UMBC

DISSERTATION APPROVAL SHEET

Title of Dissertation: Quantum Optical State Preparation for Quantum Communication

Name of Candidate: Saurabh Shringarpure ni95333@umbc.edu

Doctor of Philosophy, 2022

Graduate Program: Physics

Dissertation and Abstract Approved:

Franson, James

Franson, James

jfranson@umbc.edu

Professor

Physics Department

11/4/2022 | 10:02:32 AM EDT

NOTE: *The Approval Sheet with the original signature must accompany the thesis or dissertation. No terminal punctuation is to be used.

CURRICULUM VITAE

Name: Saurabh U. Shringarpure.

Degree and date to be conferred: Doctor of Philosophy, 2022.

Collegiate institutions attended:

1. University of Maryland Baltimore County, M.S. Physics, 2019.

2. Indian Institute of Technology Delhi, B. Tech. Engineering Physics, 2016.

Major: Physics.

Professional publications:

1. *Inhibiting phase drift in multi-atom clocks using the quantum Zeno effect*, S.U. Shringarpure and J.D. Franson, preprint, arXiv:2208.06301 (2022).

2. *Coherence of quantum states after noiseless attenuation*, S.U. Shringarpure, C.M. Nunn, T.B. Pittman, and J.D. Franson, Phys. Rev. A **105**, 013704 (2022).

3. *Proposal for a destructive controlled phase gate using linear optics*, S.U. Shringarpure and J.D. Franson, Sci. Rep. **11**, 22067 (2021).

4. *Generating entangled Schrödinger cat states using a number state and a beam splitter*, S.U. Shringarpure and J.D. Franson, Phys. Rev. A **102**, 023719 (2020).

5. *Nonlocal dispersion cancellation for three or more photons*, I.C. Nodurft, S.U. Shringarpure, B. T. Kirby, T.B. Pittman, and J.D. Franson, Phys. Rev. A **102**, 013713 (2020).

6. *Generating photon-added states without adding a photon*, S.U. Shringarpure and J.D. Franson, Phys. Rev. A **100**, 043802 (2019).

Conference presentations:

1. *Inhibiting phase drift in multi-atom clocks using the quantum Zeno effect*, S.U. Shringarpure and J.D. Franson, Frontiers in Optics + Laser Science (2022, Oct. 17 - 20, virtual), LM3F.6.

2. *Destructive controlled phase gate using linear optics*, S.U. Shringarpure and J.D. Franson, CLEO (2022, May 14 - 20, San Jose, CA), FF3J.3.

3. *Clock synchronization using the quantum Zeno effect*, S.U. Shringarpure and J.D. Franson, Poster, Frontiers in Optics + Laser Science (2021, Oct. 31 - Nov. 4, virtual), JTh5A.21.

4. *Noiseless attenuation of nonclassical states of light*, S.U. Shringarpure, C.M. Nunn, T.B. Pittman, and J.D. Franson, CLEO (2021, May 9 - 14, virtual), FTu4G.4.

5. *Generation of entangled cats from photon number states*, S.U. Shringarpure and J.D. Franson, Frontiers in Optics + Laser Science (2020, Sept. 14 - 17, virtual), LM1F.2.

6. *Generating photon-added states without adding a photon*, S.U. Shringarpure J.D. Franson, APS March Meeting (2020, March 2 - 6, virtual), W01.00005.

7. *Generating photon-added states without adding a photon*, S.U. Shringarpure J.D. Franson, Poster, Frontiers in Optics + Laser Science (2019, Sept. 15 - 19, Washington D.C.), JW4A.52.

Professional positions held:

1. Graduate Research Assistant, Univ. of Maryland Baltimore County, USA (2019-2022).

2. Graduate Teaching Assistant, Univ. of Maryland Baltimore County, USA (2017-2018).

ABSTRACT

Title of Document: QUANTUM OPTICAL STATE PREPARATION FOR QUANTUM COMMUNICATION

Saurabh U. Shringarpure
Doctor of Philosophy, 2022

Directed By: Dr. James D. Franson
Professor
Department of Physics

Nonclassical states of light are essential for long-distance quantum communication. In this dissertation, we theoretically analyze the state preparation of nonclassical states of light, resource-efficient quantum optical information processing, decoherence in quantum optical communications, and the use of the quantum Zeno effect to protect the phase of a quantum clock. An essential component of a quantum network is entanglement distribution. We study a method that can encode quantum information in entangled macroscopic superposition states, which typically carry a large number of photons. This is based on the generation of phase-entangled Schrödinger cat states using linear optical elements such as beam splitters for possible application in entanglement distribution. Controlled phase shifts can be used to verify the entanglement of the Schrödinger cat states. We then show how linear optical elements can be used to implement a controlled phase shift efficiently, with possible applications in quantum repeaters. Decoherence can arise from photon loss in quantum communication applications. Nevertheless, noiselessly attenuating single rail qubits prior to the transmission can suppress the effects of loss in the channel. A linear optical realization of noiseless attenuation is described in phase space by conditional measurements of zero photons in one of the output ports of a beam splitter. We study this approach and analyze the

coherence of quantum states that have been attenuated using this operation. Finally, we explore the use of the quantum Zeno dynamics to protect multi-atom clocks from phase drift.

QUANTUM OPTICAL STATE PREPARATION FOR QUANTUM COMMUNICATION

By

Saurabh U. Shringarpure

Thesis submitted to the Faculty of the Graduate School of the University of Maryland, Baltimore County, in partial fulfillment of the requirements for the degree of

Doctor of Philosophy

2022

To my parents

Acknowledgements

First and foremost, I would like to thank Dr. James Franson for his boundless wisdom, patience and kindness. I am truly grateful to him for giving me the chance to pursue a Ph.D. under his guidance. I thank him for listening to all of my questions and ideas. I am always amazed by his creative perspectives in tackling problems and he has inspired me to do better each time. His intuition about physical phenomena was truly motivating. I thank him for having immense patience and encouraging me to develop as a researcher at my own pace. I am extremely fortunate to have been his student.

I would like to acknowledge Dr. Todd Pittman for his inspiring enthusiasm and curiosity in Physics. I thank him for teaching me the value of good communication. His ability to give simple explanations for seemingly very complex phenomena is absolutely amazing. I am grateful I got the opportunity to observe and learn from him in our meetings. I also appreciate his support and kindness during my doctorate.

I would also like thank the rest of my Ph.D. committee: Dr. Sebastian Deffner, Dr. Jason Kestner, and Dr. Brian Kirby, for their continued support. I thank Dr. Deffner for his honest feedback. His advice to me about looking at the bigger picture has been really illuminating, and I appreciate it. Working with him during the summer rotation was a joy and immensely valuable experience. I thank Dr. Kestner for his outstanding teaching in the Electromagnetism and Quantum Information courses. It is fair to say that my cohort will never forget the problem with the fridge magnet! I am thankful to Dr. Kirby for our fruitful collaboration and his past contributions to the field we build upon in this dissertation.

I am grateful to my cohort for their friendship. I will cherish the memories of us working on Dr. Kestner's assignments and preparing for the Quals. In particular, I thank Cory Nunn and Nathan Myers for being inspiring role models with impeccable work ethics. Brainstorming with Cory and discussions with senior group members: Richard Brewster, Ian Nodurft, and Hari Lamsal, helped me develop as a researcher.

I also thank Anin Puthukkudy, Daniel Wines, Mansoor Shehzad, Noah Sienkiewicz, Rajat Patel, Shayna Greenblatt, Talia Greenblatt, and Vijin Kizhake Veetil for making my experience in graduate school memorable.

I am grateful to my parents - Uday and Ninal, grandma Pramila, and my sister Sonal, for their love and continuous encouragement and support. This dissertation could not have been possible without them. Their belief in me and their blessings has been a constant source of motivation. I thank my aunt and teacher, Swati Sule, and my cousin, Purval Sule, for nurturing curiosity about the world and Physics in me that has kept me going. My accomplishments are thanks to them, and I will always be in their debt.

Finally, I thank the reader for giving me your valuable time. I hope you find this dissertation illuminating.

Table of Contents

Chapter 1 : Introduction

Quantum communication applications require the ability to transport quantum states between distant locations. The motivating goal of this project is to improve quantum communication using photons. A hybrid of linear and nonlinear optics is used in this study to prepare quantum optical states, process information, and improve quantum state communication. There have been several proposed methods of encoding quantum information into physical systems. These include superconducting qubits, solid-state vacancy centers, and photonic qubits [1]. Photons can carry qubits over long distances without much degradation and in a relatively short time. For example, a recent experiment sent a quantum state from the Earth to a satellite [2]. Clearly, photonic qubits are better suited for communication than matter-based ones.

As a result, optical quantum communication networks will be crucial for global systems in the near future [3]. Fault-tolerant quantum computing requires a large number of qubits sharing entanglement [4], one of the reasons for setting up extensive networks. In practice, maintaining this kind of entanglement and using it for computation even at one location is challenging, and so "Quantum Data Centers" that interface between computing, communication, and sensing will be necessary [5]. A city-wide quantum network "DC-Qnet" has been recently announced for Washington D.C., laying the foundations for this future.

First and foremost, communication requires methods for generating the signal we want to send. We need ways to encode information in light's various degrees of freedom in optical quantum communications. Polarization, photon numbers, frequencies and time of a pulse, amplitude, and phase degrees of freedom can be used to encode qubits [4]. Realizing this encoding of information is what we generally refer to as state preparation.

This thesis starts by presenting an optical quantum state preparation method that produces a superposition between a coherent state and one of its orthogonal states. These are particularly attractive because they may be resilient to decoherence from photon losses. Coherent states are closest to the classical notion of an electromagnetic wave and remain intact in the event of photon annihilation. Entangled states show a noticeable departure from classical theory and intuition as their subsystems can exhibit greater correlations than allowed classically under the assumptions of locality and realism [6]. Therefore, it is essential to have methods for distributing and testing entanglement. Here we study the phase entanglement produced by splitting a pure photon number state into two separate beams.

Based on Ref. [7], photon number states are one of light's most "non-classical" quantum states. The phase of a pure number state is random or indeterminate. We show that beam splitters, one of the most common optical devices, can produce quantum states with entangled phases (Schrödinger cat states) when number states pass through them. Nonclassicality at a beam splitter is known to create entanglement [8]. As a result, splitting of number states at a beam splitter is an ideal starting point for studying entanglement distribution. The famous Bell's inequality violation [9,10] demonstrates that quantum correlations are stronger than classical ones. With the help of a single-photon interferometer, a cross-Kerr effect, and conditional measurements on the quadratures of the light field, we show that Bell's inequality is violated by these entangled Schrödinger cat states [11].

Crystals with nonlinear susceptibility can implement the cross-Kerr effect [12] needed in the Bell's inequality test mentioned above. However, it is impossible to achieve large, controlled phase shifts with current technology and materials, and we investigate instead the possibility of using linear elements with conditional measurements. We then examine how quantum information processing can be done using controlled phase gates. These controlled phase gates are also essential to circuit-based quantum computing [13]. A large body of past and ongoing research is devoted to scalable quantum information processing using optics. However, a scalable implementation is still out of reach due to the requirement for a large number of resources. In this work, we will develop a technique to implement a controlled phase gate with fewer resources that significantly improves the success probabilities [14]. This comes at the expense of destroying the control at the end of a successful gate operation.

Decoherence due to the environment can pose a challenge to optical quantum communication, despite its merits. Amplifying the signal is insufficient to address this problem for quantum states encoded in phase space variables beacause quantum mechanics prohibits it from being done deterministically without adding noise [15,16]. Mičuda et al. proposed noiselessly attenuating before transmission and noiselessly amplifying the signals at the receiver, to suppress the effects of noise in the channel [17]. We can achieve noiseless attenuation using a conditional measurement of zero photons at one of the outputs of a beam splitter. Nunn et al. demonstrated the zero-photon subtraction (ZPS) technique in their experiment [18,19]. They examined the statistical effects of noiseless attenuation via ZPS. We investigate whether ZPS preserves phase information and is genuinely noiseless.

Quantum communication protocols require reliable timekeeping in addition to methods for suppressing noise in channels. We propose a novel method for potentially forming better clocks using quantum Zeno dynamics. Atomic clocks have significantly improved timekeeping over quartz clocks as each of the unperturbed atoms of a species will have the same energy levels [20]. However, different environments, such as stray electromagnetic fields, can cause the atoms to change their level structure and cause phase drifts to occur erroneously. This thesis proposes a technique that can protect multi-atom clocks from phase drifts by restricting them to a suitable subspace using the quantum Zeno effect [21]. There are parallels between this and quantum computing in decoherence-free subspaces [22].

This work fits within the current trends in quantum computing and communication. We hope this contributes to the ongoing efforts toward the second quantum internet revolution by aiding in the quest to understand quantum optical theory's strengths and limitations. With the quantum internet, we aim to send and receive quantum states over large distances without destroying them. This would allow quantum computation to be performed nonlocally, in parts, distributed all over a network. Thus, a robust quantum communication network between all these distributed parts will be essential.

The rest of this thesis is organized as follows. Chapter 2 describes some fundamental concepts that will support the rest of the material. Chapter 3 discusses generating nonclassical quantum states using conditional measurements. Chapter 4 analyzes the generation of phase-entangled Schrödinger cat states and violating Bell's inequality. Chapter 5 proposes a destructive controlled-phase gate using linear optics and conditional measurements for single-rail qubits. Chapter 6 studies the coherence properties of quantum states undergoing noiseless attenuation with linear optics and conditional measurements. Chapter 7 investigates the use of the quantum Zeno effect to prevent phase drift in multi-atom clocks. Finally, Chapter 8 provides a summary and conclusions.

Chapter 2 : Background concepts

2.1 The postulates of quantum mechanics

Quantum mechanics is a mathematical framework that is useful in explaining physical phenomena typically at the microscopic scale. At its core, there are several postulates [23]. These are:

(1) A unit vector represents all the accessible information of the state of a closed physical system, $|\psi\rangle$, residing in a Hilbert space, $\mathcal{H}$, which is referred to as the "state vector."

(2) The observable physical attributes of any system are represented by Hermitian operators acting on vectors of this Hilbert space.

(3) The measurement outcomes of any observable are the eigenvalues of the corresponding Hermitian operator.

(4) The probability of a specific outcome is given by the square of the absolute value of the inner product between the state of the system and the corresponding eigenvector of the Hermitian operator.

(5) After the measurement, the system's state is given by the eigenvector of the Hermitian operator corresponding to the realized outcome. This is known as the "state collapse."

(6) The Schrödinger equation gives the time evolution of an unobserved state vector:

$$i\hbar \frac{\partial|\psi\rangle}{\partial t} = \hat{H}|\psi\rangle, \tag{2.1}$$

where $\hat{H}$ is the Hamiltonian, the operator for the total energy.

2.2 Density operators

If the quantum states of the system are not completely known but described only as an ensemble of "pure" quantum states then we have a "mixed state." The density operators are convenient representations of these mixtures. The density operator $\hat{\rho}$ for an ensemble of quantum states $\left\{p_k, |\psi\rangle_k\right\}$, where p_k is the probability that the state is $|\psi\rangle_k$, is given by

$$\hat{\rho} = \sum_k p_k |\psi\rangle_k {}_k\langle\psi|. \tag{2.2}$$

Several ensembles can give the same density operator.

The expectation value of a Hermitian observable, $\hat{O}$, for a state described by a density operator is given by a trace operation: $\mathrm{Tr}\left[\hat{O}\hat{\rho}\right]$. The post measurement state just after realizing one of the distinct measurement outcomes can be obtained using a set of orthogonal projection operators or "von Neumann projectors", $\left\{\hat{\Pi}_m\right\}$. These capture the transformation that occurs during the state collapse from the postulate (5) and satisfy a completeness condition: $\sum_m \hat{\Pi}_m = \hat{I}$ [1]. The completeness condition may be considered a consequence of the normalization of sum of probabilities of all outcomes, as the probability of an outcome m is given by

$$p(m) = \mathrm{Tr}\left[\hat{\Pi}_m \hat{\rho} \hat{\Pi}_m\right] = \mathrm{Tr}\left[\hat{\Pi}_m \hat{\rho}\right]. \tag{2.3}$$

Here, $\hat{\Pi}_m$ are the elements of a projection valued measure [1].

The normalized density operator, when the outcome m is realized, becomes

$$\frac{\hat{\Pi}_m \hat{\rho} \hat{\Pi}_m}{p(m)}. \tag{2.4}$$

General measurements do not require the operators transforming the state to be Hermitian, von Neumann projectors, and are given by so-called "Kraus operators" $\{\hat{M}_m\}$ satisfying the completeness condition $\sum_m \hat{M}_m^\dagger \hat{M}_m = \hat{I}$ [1]. The probability of an outcome m is given by

$$p(m) = \mathrm{Tr}\left[\hat{M}_m \hat{\rho} \hat{M}_m^\dagger\right] = \mathrm{Tr}\left[\hat{M}_m^\dagger \hat{M}_m \hat{\rho}\right]. \tag{2.5}$$

Here, $\hat{M}_m^\dagger \hat{M}_m$ are the elements of a positive operator valued measure [1], and the normallized, post measurement density operator is given by

$$\frac{\hat{M}_m \hat{\rho} \hat{M}_m^\dagger}{p(m)}. \tag{2.6}$$

These general measurements may be important when a part of the system is measured, for example when considering states of open systems that can interact with the environment. In this thesis we will use von Neumann projectors wherever possible but a detailed description about these general measurements can be found in Ref. [1].

Analogous to the Schrödinger equation for state vectors, the Liouville-von Neumann equation describes the dynamics of a density operator of a closed system:

$$\frac{d\hat{\rho}}{dt} = -\frac{i}{\hbar}\left[\hat{H}, \hat{\rho}\right]. \tag{2.7}$$

The dynamics of an open quantum system are more complicated and generally given by a quantum master equation. For environments satisfying the Born-Markov approximations of weak coupling to the system and short memory interactions, and when the system and the environment are initially in a product state, a Lindblad master equation describes the dynamics [24].

A Lindblad master equation has the form:

$$\frac{d\hat{\rho}}{dt} = -\frac{i}{\hbar}[H,\hat{\rho}] + \sum_k \gamma_k \left(\hat{L}_k \hat{\rho} \hat{L}_k^\dagger - \frac{1}{2}\left\{ \hat{L}_k^\dagger \hat{L}_k, \hat{\rho} \right\} \right) \tag{2.8}$$

where γ_k are the interaction strengths and $\hat{L}_k$ are the corresponding Kraus operators that describe transformations of the system due to the interaction with the environment. These are also commonly known as the jump operators because they can be thought of as abrupt jumps or transitions experienced by the system. The first term in parantheses captures the modifications to the density operator due to the jump operations, whereas the second term is required to normalize the trace of the final density operator to unity [24].

2.3 Properties of a quantum system

2.3.1 Superposition

States of a quantum system can be represented by vectors residing in a Hilbert space. As linear combinations of vectors are also vectors, the state of a quantum system can be a superposition of states. If we consider a cat as a quantum system then it means, very counterintuitively, there exists some state that describes the cat which is an equal "superposition" of it being alive and dead at the same time, when not observed [25].

2.3.2 Entanglement

Two, or more, subsystems may be described by a state vector that cannot be written as a simple tensor product of state vectors each describing a subsystem independently. The subsystems in these "entangled" states are highly correlated. These correlations may even exceed any classically allowed correlations as shown by a violation of Bell's inequality [9,10].

2.3.3 Interference

Upon measurement, the state collapse may leave the system in a superposition of states if the measurement does not distinguish between these states. In such cases the states may superpose and increase the probability of that outcome, constructive interference, or it may decrease the probability, destructive interference. Classically, the probabilities of two events cannot cancel one another. However, destructive interference makes that possible when the measurements cannot distinguish between two possibilities or probability amplitudes.

2.4 Quasiprobabilities

2.4.1 Characteristic functions

For classical probability distribution $\rho(x)$ over some variable x we can compute the expectation value $C(\lambda) \equiv \left\langle e^{i\lambda x} \right\rangle$ which is its "characteristic function" [26]. Consequently, the probability distribution is just the Fourier transform of the characteristic function: $\rho(x) = \frac{1}{2\pi}\int_{-\infty}^{\infty} e^{-i\lambda x} C(\lambda)\, d\lambda$. Consider the exponential factor $\exp(\lambda\alpha^* - \lambda^*\alpha)$ for a phase space formed by the real and the imaginary parts of a complex amplitude α that are conjugate variables decribing a simple harmonic oscillator with angular frequency $\omega = 1$. In the quantum theory, these variables are promoted to operators which do not commute and so, different schemes for ordering the operators lead to different expectation values.

The Wigner characteristic function is given by [26],

$$C_W(\lambda) = \mathrm{Tr}\left[\hat{\rho} e^{\lambda\hat{a}^\dagger - \lambda^*\hat{a}}\right], \tag{2.9}$$

where α and α^* in $\exp(\lambda\alpha^* - \lambda^*\alpha)$ have been replaced by the annihilation and creation operators $\hat{a}$ and $\hat{a}^\dagger$, respectively, and the resulting operator is said to be

Weyl ordered [27]. If instead the operators are ordered normally, such that all the creation operators lie to the left of the annihilation operators, then we may separate them out into two exponential terms giving the characteristic function:

$$C_N(\lambda) = \mathrm{Tr}\left[\hat{\rho}e^{\lambda\hat{a}^\dagger}e^{-\lambda^*\hat{a}}\right], \tag{2.10}$$

and similarly, the antinormal ordering of operators gives:

$$C_A(\lambda) = \mathrm{Tr}\left[\hat{\rho}e^{-\lambda^*\hat{a}}e^{\lambda\hat{a}^\dagger}\right]. \tag{2.11}$$

2.4.2 Wigner distribution

The Wigner distribution is the Fourier transform of the Weyl ordered characteristic function [26]:

$$W(\alpha) = \frac{1}{\pi^2}\int \exp\left(\lambda^*\alpha - \lambda\alpha^*\right)C_W(\lambda)d^2\lambda. \tag{2.12}$$

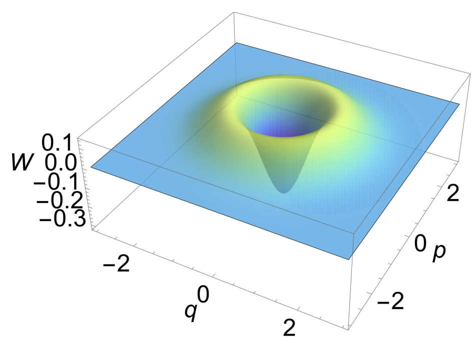

Figure 2.1 Wigner distribution of a single-photon state in the phase space formed by the conjugate variables q and p which are related to the complex amplitude α by the convention $\alpha = (q+ip)/\sqrt{2\hbar}$. Units where $\hbar = 1$ were used.

By making the substitutions: $\alpha = (q+ip)/\sqrt{2\hbar}$, $\lambda = (x+iy)/\sqrt{2\hbar}$, and $d^2\lambda = dxdy/2\hbar$, it can be shown that [27]

$$W(q,p) = \frac{1}{2\pi\hbar}\int_{-\infty}^{\infty} e^{ipx/\hbar}\left\langle q + x/2\right|\hat{\rho}\left|q - x/2\right\rangle dx \tag{2.13}$$

Wigner distributions are primarily used to easily identify the nonclassical nature of a state. For example, the volume of the negative region of the Wigner distribution of a pure, single mode state corresponds to the nonclassicality. A coherent state has no Wigner negativity, whereas a single photon state has characteristic negativity at the origin as shown in Fig. 2.1. Similarly cat states, which are quantum superpositions of coherent states with equal amplitudes and opposite phases, have fringes near the origin that can take negative values [26]. Interestingly, the negativity of a bipartite state can act as an entanglement witness [28,29]. In this way, the Wigner distribution is a powerful tool for monitoring the evolution of the nonclassicality in a noisy environment, for example.

2.4.3 Glauber-Sudarshan P distribution

The Glauber-Sudarshan P distribution is obtained from the normally-ordered characteristic function [26]:

$$P(\alpha) = \frac{1}{\pi^2}\int \exp\left(\lambda^*\alpha - \lambda\alpha^*\right)C_N(\lambda)d^2\lambda. \tag{2.14}$$

For coherent states these are simply delta functions located at the phase space value equal to their amplitude. This makes P distributions particularly useful if we want to express states in terms of collections of coherent states. For a general classical state which is a statistical mixture of coherent states, the P distribution is simply the well-behaved probability distribution of complex amplitudes that describe it. The only classical pure states are coherent states [30]. One of the biggest problems of these quasiprobabilities is that they can be highly singular which makes analyses quite difficult for a general state. Unlike the Wigner distriution of Fig. 2.1 the P distribution of a single-photon state is highly singular, more singular than a delta function distribution, hence cannot be plotted [26].

2.4.4 Husimi-Kano Q distribution

The Husimi-Kano Q distribution is obtained from the antinormal characteristic function [26]:

$$Q(\alpha) = \frac{1}{\pi^2}\int \exp(\lambda^*\alpha - \lambda\alpha^*) C_A(\lambda) d^2\lambda \tag{2.15}$$

In terms of the density operator, the Q distribution is easiest to compute using [26]

$$Q(\alpha) = \langle\alpha|\hat{\rho}|\alpha\rangle/\pi, \tag{2.16}$$

which is nonnegative and bounded $(0 \le Q \le 1/\pi)$, unlike the previous examples.

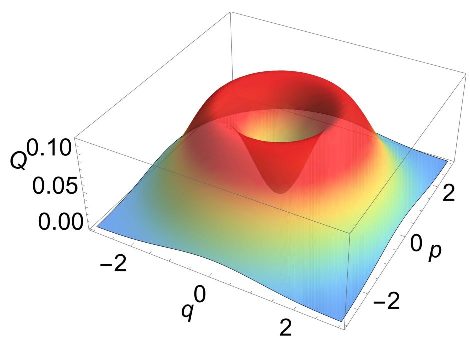

Figure 2.2 Husimi-Kano Q distribution of a single-photon state in the phase space formed by the conjugate variables q and p which are related to the complex amplitude α by the convention $\alpha = (q + ip)/\sqrt{2\hbar}$. Units where $\hbar = 1$ were used.

Despite these properties, it is not a probability distribution because $Q(\alpha)$ does not represent the probability of mutually exclusive states α, as required by the third axiom of the probability theory [31]. The Q distribution can be measured directly, making it helpful in characterizing optical quantum states. A 50:50 beam splitter divides the signal into two coherent parts, and balanced homodyne detection is used to separately measure the two quadratures of the field. The joint probability for those simultaneous measurements is simply the Q distribution of the initial field before the beam splitter [32-34]. Figure 2.2 illustrates the Q distribution of a single-photon state.

All the distributions mentioned above are quasiprobabilities. They all show some properties that cannot be satisfied by a valid probability distribution.

2.5 Heralding, post-selection, and the quantum Zeno effect

Measurements in quantum mechanics play an essential role. Classically, the system remains unaffected by measurements, but quantum theory tells us that they modify systems as per postulate (5) mentioned earlier. This modification can be quite dramatic and may occur even if we only observe a small part of the system. The changes depend on the entanglement between the subsystems. Suppose a system can be partitioned into two separate parts A and B, so that the initial product state is given by $\hat{\rho} = \hat{\rho}_A \otimes \hat{\rho}_B$. After some unitary time evolution $\hat{U}$, the system may no longer be in a product state. However, we can measure the subsystems A and B separately in what we refer to as partial measurements. Let's consider measuring part B. The final form of the system would then be given by

$$\left(\hat{I} \otimes \sum_k \hat{\Pi}_k\right) \hat{U} \hat{\rho} \hat{U}^\dagger \left(\hat{I} \otimes \sum_k \hat{\Pi}_k\right). \tag{2.17}$$

Here, the identity acts on part A whereas $\hat{\Pi}_k$ project part B onto different measurement outcomes k. From this, we can immediately see that these different outcomes for B can give very different final normalized states for part A,

$$\hat{\rho}_{A|k} = \frac{\left(\hat{I} \otimes \hat{\Pi}_k\right) \hat{U} \hat{\rho} \hat{U}^\dagger \left(\hat{I} \otimes \hat{\Pi}_k\right)}{\mathrm{Tr}\left[\hat{U}^\dagger \left(\hat{I} \otimes \hat{\Pi}_k\right) \hat{U} \hat{\rho}\right]}, \tag{2.18}$$

where $\hat{\rho}_{A|k}$ represents the density operator of A just after the outcome k is realized.

Thus, we can implement transformations for the system of interest, part A, by observing an ancillary system, part B, that may otherwise be difficult or impossible to realize experimentally with an ordinary, unitary time evolution. This process is referred to as a "conditional measurement" that can be performed by post selecting or heralding.

Frequent measurements of a quantum system can lead to interesting behavior. Consider a system that starts in an eigenstate of a measurement observable $\hat{O}$. Time evolution of the system can take it into a superposition of different eigenstates. However, suppose the same observable $\hat{O}$ is measured repeatedly in sufficiently quick succession. The system does not have enough time to build the probability amplitudes of the measurably different eigenstates orthogonal to the initial one. Each of the measurements projects the system onto the initial eigenstate with a high probability. Thus, effectively the dynamics is "frozen" or slowed down in a phenomenon known as the quantum Zeno effect [21,35]. The anti-Zeno effect is a complementary effect where a different, lower rate of measurements leads to a speed up in the dynamics [36].

If a measurement cannot distinguish between several orthogonal states, it projects the system down onto a subspace spanned by those orthogonal states. In this case, the system is free to evolve within that subspace but forced to remain inside it [37]. As we will see in Chapter 7, applications like inhibiting a clock's phase drift can employ such quantum Zeno dynamics.

2.6 Quantum optics

2.6.1 Quantization of the electromagnetic field

Maxwell's equations describe the classical theory of light [38]. For fields in the vacuum, in the absence of charges and currents, these are

$$\nabla \times \boldsymbol{E} = -\frac{\partial \boldsymbol{B}}{\partial t} \tag{2.19}$$

$$\nabla \times \boldsymbol{B} = \mu_0 \varepsilon_0 \frac{\partial \boldsymbol{E}}{\partial t} \tag{2.20}$$

$$\nabla . \boldsymbol{B} = 0 \tag{2.21}$$

$$\nabla . \boldsymbol{E} = 0 \tag{2.22}$$

where $\boldsymbol{E}$ and $\boldsymbol{B}$ are the electric and magnetic fields, respectively. μ_0 and ε_0 are the permeability and permittivity of free space. In terms of the vector potential $\boldsymbol{A}$ in the absence of any sources, we have

$$\boldsymbol{B} = \nabla \times \boldsymbol{A} \tag{2.23}$$

$$\boldsymbol{E} = -\nabla \phi - \frac{\partial \boldsymbol{A}}{\partial t}. \tag{2.24}$$

Combined with Maxwell's equations in the Coulomb gauge with $\nabla . \boldsymbol{A} = 0$ and $\phi = 0$, this gives a simple wave equation

$$c^2 \nabla^2 \boldsymbol{A} = \frac{\partial^2 \boldsymbol{A}}{\partial t^2}, \tag{2.25}$$

where $c \equiv 1 \big/ \sqrt{\mu_0 \varepsilon_0}$ is the speed of light in the vacuum. The general solution to this equation for monochromatic light is a weighted sum of transverse plane waves. Let's consider a Fourier expansion of the vector potential inside a finite volume, V:

$$\boldsymbol{A} = \sum_{\boldsymbol{k},\mu} \left(\boldsymbol{e}_{\boldsymbol{k},\mu} \alpha_{\boldsymbol{k},\mu} e^{i(\boldsymbol{k}.\boldsymbol{r} - \omega t)} + c.c. \right) \tag{2.26}$$

where $\alpha_{\boldsymbol{k},\mu}$ is the amplitude in a given mode (Fourier component), $\boldsymbol{e}_{\boldsymbol{k},\mu}$ is the polarization unit vector for polarization μ which is perpendicular to the wave vector $\boldsymbol{k}$ for transverse waves, the angular frequency is given by $\omega \equiv c|\boldsymbol{k}| = ck$, and finally $c.c.$ is the complex conjugate of the term on the left.

The electric and magnetic fields are, therefore

$$\boldsymbol{E} = \sum_{\boldsymbol{k},\mu}\left(\boldsymbol{e}_{\boldsymbol{k},\mu} i\omega\alpha_{\boldsymbol{k},\mu} e^{i(\boldsymbol{k}.\boldsymbol{r}-\omega t)} + c.c.\right) \tag{2.27}$$

$$\boldsymbol{B} = \sum_{\boldsymbol{k},\mu}\left(\left(i\boldsymbol{k}\times\boldsymbol{e}_{\boldsymbol{k},\mu}\right)\alpha_{\boldsymbol{k},\mu} e^{i(\boldsymbol{k}.\boldsymbol{r}-\omega t)} + c.c.\right) \tag{2.28}$$

The energy density contained in the electric and magnetic fields in free space is

$$\mathcal{U} = \frac{1}{2}\varepsilon_0 E^2 + \frac{1}{2\mu_0}B^2 \tag{2.29}$$

The Hamiltonian of the system given by the total energy reduces to then

$$H = \sum_{\boldsymbol{k},\mu}\omega^2 V\varepsilon_0\left[\alpha_{\boldsymbol{k},\mu}\alpha^*_{\boldsymbol{k},\mu} + \alpha^*_{\boldsymbol{k},\mu}\alpha_{\boldsymbol{k},\mu}\right], \tag{2.30}$$

which has the same form as the Hamiltonian for a large number of uncoupled simple harmonic oscillators. For simplicity, let's only consider a single mode and drop all the subscripts, so we have

$$H \equiv \frac{1}{2}\left(p^2 + \omega^2 q^2\right), \tag{2.31}$$

where the conjugate canonical variables are defined as

$$x \equiv \sqrt{V\varepsilon_0}\,(\alpha^* + \alpha) \tag{2.32}$$

$$p \equiv \sqrt{\omega^2 V\varepsilon_0}\, i(\alpha^* - \alpha). \tag{2.33}$$

Quantizing the field corresponds to promoting the variables to operators that act on quantum states, so that $x \rightarrow \hat{x}$ and $p \rightarrow \hat{p}$. By imposing the commutator, $[\hat{x}, \hat{p}] = i\hbar$, we can rewrite α as an operator $\sqrt{\hbar/2\omega V\varepsilon_0}\hat{a}$ and similarly α^* as its Hermitian conjugate so that $\left[\hat{a},\hat{a}^\dagger\right]=1$ [26]. The Hamiltonian in terms of the new operators is

$$H=\hbar\omega\left(\hat{a}^\dagger\hat{a}+\frac{1}{2}\right). \tag{2.34}$$

The operators $\hat{a}$ and $\hat{a}^\dagger$ have the effect of annihilating and creating an excitation of the harmonic oscillator in a given mode, respectively:

$$\hat{a}\left|n\right\rangle=\sqrt{n}\left|n-1\right\rangle \tag{2.35}$$

$$\hat{a}^\dagger\left|n\right\rangle=\sqrt{n+1}\left|n+1\right\rangle. \tag{2.36}$$

Here, $\left|n\right\rangle$ denotes the n^{th} excitation of the harmonic oscillator and $\left|0\right\rangle$ the vacuum state with the lowest possible energy. The excitations of the electromagnetic field are referred to as "photons." Finally, we can redefine the vector potential and, consequently, the electric and the magnetic fields as operators acting on the quantum state of the electromagnetic field.

2.6.2 Optical devices and their unitaries

We have shown how to describe the electromagnetic field in the quantum theory. In quantum optics experiments, we use optical devices such as beam splitters, mirrors, glass slabs, etc. to modify and manipulate the electromagnetic fields to our needs. The evolution of the quantum state of light in these optical devices is described by unitary Schrödinger evolution assuming no losses. In practice, we can greatly simplify the analysis by considering input-to-output relations for these devices, provided that the Hamiltonian is at most a quadratic polynomial in the field operators of the consituent modes.

The Schrödinger evolution, $\hat{U} = e^{-i\hat{H}t/\hbar}$, is then referred to as a “Gaussian unitary.” These have the property of transforming quantum states with Gaussian Wigner distributions, such as the vacuum state, coherent states, and thermal states, into other states with Gaussian distributions [39].

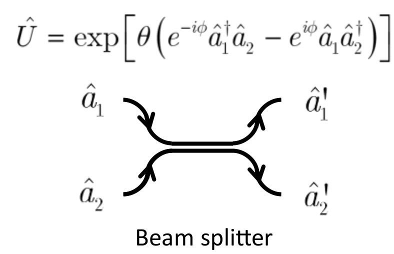

Figure 2.3 A fiber coupler type beam splitter. The input modes correspond to field operators $\hat{a}_1$ and $\hat{a}_2$, while the output modes correspond to $\hat{a}_1'$ and $\hat{a}_2'$.

First, consider the example of a lossless fiber coupler type beam splitter as shown in Fig. 2.1. It mixes the fields in two electromagnetic modes with some coupling strength κ for some time t . The unitary operator that evolves the quantum state can be modeled by a Gaussian unitary of the form

$$\hat{U} = \exp\left[\theta\left(e^{-i\phi}\hat{a}_1^\dagger\hat{a}_2 - e^{i\phi}\hat{a}_1\hat{a}_2^\dagger\right)\right], \tag{2.37}$$

with $\theta \equiv \kappa t/\hbar$. Let’s consider that the beam splitter splits a single photon state incoming in the first mode so that the initial state can be written as $|1,0\rangle$. The final state in the two outputs is then

$$\hat{U}|1,0\rangle = \cos\theta|1,0\rangle - e^{i\phi}\sin\theta|0,1\rangle. \tag{2.38}$$

Alternatively, by expanding the identity operator as a product of the unitary and its Hermitian conjugate, and using the fact that the unitary leaves the vacuum state unchanged, $\hat{U}|0,0\rangle = |0,0\rangle$, we have

$$\hat{U}|1,0\rangle = \left(\hat{U}\hat{a}_1^\dagger \hat{U}^\dagger\right)\hat{U}|0,0\rangle = \left(\hat{U}\hat{a}_1^\dagger \hat{U}^\dagger\right)|0,0\rangle. \tag{2.39}$$

This is equivalent to replacing the creation operator in the first mode with its Heisenberg picture evolved operator with time reversed: $\hat{a}_1^\dagger \to \hat{U}\hat{a}_1^\dagger \hat{U}^\dagger$. However, note that the state itself is still in the Schrödinger picture. It can be seen that the creation operators in the output can be related to the to the input operators by a linear transformation [13]

$$B = \begin{pmatrix} \cos\theta & -e^{i\phi}\sin\theta \\ e^{-i\phi}\sin\theta & \cos\theta \end{pmatrix}, \tag{2.40}$$

where $\cos^2\theta$ is the transmittance and $e^{i\phi}$ is the phase gained during the coupling from the first into the second mode.

More generally for any Gaussian unitary, the output creation and annihilation operators can be related to the input by a linear transformation that is referred to as a Bogoliubov transformation [40]. These linear transformations are additionally required to preserve the commutator between the operators from input to output in all the modes: $\left[\hat{a}_m, \hat{a}_n^\dagger\right] = \delta_{mn}$.

A beam splitter transformation does not mix the creation and annihilation operators and the more general linear transformation that relates the input operators to the output operators is given by

$$\begin{pmatrix} \hat{a}_1 \\ \hat{a}_2 \\ \hat{a}_1^\dagger \\ \hat{a}_2^\dagger \end{pmatrix}_{in} = \begin{pmatrix} \cos\theta & -e^{i\phi}\sin\theta & 0 & 0 \\ e^{-i\phi}\sin\theta & \cos\theta & 0 & 0 \\ 0 & 0 & \cos\theta & -e^{-i\phi}\sin\theta \\ 0 & 0 & e^{i\phi}\sin\theta & \cos\theta \end{pmatrix} \begin{pmatrix} \hat{a}_1 \\ \hat{a}_2 \\ \hat{a}_1^\dagger \\ \hat{a}_2^\dagger \end{pmatrix}_{out}. \tag{2.41}$$

Next, consider a single-mode squeezer implemented by a nonlinear crystal [41]. This produces a collinear, degenerate, down conversion process as shown in Fig. 2.2.

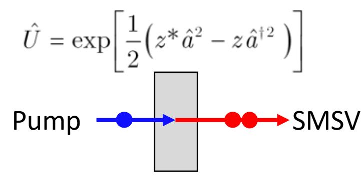

Figure 2.4 A single mode squeezed vacuum created during a collinear down conversion process.

The system undergoes unitary evolution

$$\hat{U} = \exp\left[\frac{1}{2}\left(z^* \hat{a}^2 - z\hat{a}^{\dagger 2}\right)\right], \tag{2.42}$$

where $z \equiv re^{i\theta}$ is the squeezing parameter. The Bogoliubov transform can be shown to be [40]

$$\begin{pmatrix} \hat{a} \\ \hat{a}^\dagger \end{pmatrix}_{in} = \begin{pmatrix} \cosh r & e^{i\theta}\sinh r \\ e^{-i\theta}\sinh r & \cosh r \end{pmatrix} \begin{pmatrix} \hat{a} \\ \hat{a}^\dagger \end{pmatrix}_{out}. \tag{2.43}$$

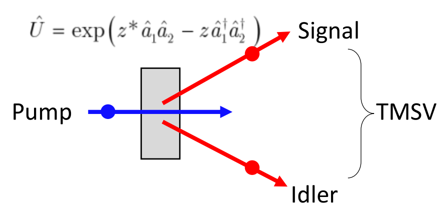

Figure 2.5 A two-mode squeezed vacuum created during a non-collinear down conversion process.

Similarly, a two-mode squeezing operator can be achieved using a non-collinear down conversion process as shown in Fig. 2.3 by with a unitary evolution [16]

$$\hat{U} = \exp\left(z^* \hat{a}_1\hat{a}_2 - z\hat{a}_1^\dagger\hat{a}_2^\dagger\right). \tag{2.44}$$

This gives [40]

$$\begin{pmatrix} \hat{a}_1 \\ \hat{a}_2 \\ \hat{a}_1^\dagger \\ \hat{a}_2^\dagger \end{pmatrix}_{in} = \begin{pmatrix} \cosh r & 0 & e^{i\theta}\sinh r & 0 \\ 0 & \cosh r & 0 & e^{i\theta}\sinh r \\ e^{-i\theta}\sinh r & 0 & \cosh r & 0 \\ 0 & e^{-i\theta}\sinh r & 0 & \cosh r \end{pmatrix} \begin{pmatrix} \hat{a}_1 \\ \hat{a}_2 \\ \hat{a}_1^\dagger \\ \hat{a}_2^\dagger \end{pmatrix}_{out} . \tag{2.45}$$

As we are considering various Gaussian unitaries in this section, it is worth considering the single mode displacement operator which creates a coherent state from the vacuum state. It is given by the unitary

$$\hat{U} = \exp\left(\alpha\hat{a}^\dagger - \alpha^*\hat{a}\right) \tag{2.46}$$

where α is the complex displacement amplitude. Experimentally, this operator can be implemented using a highly asymmetrical beam splitter and a large-amplitude coherent state in the secondary input mode [42].

The input-output transform for a displacement operation is quite simple as it only adds a constant offset [40]

$$\begin{pmatrix} \hat{a} \\ \hat{a}^\dagger \end{pmatrix}_{in} = \begin{pmatrix} \hat{a} \\ \hat{a}^\dagger \end{pmatrix}_{out} - \begin{pmatrix} \alpha \\ \alpha^* \end{pmatrix}. \tag{2.47}$$

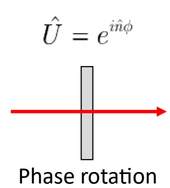

Figure 2.6 A phase rotation implemented by inserting a glass slab in the optical path.

To conclude the discussion of Gaussian unitaries, let's consider the phase rotation unitary [40]

$$\hat{U} = e^{i\hat{n}\phi}. \tag{2.48}$$

The Bogoliubov transformation for this is given by [40]

$$\begin{pmatrix} \hat{a} \\ \hat{a}^{\dagger} \end{pmatrix}_{in} = \begin{pmatrix} e^{-i\phi} & 0 \\ 0 & e^{i\phi} \end{pmatrix} \begin{pmatrix} \hat{a} \\ \hat{a}^{\dagger} \end{pmatrix}_{out} . \tag{2.49}$$

Any arbitrary Gaussian unitary may be expanded as a product of displacements, rotations, and squeezing operations, making them fundamental [40]. The corresponding multiport generalizations are used [43-45] for multiport unitaries.

2.6.3 Disentanglement formulas

We often need to analyze the unitary evolution when the initial quantum state is a complicated superposition state. Here we cannot use Bogoliubov transformations between the input and the output creation operators in an effective way. Several phenomena of this kind in quantum optics can be analyzed using Lie algebras and Lie groups [46]. Lie group elements may be expressed in terms of an exponential of linear combinations of its generators, such as $\hat{U} = \exp\left(i\sum_{k=1}^{n} c_k \hat{A}_k\right)$. Note, however, that the exponential cannot be broken up simply into a product of the exponentials of the generators as they may not always commute.

When the commutator of two operators, say a and b, also commutes with each of the operators, the Baker-Cambell-Housdorff formula states that

$$\exp(a+b) = \exp(a)\exp(b)\exp\left(-\frac{1}{2}[a,b]\right). \tag{2.50}$$

Generally, the set of all the commutators between the generators defines a Lie algebra. Thus, an arbitrary Lie group element may be expressed as a product of exponentials of these generators and their commutators. Unitary time evolutions are nothing but Lie group elements, and the generators differ depending on the system of interest. This framework can be helpful if the Lie algebras are finite-dimensional.

Take the example of the displacement operator $\hat{U} = \exp\left(\alpha \hat{a}^\dagger - \alpha^* \hat{a}\right)$. The operators $\hat{a}^\dagger$ and $\hat{a}$ are the generators here, and they have a simple commutator, $\left[\hat{a}, \hat{a}^\dagger\right] = \hat{I}$, with all other relevant commutators being trivial. This forms a Heisenberg-Weyl algebra and the displacement operator can be written in the form [47]

$$\hat{U} = \exp\left(\beta \hat{a}^\dagger\right) \exp\left(\gamma \hat{a}\right) \exp\left(\delta \hat{I}\right), \tag{2.51}$$

with coefficients γ, β, and δ that depend on the order of the exponential operators. Here, we have $\beta = \alpha$, $\gamma = -\alpha^*$, and $\delta = -|\alpha|^2 / 2$ [47].

Now let's consider the single-mode squeeze operator in the form $\hat{U} = \exp\left[\tau \hat{K}_+ - \tau^* \hat{K}_-\right]$, with the ladder operators defined as $\hat{K}_+ \equiv \hat{a}^{\dagger 2} / 2$, $\hat{K}_- \equiv \hat{a}^2 / 2$ [48,49]. The relevant Lie algebra here is $\mathfrak{su}(1,1)$ with the commutators $\left[\hat{K}_+, \hat{K}_-\right] = -2\hat{K}_0$ and $\left[\hat{K}_0, \hat{K}_\pm\right] = \pm \hat{K}_\pm$ where $\hat{K}_0 \equiv \frac{1}{2}\left(\hat{a}^\dagger \hat{a} + \frac{1}{2}\hat{I}\right)$.

With this alebgra, it is possible to rewrite the squeeze operator as [47]

$$\hat{U} = \exp\left(\frac{\tau}{|\tau|} \tanh|\tau| \hat{K}_+\right) \exp\left(-2 \ln \cosh|\tau| \hat{K}_0\right) \exp\left(\frac{-\tau^*}{|\tau|} \tanh|\tau| \hat{K}_-\right). \tag{2.52}$$

The two-mode squeeze operator has the same form but with the definitions $\hat{K}_+ \equiv \hat{a}_1^\dagger \hat{a}_2^\dagger$, $\hat{K}_- = \hat{a}_1 \hat{a}_2$, and $\hat{K}_0 \equiv \frac{1}{2}\left(\hat{a}_1^\dagger \hat{a}_1 + \hat{a}_2^\dagger \hat{a}_2 + \hat{I}\right)$ where $\hat{a}_1$ and $\hat{a}_2$ are the annihilation operators of the two modes [47,49].

As a final example, let's consider a beam splitter with the unitary evolution of the form $\hat{U} = \exp\left(\tau \hat{J}_+ - \tau^* \hat{J}_-\right)$, with the ladder operators $\hat{J}_+ \equiv \hat{a}_1^\dagger \hat{a}_2$, and $\hat{J}_- \equiv \hat{a}_1 \hat{a}_2^\dagger$.

They form an $\mathfrak{su}(2)$ Lie algebra with the commutators, $\left[\hat{J}_+, \hat{J}_-\right] = +2\hat{J}_0$ and $\left[\hat{J}_0, \hat{J}_\pm\right] = \pm\hat{J}_\pm$ where $\hat{J}_0 \equiv \frac{1}{2}\left(\hat{a}_1^\dagger\hat{a}_1 - \hat{a}_2^\dagger\hat{a}_2\right)$.

It can be shown that the beam splitter unitary has the form [47]

$$\hat{U} = \exp\left(\frac{\tau}{|\tau|}\tan|\tau|\hat{J}_+\right)\exp\left(-2\ln\cos|\tau|\hat{J}_0\right)\exp\left(\frac{-\tau^*}{|\tau|}\tan|\tau|\hat{J}_-\right). \quad (2.53)$$

By changing the order of the exponentials of the generators several equivalent disentanglement formulas can be obtained, which may be useful in different applications. However, the scalar coefficients in the exponents may take up different values if the generators do not commute [47,49].

Chapter 3 : Generating nonclassical states using post selection

This chapter has been taken from Ref. [50] published in Physical Review A.

In this chapter, we use post selection on the output of an optical parametric amplifier (OPA) to generate a wide range of nonclassical states. OPAs are $\chi^{(2)}$ nonlinear crystals that convert high-energy photons into two pairs of lower-energy photons. This process is known as spontaneous parametric down conversion. The two daughter photons generated in this way are referred to as the signal and the idler. The signal and idler photons are emitted in specific spatiotemporal modes depending on the phase matching conditions. If these spatiotemporal modes are excited with a field at the input ports of the crystal, then the $\chi^{(2)}$ crystal amplifies these modes by increasing their average photon number. In this way, the device functions an optical parametric amplifier. We demonstrate that such a device can be used to create a large variety of quantum states that are a macroscopic superposition of two orthogonal states of light. Our approach here is an example of photon catalysis, where we mix a particular auxiliary state with the input on an optical device, such as a beam splitter or an OPA, and the output is conditioned on the auxiliary being unaffected [51,52].

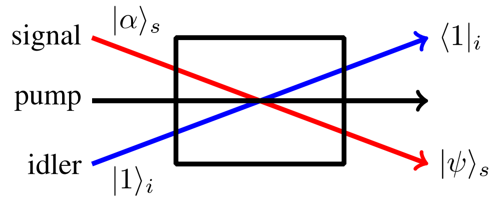

Figure 3.1 Optical parametric amplifier with a coherent state in the input signal mode and a single photon number state in the idler mode. A measurement of a single photon in the output idler mode heralds the state of interest in the output signal mode.

The basic approach is illustrated in Fig. 3.1, where a coherent state is incident in the signal mode of an optical parametric amplifier with a single photon incident in the idler mode. We post-select, or herald, the output state of the signal mode when a single photon is detected in the output idler mode. Since the signal and idler photons are emitted in pairs, the post-selection process ensures that no photons were emitted or absorbed in either mode. Nevertheless, the post-selection process can have the effect of creating a photon-added state for an appropriate choice of the gain. Other choices of the gain can produce a displaced number state or states that are orthogonal to a coherent state or a photon-added state, which may be useful for continuous-variable qubits.

Quantum state engineering methods to prepare various types of quantum states [53], such as photon-added/subtracted coherent states, thermal states, displaced number states [54], superpositions of number states [55], and truncated coherent states [56] have been explored using conditional measurements on beam splitters. These techniques have been very successful, but they have limited tunability of the prepared state due to the fixed transmittance of conventional beam splitters.

The equivalence between a lossless beam splitter and an optical parametric amplifier when the input and output signals are appropriately interchanged has been previously discussed [57,58]. This equivalence allows an optical parametric amplifier to be used with conditional measurements in a way that is somewhat analogous to the use of a beam splitter. This has been applied, for example, to the noiseless attenuation of coherent states [59] and the preparation of various non-classical states [60-62], and it provides part of the motivation for the work reported here.

This paper is organized as follows. Section 3.1 derives the form of the post-selected output state and the corresponding probability of success. Sections 3.2 and 3.3 examine the behavior of the final state as a function of the amplifier gain, including the special cases where the output is a displaced number state or a photon-added state. Section 3.4 describes the properties of the output in phase space using the Q-function for specific values of the gain. Section 3.5 provides a summary and conclusions.

3.1 State preparation

The time evolution operator $\hat{S}$ for an optical parametric amplifier can be written in a factored form given by [15,63]

$$\hat{S} = \frac{1}{g} e^{-\sqrt{1-1/g^2}\hat{a}^\dagger\hat{b}^\dagger} g^{-\left(\hat{a}^\dagger\hat{a}+\hat{b}^\dagger\hat{b}\right)} e^{\sqrt{1-1/g^2}\hat{a}\hat{b}}. \tag{3.1}$$

Here $g = \cosh(\kappa t)$ is the gain, where κ is the coupling strength of the amplifier and t is the interaction time, while $\hat{a}$ and $\hat{b}$ are the annihilation operators of the signal and the idler modes respectively. Note that we can effectively tune the amplifier gain by varying the intensity of the pump. We will define $G \equiv \sqrt{1-1/g^2}$ for convenience.

We assume that a coherent state $|\alpha\rangle_s$ is introduced in the signal mode while a single photon number state $|1\rangle_i$ is incident in the idler mode of the amplifier. This corresponds to an input state of $|\alpha\rangle_s|1\rangle_i$, which is a simplified notation for $|\alpha\rangle_s \otimes |1\rangle_i$ in the tensor product space of the signal and idler modes. The transformation produced by the optical parametric amplifier is followed by a conditional measurement of a single photon in the idler mode, which can be represented by a projection operator $\hat{\Pi}$ given by

$$\hat{\Pi} = |1\rangle_i \langle 1|_i . \tag{3.2}$$

Thus, the final state $|\psi\rangle$ after these operations is given by

$$|\psi\rangle = \hat{\Pi}\hat{S}|\alpha\rangle_s |1\rangle_i . \tag{3.3}$$

Using a Taylor series expansion of the final exponential in Eq. (3.1) gives

$$e^{G\hat{a}\hat{b}}|\alpha\rangle_s|1\rangle_i = \left(1 + G\hat{a}\hat{b} + \ldots\right)|\alpha\rangle_s|1\rangle_i = |\alpha\rangle_s\left(G\alpha|0\rangle_i + |1\rangle_i\right). \tag{3.4}$$

We see that only the first two terms of the expansion contribute after it acts on the input state. Similarly, the adjoint of the Taylor series expansion of the first exponential factor in Eq. (3.1) acting on the projection operator to the left also gives only two non-vanishing terms:

$$\hat{\Pi}e^{-G\hat{a}^\dagger\hat{b}^\dagger} = |1\rangle_i\langle 1|_i\left(1 - G\hat{a}^\dagger\hat{b}^\dagger + \ldots\right) = |1\rangle_i\langle 1|_i - G\hat{a}^\dagger|1\rangle_i\langle 0|_i . \tag{3.5}$$

Next, we let the middle exponential factor in Eq. (3.1) act on the state obtained in Eq. (3.4). Expanding the coherent state in the number basis gives

$$\begin{aligned}
&g^{-\left(\hat{a}^\dagger\hat{a}+\hat{b}^\dagger\hat{b}\right)}|\alpha\rangle_s\left(G\alpha|0\rangle_i + |1\rangle_i\right)\\
&= \left(g^{-\hat{n}_s}|\alpha\rangle_s\right)g^{-\hat{n}_i}\left(G\alpha|0\rangle_i + |1\rangle_i\right)\\
&= \left(e^{-|\alpha|^2/2}g^{-\hat{n}_s}\sum_{n=0}^{\infty}\frac{\alpha^n}{\sqrt{n!}}|n\rangle_s\right)\left(G\alpha|0\rangle_i + \frac{1}{g}|1\rangle_i\right)\\
&= \left(e^{-|\alpha|^2/2}\sum_{n=0}^{\infty}\frac{1}{\sqrt{n!}}\left(\frac{\alpha}{g}\right)^n|n\rangle_s\right)\left(G\alpha|0\rangle_i + \frac{1}{g}|1\rangle_i\right)\\
&= e^{-|G\alpha|^2/2}|\alpha/g\rangle_s\left(G\alpha|0\rangle_i + \frac{1}{g}|1\rangle_i\right).
\end{aligned} \tag{3.6}$$

Inserting Eqs. (3.1), (3.4), (3.5) and (3.6) in Eq. (3.3), we get the following post-selected (unnormalized) state in the signal mode

$$\left|\psi\right\rangle = e^{-|G\alpha|^2/2}\left(\frac{1}{g^2} - \frac{1}{g}G^2\alpha a^\dagger\right)\left|\alpha/g\right\rangle_s . \tag{3.7}$$

Equation (3.7) shows that the post-selected output state is a superposition of an attenuated coherent state and a photon-added coherent state, where the probability amplitudes of those two states can be controlled by varying the gain. It can be rewritten in another useful form by using the fact that $\alpha\left|\alpha/g\right\rangle_s = g\hat{a}\left|\alpha/g\right\rangle_s$ which gives

$$\left|\psi\right\rangle = e^{-|G\alpha|^2/2}\left(\frac{1}{g^2} - G^2\hat{a}^\dagger\hat{a}\right)\left|\alpha/g\right\rangle_s . \tag{3.8}$$

Since $\hat{a}^\dagger\hat{a} = \hat{n}_s$, this gives the following expression for the final state:

$$\left|\psi\right\rangle = e^{-|G\alpha|^2/2}\left(\frac{1}{g^2} - G^2\hat{n}_s\right)\left|\alpha/g\right\rangle_s . \tag{3.9}$$

This form of the post-selected output state provides useful insight into the effects of the post-selection process as viewed in a number-state basis, as will be discussed in the next section.

The probability P_S of success for the post-selection process is given by the norm of the final state $\left|\psi\right\rangle$ in Eq. (3.7) which can be shown to be

$$P_S = e^{-|G\alpha|^2}\left[\left(\frac{1}{g^2} - \left|\frac{\alpha}{g}\right|^2 G^2\right)^2 + \left|\frac{\alpha}{g}\right|^2 G^4\right]. \tag{3.10}$$

The final state can then be normalized to give

$$\left|\psi\right\rangle = \left(\frac{1}{g^2} - G^2\hat{n}\right)\left|\alpha/g\right\rangle \Bigg/ \sqrt{\left(\frac{1}{g^2} - \left|\frac{\alpha}{g}\right|^2 G^2\right)^2 + \left|\frac{\alpha}{g}\right|^2 G^4} . \tag{3.11}$$

The probability of success is exponentially small for large values of $|G\alpha|$.

3.2 Displaced number states

Eqs. (3.7) and (3.9) show that the post-selection process can be used to generate a continuous range of quantum states as we vary the gain. In this section, we will describe some of the properties of these states as a function of the gain. We will show that a specific value of the gain can be used to generate a displaced single-photon state.

Equation (3.9) suggests that the value of the gain can be chosen in such a way that the coefficient c_n in an expansion of the state in a basis of number states will vanish for a specific value of n. For example, an appropriate choice of the gain can cause c_n to vanish when n is equal to the mean photon number. In that case, the final state will have an asymmetric probability amplitude in the number state basis as illustrated in Fig. 3.2. This allows the final state $|\psi\rangle$ to be chosen to be orthogonal to the coherent state $|\alpha/g\rangle_s$, which may be useful in generating two orthogonal states for use as a qubit, for example.

We will now show that a displaced number state can be produced by choosing a value of the gain given by

$$g = g_0 \equiv \frac{1}{\sqrt{1 - 1/|\alpha|^2}}. \tag{3.12}$$

A displaced numbers state has the property that it is orthogonal to the corresponding coherent state, which may be a useful way to represent two orthogonal qubits. Inserting the value of the gain from Eq. (3.12) into Eq. (3.11) gives

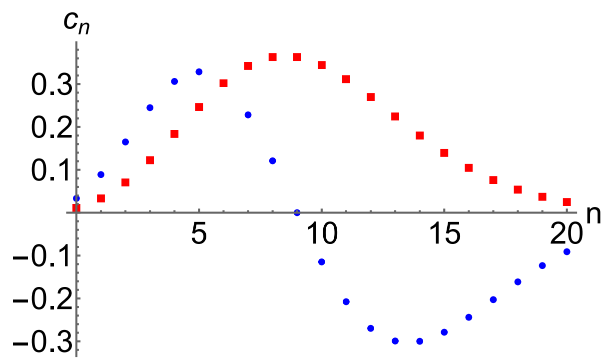

Figure 3.2 Coefficients c_n in the expansion of two states of interest in a basis of number states $|n\rangle$. The plot with red square markers shows the coefficients c_n for an attenuated coherent state for the case of $|\alpha|^2 = 10$, with g_0 given by Eq. (3.12).The plot with blue circle markers shows the coefficients c_n of the final post-selected state for a value of the gain $g = g_0$, which causes the final state to be orthogonal to the attenuated coherent state $|\alpha/g\rangle$. It can be seen that the cancellation of the two terms on the right-hand side of Eq. (3.9) gives $c_n = 0$ near the center of the $|\alpha/g_0\rangle$ distribution, so that the final state is approximately asymmetric about the mean photon number. The final state in this case is a displaced single photon state.

$$| \psi\rangle_{g_0} = -\left(\frac{|\alpha|^2}{\alpha^*}\right)\left(\frac{\alpha^*}{g_0} - \hat{a}^\dagger\right)\left|\alpha/g_0\right\rangle_s. \tag{3.13}$$

This state can be simplified by making use of the displacement operator $\hat{D}(\alpha)$ defined as usual by

$$\hat{D}(\alpha) = e^{\alpha\hat{a}^\dagger - \alpha^*\hat{a}}, \tag{3.14}$$

which has the property that [64]

$$\hat{D}(\alpha)|0\rangle = |\alpha\rangle. \tag{3.15}$$

The displacement operator satisfies the following commutation relationship with the photon creation operator [64]

$$[\hat{a}^{\dagger}, \hat{D}(\alpha)] = \alpha^* \hat{D}(\alpha). \tag{3.16}$$

Eqs. (3.15) and (3.16) allows the $\hat{a}^{\dagger} \mid \alpha/g_0\rangle_s = \hat{a}^{\dagger}\hat{D}\left(\alpha/g_0\right)|0\rangle_s$ term in Eq. (3.13) to be rewritten in the opposite order of the operators. The commutator cancels the α/g_0 term in Eq. (3.13), which gives

$$\mid \psi\rangle_{g_0} = -\left(\frac{|\alpha|}{\alpha^*}\right)\hat{D}\left(\alpha/g_0\right) \mid 1\rangle_s. \tag{3.17}$$

Equation (3.17) shows that the post-selected amplifier produces a displaced number state as desired for this value of the gain.

Since $\hat{D}(\alpha)$ corresponds to a unitary transformation and $\langle 1|0\rangle = 0,$ the displaced number state produced in this way is orthogonal to the corresponding coherent state $\left|\alpha/g_0\right\rangle_s$. The orthogonality of these two states can be understood from the asymmetric nature of the amplitudes c_n in the photon number basis as shown in Fig. 3.2.

The displaced number state $|\psi\rangle_{g_0}$ also has the interesting property that it has the same average photon number as the initial coherent state in the input to the optical parametric amplifier. This can be shown by rearranging Eq. (3.12) into the form

$$\left|\alpha/g_0\right|^2 = |\alpha|^2 - 1. \tag{3.18}$$

The average photon number for a displaced photon number state is given by [64]

$$\langle \hat{n} \rangle_{\hat{D}(\alpha')|n\rangle} = n + |\alpha'|^2 . \tag{3.19}$$

Combining Eqs. (3.18) and (3.19) for $n = 1$ and $\alpha' = \alpha/g$, we see that the average photon number remains unchanged for $g = g_0$.

However, the variance in the photon number for the output state $|\psi\rangle_{g_0}$ is different from the input state. The variance for a displaced number states is given by [64]

$$\mathrm{Var}(n)_{\hat{D}(\alpha')|n\rangle} = (2n+1)|\alpha'|^2 . \tag{3.20}$$

Combining Eqs. (3.18) and (3.20) gives a photon-number variance of $3|\alpha/g_0|^2 = 3|\alpha|^2 - 3$.

We have shown that a gain of $g = g_0$ gives a displaced number state with $n = 1$. We will now consider an arbitrary value of the gain and show that there is no contribution from displaced photon number states with photon number greater than 1. Using Eq. (3.16) in Eq. (3.11) allows the final state to be written in the form

$$|\psi\rangle = \frac{1}{\sqrt{N}}\left[\left(\frac{1}{g^2} - \left|\frac{\alpha}{g}\right|^2 G^2\right)\left|\frac{\alpha}{g}\right\rangle - \frac{\alpha}{g} G^2 \left|\frac{\alpha}{g},1\right\rangle\right], \tag{3.21}$$

where we have used the notation $\hat{D}(\alpha)\,|\,n\rangle = |\,\alpha, n\rangle$ and

$$N \equiv \left(\frac{1}{g^2} - \left|\frac{\alpha}{g}\right|^2 G^2\right)^2 + \left|\frac{\alpha}{g}\right|^2 G^4. \tag{3.22}$$

Equation (3.21) shows that the final signal state completely lies in the subspace of only two orthogonal states – the attenuated coherent state $|\alpha/g\rangle$ and the corresponding displaced single photon state.

3.3 Photon-added states

We showed in the previous section that the post-selection process can produce a displaced number state that is orthogonal to a coherent state. We now show that the post-selection process can also produce a photon added state in the limit of large gain.

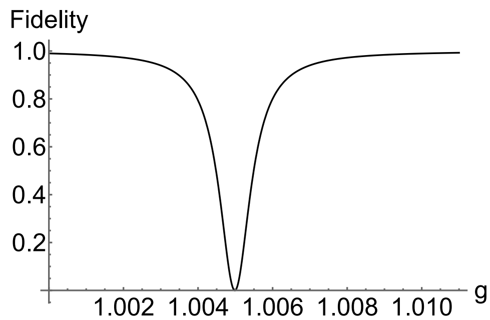

Figure 3.3 A plot of the magnitude squared of the inner product of the output state with a photon-added state proportional to $\hat{a}^\dagger \left|\alpha/g\right\rangle$. The inner product is plotted as a function of the gain g with $\alpha = 10$ $(n = 100)$. It can be seen that the output state approaches a photon-added state in the limit of large gain, and that there is a gain $g = g_1$ where the output is orthogonal to a photon-added state.

This can be seen intuitively from Eq. (3.9), where the G^2/g term becomes much larger than the $1/g^2$ term in the limit of large gain. As a result, the first term can be neglected in that limit and the second term gives a photon added state proportional to $\hat{a}^\dagger \left|\alpha/g\right\rangle$. Figure 3.3 shows a plot of the absolute value squared of the inner product between the final state and a single-photon added coherent state. The inner product approaches unity in the limit of large gain, which shows that the post-selected amplifier can generate a photon-added state in that limit as expected.

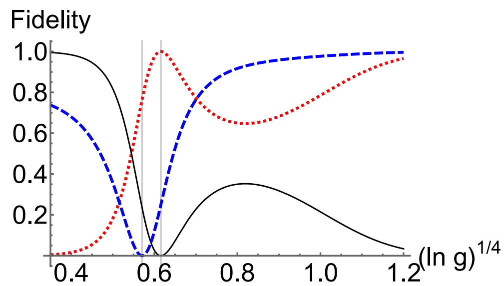

Figure 3.4 Magnitude squared of the projection of the final state onto specific quantum states with $\alpha = 2$. The solid black line shows the projection onto an attenuated coherent state, while the dashed blue line shows the projection onto a photon-added coherent state. The dotted red line shows the projection onto a displaced photon number state. Values of the gain g where the final state is orthogonal to an attenuated coherent state, or a photon added state can also be seen. A logarithmic scale for the gain has been used to illustrate all the relevant features.

It can also be seen from Fig. 3.3 that the inner product vanishes for a specific value of the gain $g = g_1$ where

$$\langle \alpha/g_1 | \hat{a} | \psi \rangle = 0. \tag{3.23}$$

We can determine the value of g_1 by combining Eq. (3.23) with the requirement that the gain be real and greater than or equal to 1. It can be shown that this occurs for

$$g = g_1 \equiv \sqrt{1 + \left(-|\alpha|^2 + \sqrt{|\alpha|^4 + 4}\right)/2}. \tag{3.24}$$

Thus, the final state is orthogonal to the photon added state proportional to $\hat{a}^\dagger \left|\alpha/g\right\rangle$ for this value of the gain. The orthogonality of these two states may also be useful for generating continuous-variable qubits with two orthogonal states.

The contributions to the final state from an attenuated coherent state, a photon added state, and a displaced number state are summarized in Fig. 3.4, where the square of the projection of the final state onto these states is plotted over a relatively large range of the gain. It can be seen that there are values of the gain where the output state is purely a coherent state, a displaced number state, or a photon added state. In addition, it can be seen that the output is orthogonal to an attenuated coherent state or a photon added state for values of the gain equal to g_0 and g_1, respectively.

3.4 Husimi- Kano Q-functions

The Husimi-Kano Q-function [65,66] provides a convenient tool for visualizing the properties of quantum states as well as for calculating the expectation value of observables. For a single mode of the field, the Q-function $Q(\alpha)$ is defined as

$$Q(\alpha) = \langle\alpha|\hat{\rho}|\alpha\rangle/\pi, \tag{3.25}$$

where $\hat{\rho}$ is the density operator of the state. The Q-function corresponds to the diagonal matrix elements of the density operator in a basis of coherent states. For pure states, which we have here, this becomes

$$Q(\alpha) = \left|\langle\alpha|\psi\rangle\right|^2/\pi, \tag{3.26}$$

where $|\psi\rangle$ is given by Eq. (3.21).

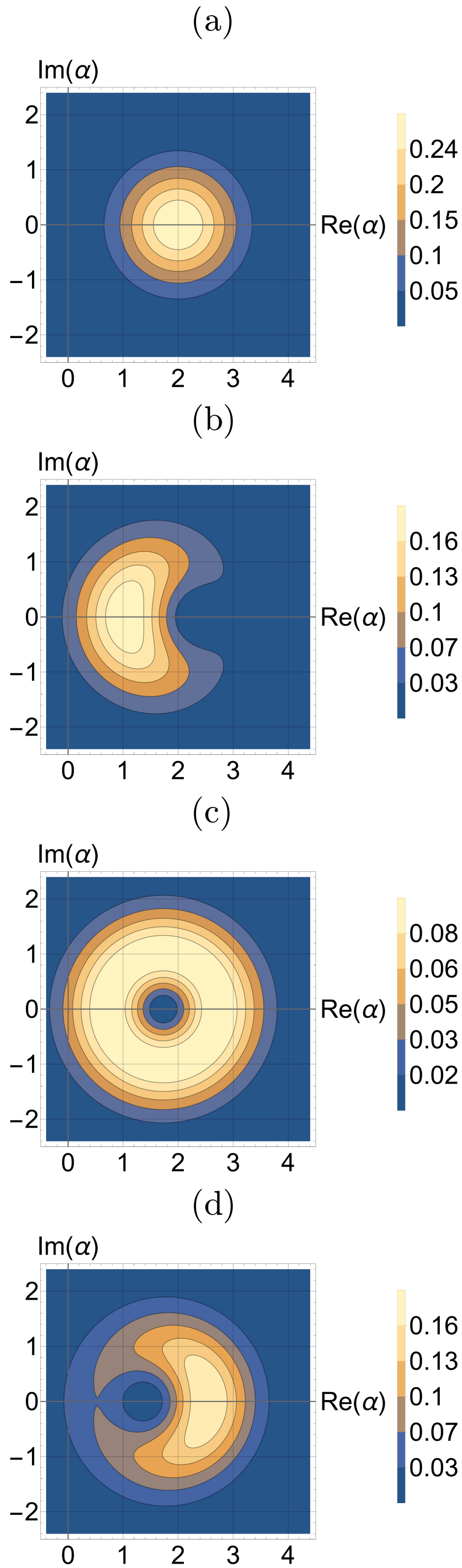

Figure 3.5 Contour plots of the Q-function of the output state for an initial amplitude of $\alpha = 2$ for various amplifier gain values. (a) $g = 1$. This corresponds to the input coherent state. (b) $g = g_1 = 1.111$. This state is orthogonal to a photon added coherent state with an amplitude attenuated to α / g_1. (c) $g = g_0 = 1.154$. This is a displaced single photon state with the amplitude of displacement attenuated to α/g_0. (d) $g = 1.195$. This is an arbitrary state with a larger gain, which approaches a photon-added state in the limit of large gain.

Figure 3.5 shows a plot of the Q-function for some specific values of the amplifier gain. Fig. 3.5(a) shows the Q-function for the initial coherent state $|\alpha\rangle$ corresponding to a gain of unity, while Fig. 3.5(b) shows a state that is orthogonal to a photon added state at a gain of $g = g_1 = 1.111$. The Q-function for a displaced number state that occurs at a gain of $g = g_0 = 1.154$ is shown in Fig. 3.5(c), and an arbitrary state at a higher gain of $g = 1.195$ is shown in Fig. 3.5(d); the output state approaches a photon-added state in the limit of large gain. All these plots correspond to a coherent state amplitude of $\alpha = 2$, but similar results are obtained for other values of α.

Figure 3.5 exhibits the wide range of quantum states that can be produced using the post-selected amplifier illustrated in Fig. 3.1. It can be shown from Eq. (3.9) that cancellation between the $1/g^2$ and G^2 terms will cause the probability amplitude c_n in a number-state basis to vanish at a particular value n_0 given by

$$n_0 = \frac{1}{g^2 G^2}. \tag{3.27}$$

It can also be shown that the Q-function vanishes at a coherent state amplitude α^* given by

$$\alpha^* = \frac{n_0}{\beta/g}. \tag{3.28}$$

The zero in the Q-function indicates that the state is orthogonal to the corresponding coherent state $|\alpha^*\rangle$. As the gain is increased for a fixed input signal amplitude, the zero can be seen to move inwards from infinity towards the origin. This can be viewed as a generalization of the orthogonality of the displaced number state of Eq. (3.17) to the coherent state $|\alpha/g_0\rangle_s$. It is consistent with the fact that, in the limit of large gain, the state becomes a single photon state that is orthogonal to the vacuum state. Roughly speaking, the existence of the zero in the Q-function corresponds to the orthogonality of the asymmetric c_n coefficient in Fig. 3.2 to a particular coherent state.

3.5 Experimental considerations

In any practical implementation of this approach, it will be essential to consider the effects of experimental errors such as photon loss, detector dark counts, and limited detector efficiencies. To analyze the effects of these experimental errors, we will consider the specific implementation shown in Fig. 3.6.

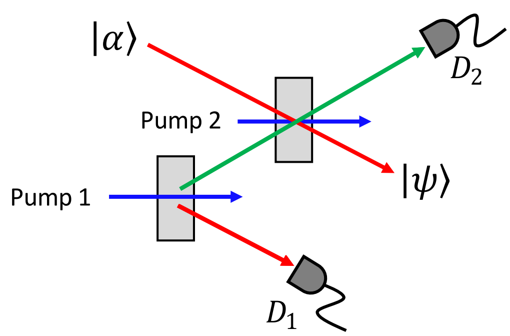

Figure 3.6 Possible experimental setup for the generation of a continuous range of quantum states. The single photon required for input to the idler mode of an optical parametric amplifier (OPA) is generated by spontaneous parametric down-conversion (SPDC) in the lower nonlinear crystal which is pumped by a laser. The detection of a single photon in detector D_1 located in one of the output modes of the SPDC crystal heralds the presence of a single photon in the other mode. The single photon then enters a second nonlinear crystal used as an OPA, which is pumped by a second laser. The gain of the OPA can be varied by controlling the intensity of the second laser, which allows a continuous range of quantum states to be generated.

It will be assumed that the single photon input to the idler mode of the optical parametric amplifier in Fig. 3.1 is generated in one of the two output modes of a spontaneous parametric down conversion crystal (SPDC) as shown in Fig. 3.6. The presence of the single photon is heralded by post-selecting on a detection event in the other output path of the SPDC. We will assume that the spontaneous parametric down conversion process generates only a single pair of entangled photons at a time, which is a good approximation when the intensity of the laser used as a pump for the nonlinear crystal is sufficiently low. With this assumption, the only error in heralding a single photon is due to the dark counts in detector D_1.

Post-selecting on the case in which a single photon is present in the output of the idler mode of the optical parametric amplifier in Fig. 3.1 will require a number resolving detector D_2 as shown in Fig. 3.6. Here a dark count in detector D_2 will produce an error in which it is assumed that an idler photon was present even when there were none. In addition, limited detection efficiency in detector D_2 can produce an error in which it was concluded that one idler photon was present even though there were actually two or more. Errors of that kind are equivalent to photon loss combined with a perfect detection efficiency.

We will assume that there is negligible probability that higher photon number states $(n \geq 3)$ will falsely indicate that a single photon was present in detector D_2, which is a good approximation for relatively high detection efficiencies. We will also assume that there is negligible probability of having a dark count and a photon loss simultaneously. With these assumptions, we will denote the dark count probability in both detectors by d and the probability that a photon count is lost (due to detector inefficiency or actual photon loss) by a probability of l.

The fidelity F of the final mixed state $\hat{\rho}$ with the ideal output state $|\psi\rangle$ of Eq. (3.9) is defined as

$$F = \langle\psi|\hat{\rho}|\psi\rangle. \tag{3.29}$$

F can be written as a sum of terms corresponding to the inner products of $|\psi\rangle$ with the various states that are actually present in the output when a dark count or photon loss occurs. There are six different possibilities that could contribute significantly to an outcome in which both detectors appear to register a single photon. These outcomes will be labelled (0, 0), (0, 1), (0, 2), (1, 0), (1, 1) and (1, 2), where the first and second entries denote the actual photon number in the input and output modes of the amplifier respectively. For example, (0, 0) is an event in which two dark counts occurred, while (1, 1) corresponds to the case in which both detectors functioned correctly.

All six of these states can be calculated using techniques similar to those described above. The outcome (0, 0) corresponds to the noiseless attenuation of an input coherent signal state $|\alpha\rangle$ to $|\alpha/g\rangle$ as shown in Ref. [59]. The state (0, 1) corresponds to photon addition on $|\alpha/g\rangle$ while (1, 0) corresponds to $|\alpha/g\rangle$ itself. All six of these states can contribute to the fidelity in general since none of them are orthogonal to $|\psi\rangle$ for an arbitrary value of the gain.

The states (0, 2) and (1, 2) can also be calculated using similar techniques but they have a relatively complicated form. For simplicity, we can calculate a lower bound on the fidelity by assuming that the states (0, 2) and (1, 2) are approximately orthogonal to the desired state $|\psi\rangle$. In that case, the lower bound on the fidelity is given by

$$
\begin{aligned}
F = {} & d^2 \left|\left\langle \phi_{(0,0)} \middle| \psi \right\rangle\right|^2 + d(1-d-l)\left|\left\langle \phi_{(0,1)} \middle| \psi \right\rangle\right|^2 \\
& +(1-d)d\left|\left\langle \phi_{(1,0)} \middle| \psi \right\rangle\right|^2 + (1-d)(1-d-l)\left|\left\langle \phi_{(1,1)} \middle| \psi \right\rangle\right|^2 .
\end{aligned}
\tag{3.30}
$$

Figure 3.7 shows the lower bound on the fidelity as a function of d for several values of l. We have also plotted the actual fidelity including the contributions from the states (0, 2) and (1, 2). Limited detection efficiency and dark counts can both have an effect on the fidelity.

The detectors used in pulsed down-conversion experiments have dark counts corresponding to d as low as 10^{-6}, so that dark counts should have a relatively small impact on the fidelity. Superconducting detectors can have efficiencies of about 95% $(l \leq 0.05)$ which would also have a minimal effect on the fidelity, whereas the more common silicon photo avalanche diodes can have detector efficiencies up to $\sim 74\%$ [67]. In both cases, the dominant error source is more likely to be actual photon loss due to coupling between fibers or absorption in filters.

3.6 Summary and conclusions

We have shown that post-selection on the idler mode of an optical parametric amplifier can generate a continuous range of quantum states with different properties. As illustrated in Fig. 3.1, a coherent state is assumed to be incident in the signal mode while a single photon is incident in the idler mode. Post-selection on a single photon emerging in the idler mode gives an output state whose properties depend on the gain of the amplifier. The states that can be generated in this way include a coherent state, a displaced number state, and a photon added state, along with a continuous range of states with intermediate properties.

One of the interesting features of this approach is that no photons are absorbed or emitted in the idler mode due to the post-selection process, and no photons are absorbed or emitted in the signal mode either since the photons are only absorbed or emitted in pairs. As a result, one might suspect that the amplifier has done nothing. Nevertheless, the post-selection process can change the probability amplitudes c_n of the state in a number-state basis, since different values of n will have different probability amplitudes for producing the post-selected output. In that respect, these results are somewhat similar to Ref. [68] in which they considered post-selecting on an ensemble of absorbing atoms, accepting only those events in which the atoms remained in their ground states. Although the atoms may appear to have done nothing, the post-selection process can increase the amount of absorption or even produce gain, depending on the strength of the interaction.

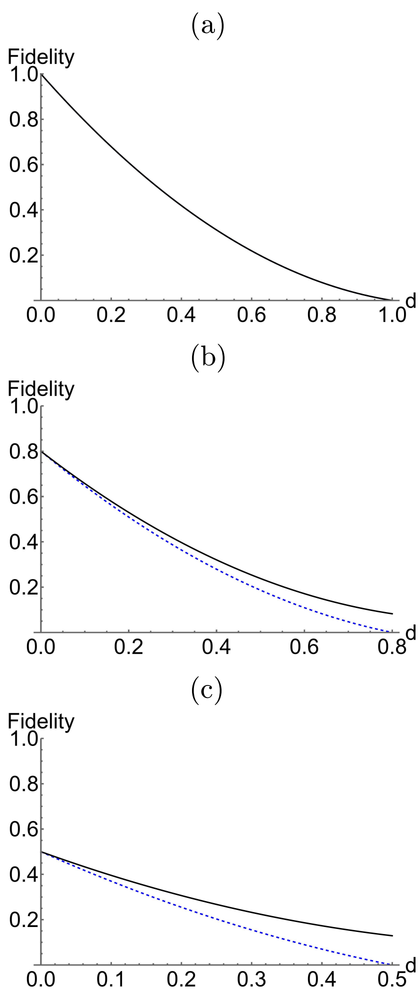

Figure 3.7 Fidelity of the output stated plotted as a function of the dark count probabilit d for several values of the loss probability l. The blue dashed curve shows the lower bound on the fidelity obtained by neglecting the contributions from the states $(0,2)$ and $(1,2)$ as described in the text. The black solid curve shows the actual fidelity without neglecting those terms. $\alpha = 2$ and $g = g_0(\alpha) = 1.154$ were chosen for the plots. (a) Loss probability $l = 0.0$. (b) $l = 0.2$ (c) $l = 0.5$.

The state produced by the post-selection process is orthogonal to a coherent state whose amplitude depends on the value of the gain. This can be understood as being due to cancellation between the two gain-dependent terms in Eq. (3.9), which produces an asymmetric dependence of the coefficient c_n as a function of n as illustrated in Fig. 3.2. A corresponding zero in the Q-function is apparent in Fig. 3.5. This orthogonality may be a useful property when using these states as continuous variable qubits.

It can be seen from Eq. (3.10) that the probability of success becomes exponentially small for coherent state inputs with a large amplitude since it becomes increasingly unlikely that one or more pairs of photons will not be emitted due to stimulated emission in the signal mode. This is one of the major open problems in quantum state engineering using conditional measurements. Nevertheless, this approach may have useful applications for moderate values of the gain and input coherent state amplitudes. The fidelity of the output state is primarily limited by photon loss or detector efficiency, but reasonably high values of the fidelity should be achievable.

Our analysis provides an interesting example of the variety of quantum states that can be obtained by varying the gain in a post-selected optical parametric amplifier. In addition, this approach may have practical applications for moderate values of α, since the gain and the output state can be continuously varied by adjusting the intensity of the pump beam. Two amplifiers can also be used in a somewhat similar technique to create entangled macroscopic states, in a future work.

Chapter 4 : Generating phase entangled Schrödinger cat states and violating Bell's inequality

This chapter is essentially taken from Ref. [69] that has been published in Physical Review A.

Quantum mechanics violates Bell inequality, which rules out the possibility of local hidden-variable theories [6,9,10,70,71] as an alternative to quantum mechanics. The earliest experimental tests of Bell's inequality were based on entanglement between the polarizations or spins of two particles [72-78]. It was subsequently shown that Bell's inequality could be violated using continuous degrees of freedom, such as energy-time entanglement combined with two distant interferometers [79]. Here we note that a photon number state incident on a balanced beam splitter will produce an entangled state in which the phases of the two output beams are highly correlated [80]. This entangled state can be viewed as a generalized Schrödinger cat state where there is an equal probability amplitude for all phases.

We show that Bell's inequality can be violated using this entangled state and two distant measurement devices. Each of the measurement devices consists of a single-photon interferometer with a Kerr medium in one path, a set of single-photon detectors, and post-selection based on a homodyne measurement. The use of post-selection suggests that the fair sampling assumption may be required for a violation of Bell's inequality. Somewhat surprisingly, we show that the fair sampling assumption is not required if the measurements are performed in the correct order. Like other Schrödinger cats, these states are highly sensitive to photon loss. A violation of Bell's inequality requires that either the photon loss is inherently small or its effects have been minimized using linear optics techniques based on post-selection [17].

It is well known that photon number states are highly nonclassical states of light [7] and that they are a useful resource for generating other kinds of nonclassical states. For example, a number state incident on a beam splitter has been used to herald an approximate cat state in one output mode by postselecting on the results of a homodyne measurement in the other output mode [81]. It has previously been shown that Bell's inequality can be violated using a variety of continuous variable states, homodyne measurements, or N00N states [82-85]. The approach described here is somewhat similar to earlier nonlocal interferometers [79,86], but the source of the entangled state is very different.

This chapter is organized as follows. Section 4.1 outlines the basic approach. Section 4.2 derives the form of the entangled cat state at the output of the beam splitter. The nonlocal interference effects that can be observed using this entangled state are calculated in Section 4.3. Section 4.4 shows that Bell's inequality can be violated provided that the effects of photon loss are sufficiently small. In Section 4.5, we show that the fair sampling assumption is not required if the measurements are performed in the correct order. Section 4.6 discusses an intuitive explanation for the origin of these effects, while Section 4.7 provides a summary and conclusions.

4.1 Basic approach

We consider a situation in which a photon number state $|N\rangle$ is incident on a beam splitter with 50% transmission and reflection as illustrated in Fig. 4.1. As will be shown in the next section, the output state $|\psi\rangle$ from the beam splitter corresponds to a superposition of identical coherent states in each of the output beams. Since photon number and phase are conjugate variables, the phase of the input number state is totally uncertain and the output state corresponds to a superposition of all possible coherent-state phases between 0 and 2π. The nonlocal properties of this entangled state are the main focus of this chapter.

We will show that the entangled state $|\psi\rangle$ can be used to violate Bell's inequality using two distant measurement devices as illustrated in Fig. 4.1. Each measurement device includes a single-photon interferometer (shown in red) with a Kerr medium in one of the two paths of the interferometer. The two output beams from the beam splitter also pass through the Kerr media, so that a phase shift will be applied depending on which path the single photons took. A fixed phase shift (not shown) is also included so that each of the beams will undergo a phase shift of $\pm\theta$. Single photon detectors D_1 through D_4 determine which path the single photons take when they leave the interferometers. Variable phase shifts σ_1 and σ_2 are also included in one path of the two interferometers as shown in Fig. 4.1.

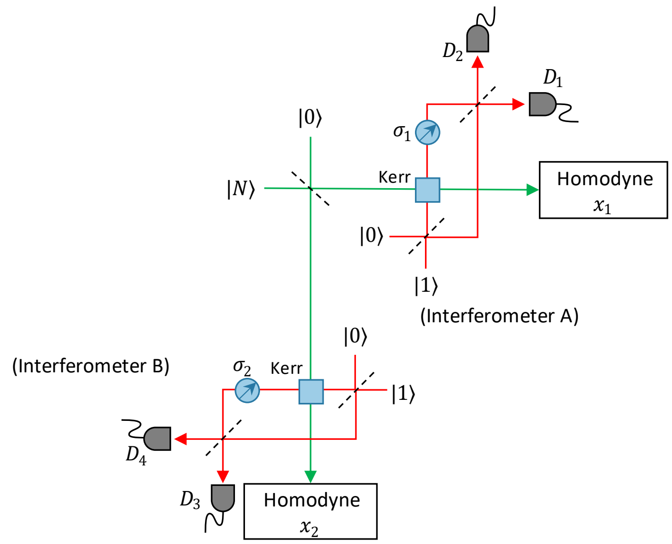

Figure 4.1 A number state $|N\rangle$ incident on a balanced beam splitter will produce two output beams that are entangled in phase. A phase shift of $\pm\theta$ is applied to each of the beams using a pair of single-photon interferometers A and B with a Kerr medium located in one path, combined with a constant bias phase shift (not shown). Variable phase shifts σ_1 and σ_2 are introduced into one path of the single-photon interferometers and their outputs are measured using single-photon detectors D_1 through D_4. After the two beams have passed through the single-photon interferometers, their quadratures x_1 and x_2 are measured using homodyne detectors. Those events in which x_1 and x_2 lie within a small range Δx centered about x_{1M} and x_{2M} are postselected. Bell's inequality can be violated in the usual way using the output of detectors D_1 through D_4 measured at four different settings of the parameters σ_1 and σ_2.

Homodyne measurements are used to determine the quadratures x_1 and x_2 of the two beams after they have passed through the single-photon interferometers. We postselect on events in which the measured value of x_1 lies within a small range Δx centered about some specific value x_{1M}, while x_2 lies in a range Δx about x_{2M}. The combination of a single-photon interferometer with a Kerr medium in one path, the single-photon detectors, and post-selection based on a homodyne measurement can be viewed as a compound measurement device. We will show that Bell's inequality can be violated in the usual way based on the output of the single-photon detectors D_1 through D_4 measured at four different settings of the parameters σ_1 and σ_2.

We will assume for the time being that the homodyne measurements are made after the single-photons have been detected in detectors D_1 through D_4, which simplifies the analysis. According to quantum mechanics, the same results would be obtained if the homodyne measurements were performed first. The advantages of the latter approach in ruling out hidden-variable theories will be discussed in Section 4.5.

The origin of these effects can be understood as being due to nonlocal quantum interference between two different probability amplitudes for obtaining quadrature measurements centered about x_{1M} and x_{2M}. This will be described in more detail in the discussion of Section 4.6 after we have calculated the properties of the system.

4.2 Entangled state after the beam splitter

The effect of a balanced beam splitter can be described as usual by the unitary transformation

$$\hat{a}_1^\dagger \rightarrow \left(\hat{a}_1^\dagger + i\hat{a}_2^\dagger\right)/\sqrt{2} \tag{4.1}$$

and

$$\hat{a}_2^\dagger \rightarrow \left(\hat{a}_2^\dagger + i\hat{a}_1^\dagger\right)/\sqrt{2}\,. \tag{4.2}$$

Here $\hat{a}_1^\dagger$ and $\hat{a}_2^\dagger$ are the photon creation operators in the two input/output modes and we have used the common convention that the reflected component undergoes a phase shift of $\pi/2$.

The initial state $|\psi\rangle$ incident on the beam splitter is given by

$$|\psi\rangle = |N,0\rangle, \tag{4.3}$$

where $|i,j\rangle$ will denote a state with i photons in one mode and j photons in the other mode. We will make use of the fact that a number state can be written as a superposition of coherent states [87]:

$$|N\rangle = \int_0^{2\pi} d\phi f_\phi \left|Re^{i\phi}\right\rangle. \tag{4.4}$$

Here f_ϕ is defined by

$$f_\phi \equiv \frac{e^{R^2/2} e^{-iN\phi}\sqrt{N!}}{2\pi R^N}, \tag{4.5}$$

and $\left|Re^{i\phi}\right\rangle$ denotes a coherent state with amplitude R and phase ϕ. R is an arbitrary constant, but it will be convenient to choose the value $R = \sqrt{N}.$

Eq. (4.4) can be used to rewrite the initial state of the system before the beam splitter as

$$|\psi\rangle = \int_0^{2\pi} d\phi f_\phi \left|Re^{i\phi},0\right\rangle. \tag{4.6}$$

Here $\left|Re^{i\phi},0\right\rangle$ denotes a coherent state with amplitude $Re^{i\phi}$ in one input to the beam splitter and a coherent state with zero amplitude in the other input port.

It is well known that a coherent state incident on a beam splitter will produce a coherent state in the two output modes with amplitudes equal to the corresponding classical fields. As a result, the beam splitter transforms the state of the system in Eq. (4.6) into

$$|\psi\rangle = \int_0^{2\pi} d\phi f_\phi \left|\frac{R}{\sqrt{2}}e^{i\phi},\frac{R}{\sqrt{2}}e^{i\phi}\right\rangle. \tag{4.7}$$

Here we have applied a phase shift of $-\pi/2$ in path 2 after the beam splitter to compensate for the factor of i on reflection that appears in Eq. (4.1) (This phase shift is not shown in Fig. 4.1).

The phase entanglement of the two beams is apparent in Eq. (4.7), which is qualitatively consistent with the results of Ref. [88] as well. All of the subsequent results can also be derived without using Eq. (4.4) by making use of the properties of the Hermite polynomials, as is described in the Appendix B.

4.3 Nonlocal interference

In this section, we will calculate the effects of the single-photon interferometers and show that there are two different probability amplitudes for obtaining homodyne measurement results of x_{1M} and x_{2M}. Quantum interference between these two probability amplitudes can violate Bell's inequality. For the time being, we will only consider the situation in which single photons are detected in D_2 and D_4, which shows the nonlocal dependence on the phase shifts σ_1 and σ_2 in a straightforward way. In the following section, we will generalize the results to include photons detected in any of the four detectors D_1 through D_4, which can then be used to violate Bell's inequality in the usual way.

The single-photon interferometers inserted into paths 1 and 2 will be labelled by A and B, respectively. The state $|i,j\rangle_A$ will denote the case in which there are i photons in the left path of interferometer A with j photons in the right path, while $|i,j\rangle_B$ will denote the corresponding state in interferometer B. Including the single photons, the complete state of the system before the photons have entered the interferometers is given by

$$|\psi\rangle = \int_0^{2\pi} d\phi f_\phi \left| \frac{R}{\sqrt{2}} e^{i\phi}, \frac{R}{\sqrt{2}} e^{i\phi} \right\rangle |10\rangle_A |10\rangle_B . \tag{4.8}$$

After the single photons have entered their respective interferometers and passed through the first beam splitter, the state of the system becomes

$$|\psi\rangle = \int_0^{2\pi} d\phi f_\phi \left| \frac{R}{\sqrt{2}} e^{i\phi}, \frac{R}{\sqrt{2}} e^{i\phi} \right\rangle \left(\frac{|10\rangle_A + i|01\rangle_A}{\sqrt{2}} \right) \left(\frac{|10\rangle_B + i|01\rangle_B}{\sqrt{2}} \right). \tag{4.9}$$

The presence of a single photon in the path with the Kerr media will produce a nonlinear phase shift and we assume that a constant phase shift is also applied so that the net phase shift is $\pm\theta$. As a result, the state of the system after the Kerr media can be written in the form

$$|\psi\rangle = \int_0^{2\pi} d\phi \frac{f_\phi}{2} \Big(|++\rangle_\phi |1010\rangle + i|+-\rangle_\phi |1001\rangle + i|-+\rangle_\phi |0110\rangle + i^2 |--\rangle_\phi |0101\rangle \Big). \tag{4.10}$$

Here we have introduced the notation

$$|+-\rangle_\phi \equiv \left| \frac{R}{\sqrt{2}} e^{i(\phi+\theta)}, \frac{R}{\sqrt{2}} e^{i(\phi-\theta)} \right\rangle, \tag{4.11}$$

with analogous definitions for $|-+\rangle_\phi$, $|++\rangle_\phi$, and $|--\rangle_\phi$. We have also used the more compact notation $|1010\rangle \equiv |10\rangle_A |10\rangle_B$, and so forth.

The single photons encounter the variable phase shifts σ_1 and σ_2 depending on which path they traverse as shown in Fig. 4.1. This transforms the state of Eq. (4.11) into

$$\begin{aligned}|\psi\rangle = \int_0^{2\pi} d\phi \frac{f_\phi}{2}\Big(& e^{i(\sigma_1+\sigma_2)}|++\rangle_\phi|1010\rangle + ie^{i\sigma_1}|+-\rangle_\phi|1001\rangle \\ &+ie^{i\sigma_2}|-+\rangle_\phi|0110\rangle + i^2|--\rangle_\phi|0101\rangle\Big).\end{aligned} \tag{4.12}$$

Finally, the single photons exit the interferometers through another set of beam splitters which gives the state

$$\begin{aligned}|\psi\rangle = \int_0^{2\pi} d\phi \frac{f_\phi}{4} \\ \times\Big(& e^{i(\sigma_1+\sigma_2)}|++\rangle_\phi\big(|1010\rangle + i|1001\rangle + i|0110\rangle + i^2|0101\rangle\big) \\ &+ie^{i\sigma_1}|+-\rangle_\phi\big(i|1010\rangle + |1001\rangle + i^2|0110\rangle + i|0101\rangle\big) \\ &+ie^{i\sigma_2}|-+\rangle_\phi\big(i|1010\rangle + i^2|1001\rangle + |0110\rangle + i|0101\rangle\big) \\ &+i^2|--\rangle_\phi\big(i^2|1010\rangle + i|1001\rangle + i|0110\rangle + |0101\rangle\big)\Big).\end{aligned} \tag{4.13}$$

The case in which single photons are detected in D_2 and D_4 corresponds to the state $|0101\rangle$. Postselecting on that outcome gives the following unnormalized final state

$$|\psi\rangle = i^2\int_0^{2\pi} d\phi \frac{f_\phi}{4}\Big(e^{i(\sigma_1+\sigma_2)}|++\rangle_\phi + e^{i\sigma_1}|+-\rangle_\phi + e^{i\sigma_2}|-+\rangle_\phi + |--\rangle_\phi\Big). \tag{4.14}$$

The four terms in Eq. (4.14) correspond to the possible phase shifts in the two beams before they enter the homodyne detectors.

A single mode of the electromagnetic field is mathematically equivalent to a harmonic oscillator, and a homodyne measurement of the x-quadrature can be represented by the operator $\hat{x} = \left(\hat{a} + \hat{a}^\dagger\right)/\sqrt{2}$ with a suitable choice of units. As a result, it is convenient to use the position representation, where the usual wave function $\psi(x)$ is given by

$$\psi(x) = \langle x | \psi \rangle. \tag{4.15}$$

It can be shown [89] that the wave function $\psi_c(x)$ for a coherent state $|\alpha_0 e^{i\phi}\rangle$ of the field corresponds to a Gaussian wave packet of the form

$$\psi_c(x) = \frac{1}{\pi^{1/4}} e^{ip_0 x} e^{-(x-x_0)^2/2} e^{-ix_0 p_0/2}. \tag{4.16}$$

Here $x_0 \equiv \sqrt{2}\alpha_0 \cos\phi$ and $p_0 \equiv \sqrt{2}\alpha_0 \sin\phi$. The overall phase factor of $e^{-ix_0 p_0/2}$ is sometimes ignored, but it plays an important role [90] in superposition states such as in Eq. (4.9).

In the coordinate representation, Eq. (4.14) gives

$$\psi(x_1, x_2) = \langle x_1, x_2 | \psi \rangle = \psi_{++}(x_1, x_2) + \psi_{--}(x_1, x_2) + \psi_{+-}(x_1, x_2) + \psi_{--}(x_1, x_2), \tag{4.17}$$

where $\psi_{\pm\pm}(x_1, x_2)$ correspond to the four terms in Eq. (4.14). It will be convenient to choose the phase shift θ so that $N\theta = m(2\pi)$, where m is an integer. In that case, Eqs. (4.13) and (4.16) can be used to show that

$$\begin{aligned} \psi_{++}(x_1, x_2) = &-\frac{1}{4\sqrt{\pi}} e^{i(\sigma_1+\sigma_2)} \int_0^{2\pi} d\phi \; f_\phi e^{iR\sin(\phi+\theta)x_1} e^{iR\sin(\phi+\theta)x_2} \\ &\times e^{-[x_1 - R\cos(\phi+\theta)]^2/2} e^{-[x_2 - R\cos(\phi+\theta)]^2/2} e^{-iR^2 \sin(\phi+\theta)\cos(\phi+\theta)}. \end{aligned} \tag{4.18}$$

with $N\theta = m(2\pi)$, $\psi_{--} = \psi_{++}$ aside from the phase shift of $e^{i(\sigma_1+\sigma_2)}$. The cross-terms are given by

$$\begin{aligned} \psi_{+-}(x_1, x_2) = &-\frac{1}{4\sqrt{\pi}} e^{i\sigma_1} \int_0^{2\pi} d\phi \; f_\phi e^{iR\sin(\phi+\theta)x_1} e^{iR\sin(\phi-\theta)x_2} \\ &\times e^{-[x_1 - R\cos(\phi+\theta)]^2/2} e^{-[x_2 - R\cos(\phi-\theta)]^2/2} e^{-i[R^2 \sin(\phi+\theta)\cos(\phi+\theta)]/2} e^{-i[R^2 \sin(\phi-\theta)\cos(\phi-\theta)]/2}, \end{aligned} \tag{4.19}$$

with a similar expression for ψ_{-+}.

The probability $P(x_{1M}, x_{2M})$ of obtaining quadrature measurements that lie within a small interval Δx about $x_1 = x_{1M}$ and $x_2 = x_{2M}$ is given by $P(x_{1M}, x_{2M}) = |\psi(x_{1M}, x_{2M})|^2 \Delta x^2$ (It is necessary to integrate over x_1 and x_2 for large values of Δx, as will be done in the following section). It is possible to choose values of x_{1M} and x_{2M} such that $\psi_{+-}(x_{1M}, x_{2M})$ and $\psi_{-+}(x_{1M}, x_{2M})$ are negligible. In that case, Eq. (4.18) and the corresponding equation for $\psi_{--}(x_{1M}, x_{2M})$ can be used to show that

$$P(x_{1M}, x_{2M}) = \left|\left(e^{i(\sigma_1+\sigma_2)}\right) + 1\right|^2 |\psi_{++}(x_{1M}, x_{2M})|^2 \Delta x^2 = \gamma \cos^2\left[(\sigma_1 + \sigma_2)/2\right]. \tag{4.20}$$

Here γ is a constant that depends on the choice of x_{1M}, x_{2M}, and Δx. The success rate for the post-selection process (coincidence counting rate) depends on the value of γ as will be discussed in the following section.

Eq. (4.20) shows that the coincidence measurements depend nonlocally on the sum of the phase shifts $\sigma_1 + \sigma_2$, which is characteristic of nonlocal interferometers such as that of Ref. [13]. A nonlocal interference pattern proportional to $\cos^2\left[(\sigma_1 + \sigma_2)/2\right]$ with a sufficiently high visibility indicates that Bell's inequality can be violated. This is shown to be the case in more detail in the following section.

4.4 Violations of Bell's inequality

The simple form of Eq. (4.20) depends on the assumption that the cross-terms $\psi_{+-}(x_{1M}, x_{2M})$ and $\psi_{-+}(x_{1M}, x_{2M})$ can be neglected. In order to investigate this possibility, the value of $|\psi_{++}(x_{1M}, x_{2M})|^2 = |\psi_{--}(x_{1M}, x_{2M})|^2$ is plotted as a function of

x_1 and x_2 in Fig. 4.2(a). These results correspond to $N = 24$ and $\theta = \pi/4$, which satisfies the condition that $N\theta = m(2\pi)$. It can be seen that the phases of the two fields are highly correlated as expected. The magnitude squared of the wave function also shows an oscillatory behavior extending towards to the origin, which is due to the rapidly varying phase factor of $e^{-iN\phi}$ in the definition of f_ϕ.

For comparison, Fig. 4.2(b) shows the magnitude squared of the cross-terms $\left|\psi_{+-}(x_{1M}, x_{2M})\right|^2 = \left|\psi_{-+}(x_{1M}, x_{2M})\right|^2$ as a function of x_1 and x_2. A phase shift of $\theta = \pi / 4$ causes the phases of the two beams to become uncorrelated. In addition, the wave function is only appreciable inside a ring with a relatively narrow width. It can be seen that there are many choices of x_{1M} and x_{2M} where the cross-terms would be negligible compared to $\left|\psi_{++}(x_{1M}, x_{2M})\right|^2$, which would give high-visibility nonlocal interference as described by Eq. (4.20). There are also regions where $\left|\psi_{++}(x_{1M}, x_{2M})\right|^2$ is negligible compared to $\left|\psi_{+-}(x_{1M}, x_{2M})\right|^2$, which would also allow high-visibility quantum interference between the $\psi_{+-}(x_{1M}, x_{2M})$ and $\psi_{-+}(x_{1M}, x_{2M})$ terms.

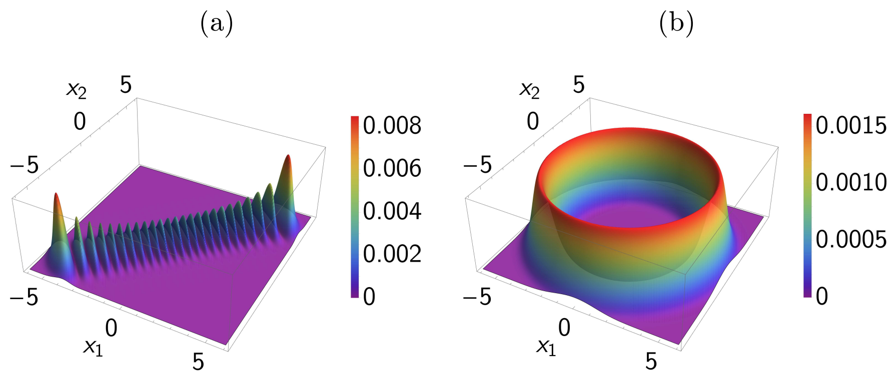

Figure 4.2 Plots of the magnitude squared of the wave function in the coordinate representation as a function of x_1 and x_2. (a) Plot of $\left|\psi_{++}\left(x_1,x_2\right)\right|^2=\left|\psi_{--}\left(x_1,x_2\right)\right|^2$. (b) Plot of the cross-terms $\left|\psi_{+-}\left(x_1,x_2\right)\right|^2=\left|\psi_{-+}\left(x_1,x_2\right)\right|^2$. These results correspond to $N=24$ and $\theta=\pi/4$ which satisfies the condition that $N\theta=m\left(2\pi\right)$ where m is an integer.

The normalized probability $P\left(x_{1M},x_{2M}\right)$ is shown in Fig. 4.3 as a function of the phase shift σ_1 in interferometer A for several values of the phase shift σ_2 in interferometer B. Here the postselected quadratures x_{1M} and x_{2M} were chosen to be $x_{1M}=x_{2M}=\sqrt{N}$, for which $\psi_{+-}\left(x_{1M},x_{2M}\right)$ and $\psi_{-+}\left(x_{1M},x_{2M}\right)$ are negligibly small. Bell's inequality [70] can be violated if the visibility of a nonlocal interference pattern of this kind is greater than $1/\sqrt{2}$ [91], which is the case for the results shown in Fig. 4.3.

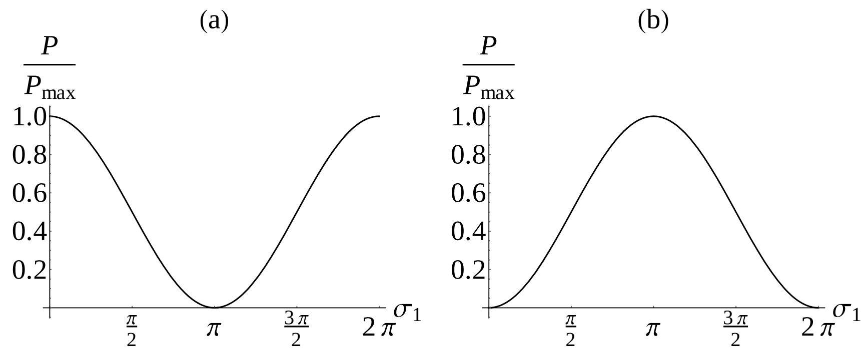

Figure 4.3 The normalized probability $P/P_{\max}$ of a postselected event for $x_{1M} = x_{2M} = \sqrt{N}$, plotted as a function of the phase shift σ_1 in interferometer A. (a) Phase shift $\sigma_2 = 0$ in interferometer B. (b) Phase shift $\sigma_2 = \pi$ in interferometer B. These nonlocal interference effects correspond to the same parameters as in Fig. 4.2 and they indicate that a violation of Bell's inequality should be possible.

There can be a significant contribution from the $\psi_{+-}(x_{1M}, x_{2M})$ and $\psi_{-+}(x_{1M}, x_{2M})$ terms for smaller values of N or θ. In that case, the interference pattern is no longer described by Eq. (4.20) and we must make use of the CHSH form of Bell's inequality introduced by Clauser, Horne, Shimony, and Holt [70]. We also need to generalize the results of the previous section to include the detection of single photons in any of the four detectors D_1 through D_4. The effects of photon loss will be neglected initially but then included later in this section.

The CHSH inequality requires two sets of measurement settings, which will be denoted by $\sigma_1 = \sigma_A$ or σ_A' in interferometer A and $\sigma_2 = \sigma_B$ or σ_B' in interferometer B. The result a of the measurement obtained using $\sigma_1 = \sigma_A$ in interferometer A will be assigned the value $a = 1$ if a photon is detected in detector

D_1, while it will be assigned the value $a = -1$ if a photon is detected in detector $D_{2.}$ [3]. The results obtained in interferometer A using σ_A' will be denoted $a' = \pm 1$ in a similar way, while the results obtained in interferometer B will be denoted $b = \pm 1$ or $b' = \pm 1$, depending on the choice of σ_2. The values of $\psi_{\pm\pm}(x_1, x_2)$ corresponding to the various single-photon detector outcomes can be calculated in the same way as in the previous section with the addition of a factor of i when a single photon is reflected by a beam splitter.

The parameter S in the CHSH form of the inequality is then defined as

$$S \equiv \langle ab \rangle + \langle a'b \rangle + \langle ab' \rangle - \langle a'b' \rangle. \tag{4.21}$$

Here $\langle ab \rangle$ denotes the average product of the measurement results a and b, with a similar notation for the other three terms. The inequality $|S| \leq 2$ holds for all local hidden-variable theories.

In the example of interest here, the results are postselected on having obtained quadrature measurements of x_1 and x_2 within a range Δx of x_{1M} and x_{2M}. For small values of Δx, the properly normalized expectation values are therefore given by [70]

$$\langle ab \rangle = \frac{\left|\psi_{a=+1,b=+1}\right|^2 - \left|\psi_{a=+1,b=-1}\right|^2 - \left|\psi_{a=-1,b=+1}\right|^2 + \left|\psi_{a=-1,b=-1}\right|^2}{\left|\psi_{a=+1,b=+1}\right|^2 + \left|\psi_{a=+1,b=-1}\right|^2 + \left|\psi_{a=-1,b=+1}\right|^2 + \left|\psi_{a=-1,b=-1}\right|^2}, \tag{4.22}$$

with analogous results for the other expectation values. Here we have used the notation $\psi_{a=+1,b=+1} \equiv \left(\langle x_1, x_2 | \otimes {}_A\langle 10 | \otimes {}_B\langle 10 | \right) |\psi\rangle$ with a similar definition for the other three terms. The constant γ and the factors of Δx^2 cancel out of these results.

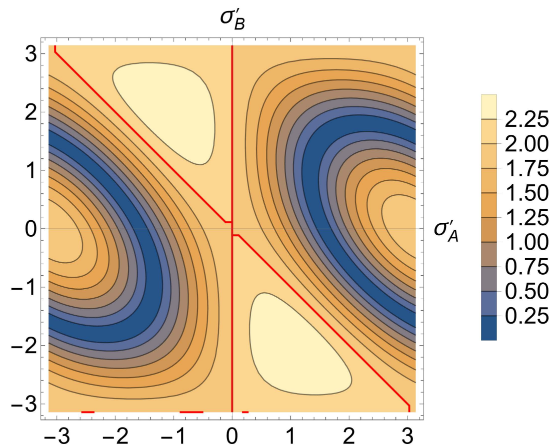

Figure 4.4 A plot of the absolute value of the CHSH parameter S as a function of the measurement settings σ_A' and σ_B'. The other measurement settings σ_A and σ_B were held fixed at values of 0 and π, respectively, while $N = 24$, $\theta = \pi/4$, and $x_{1M} = x_{2M} = \sqrt{N}$. There are large regions of the parameter space where $|S| > 2$ and the CHSH form of Bell's inequality is violated.

We will first consider the case in which the range Δx of accepted homodyne measurements is negligibly small. Fig. 4.4 shows a plot of $|S|$ as a function of σ_A' and σ_B', where the other measurement settings were held fixed at $\sigma_A = 0$ and $\sigma_B = \pi$. These results correspond to a relatively large photon number of $N = 24$ and $\theta = \pi/4$, as was used in Figs. 4.2 and 4.3. It can be seen that there are regions of the plot where $|S| > 2$ and Bell's inequality is violated, as would be expected from Fig. 4.3.

Fig. 4.5 shows a similar plot of $|S|$ for a more realistic value of $N = 4$. Although the interference pattern would no longer have the simple form shown in Eq. (4.20), it can be seen that there are still values of σ_A' and σ_B' where Bell's inequality can be violated.

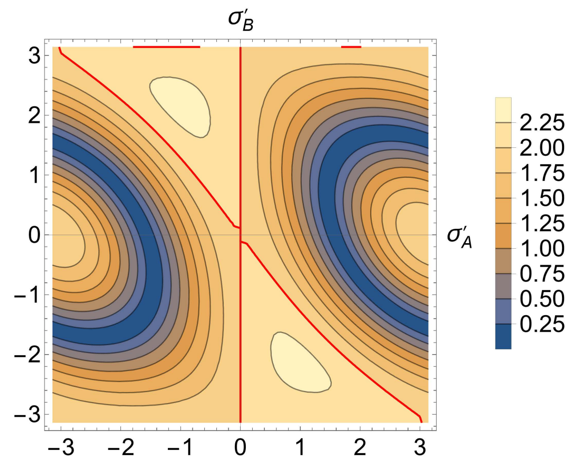

Figure 4.5 Another plot of the absolute value of the CHSH parameter S as a function of the measurement settings σ_A' and σ_B', where here the number of photons corresponds to $N = 4$. All of the other parameters are the same as in Fig. 4.4. It can be seen that there are still regions of the parameter space where $|S| > 2$ and the CHSH form of Bell's inequality is violated.

In order to obtain an acceptable counting rate in an experiment, it would be necessary to choose Δx to be a significant fraction of the overall range of the homodyne measurement results, such as $\Delta x = 0.10\sqrt{N}$. This choice of Δx can be shown to give a probability of success for the post-selection process of 0.27% per pulse for $N = 4$, for example. With $\sigma_A = 0, \sigma_A' = 0.9, \sigma_B = \pi$, and $\sigma_B' = -2.2$, this value of Δx gives a violation of Bell's inequality with $|S| = 2.3$. More generally, the maximum value of S is plotted in Fig. 4.6 as a function of N for several values of Δx. Here σ_A, σ_A', σ_B, and σ_B' were varied to optimize S. These results were obtained by integrating the magnitude squared of the wave functions in Eq. (4.22) over the relevant range of x_1 and x_2.

It can be seen from Fig. 4.6 that Bell's inequality can be violated for all values of N, including $N = 1$. The value of S is just above the hidden-variable limit of $S = 2$ for $N = 1$, and it gradually increases for larger values of N up to the maximum value allowed by quantum mechanics of $2\sqrt{2}$ (the Tsirelson bound). It can also be seen that Bell's inequality can be violated for relatively large values of Δx, which would result in reasonable values for the probability of success.

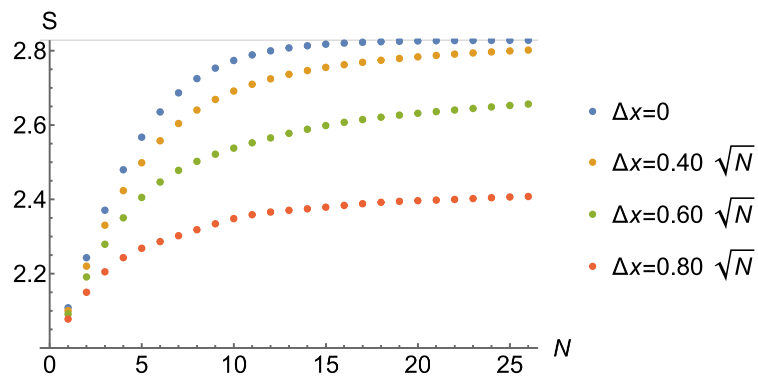

Figure 4.6 Plots of the maximum value of the CHSH parameter S as a function of the initial number N of photons incident on the first beam splitter. The results are shown for several different values of the range Δx of the homodyne measurement results that are accepted in the post-selection process. These results neglect photon loss.

The results shown above neglect the effects of photon loss. Schrödinger cat states are very sensitive to photon loss, and the loss of even a single photon will typically produce a substantial amount of decoherence. The effects of photon loss during transmission were evaluated by including an additional beam splitter in both paths after the initial beam splitter of Fig. 4.1. The reflected components of the two beams provide which-path information regarding their phases, which reduces the amount of quantum interference [92]. The maximum value of the CHSH parameter S is plotted in Fig. 4.7 as a function of the mean photon loss $\bar{n}$ for several values of N. It can be seen that Bell's inequality can no longer be violated for $\bar{n}$ greater than ~ 0.1 photons for $N = 1$ and ~ 0.2 for $N = 4$, while larger values of N allow a mean loss of ~ 0.3 photons. For a given channel loss, the value of $\bar{n}$ will be proportional to N, which favors the use of small values of N in an experimental test.

Although the violation of Bell's inequality is sensitive to photon loss, Ref. [17] has shown that an arbitrary quantum state can be transmitted through a lossy channel with negligible decoherence due to photon loss if the signal is noiselessly attenuated [17,59] before transmission, followed by noiseless amplification [93-95] after transmission. Roughly speaking, the noiseless attenuation can be used to reduce the intensity of the field to the point that the mean number of photons lost is much less than one and no significant which-path information is left in the environment. In principle, the phase-entangled states of interest here could violate Bell's inequality even after transmission through a lossy channel using techniques of that kind. Noiseless attenuation and amplification are both probabilistic, however, which results in an exponential reduction in the probability of success.

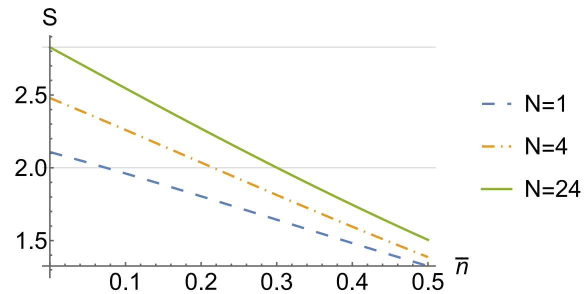

Figure 4.7 Maximum value of the CHSH parameter S as a function of the mean photon loss $\overline{n}$ for several values of the initial number N of photons. These results assume that Δx is negligibly small.

Another difficulty in an experimental test of Bell's inequality using this approach is the need to implement a Kerr phase shift at the single-photon level. Single-photon nonlinear phase shifts as large as $\pi/2$ have been demonstrated experimentally [30-37] but experiments of that kind remain challenging. Further improvements in those techniques would probably be required for the kind of experiments proposed here. Alternatively, a controlled phase shift (Kerr effect) can be implemented at the single-photon level using linear optics techniques [38,39].

4.5 Fair sampling assumption

The post-selection process based on the results of the homodyne measurements is required in order to violate Bell's inequality. As a result, one might suspect that the fair sampling assumption [96,97] may be needed. It will be shown in this section that the fair sampling assumption is not required provided that the homodyne measurements are completed before the phase shifts σ_1 and σ_2 are chosen at random. In that case, there is no opportunity for a hidden-variable model to bias the statistics as a result of the post-selection process.

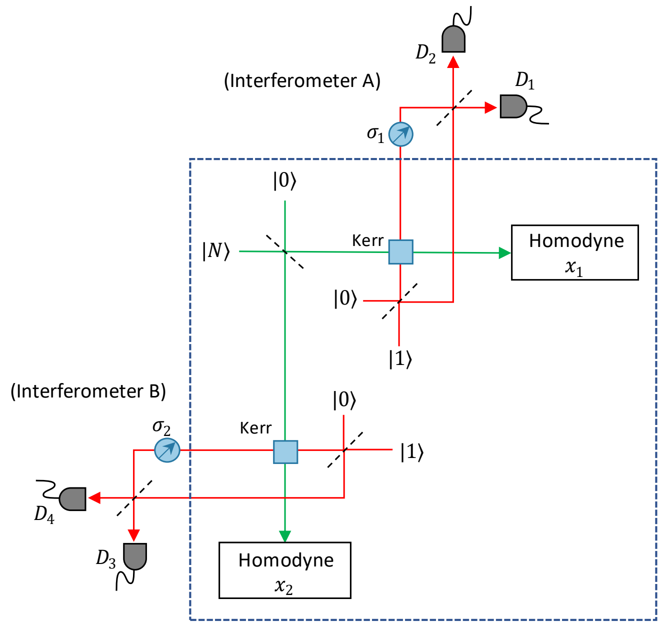

Figure 4.8 Modification of the apparatus shown in Fig. 4.1 to avoid the need for the fair sampling assumption as a result of post-selection. By extending the length of the interferometer arms, the homodyne measurement used for the post-selection process can be completed before the phase settings σ_1 and σ_2 are chosen at random. Under those conditions, a local hidden-variable theory cannot bias the statistics from detectors D_1' and D_2'. The combined system inside the dashed blue line can be viewed as a compound source that generates (heralds) the entangled states that are to be measured.

We have assumed up to now that the single-photon detection measurements in D_1 through D_4 were completed before the homodyne measurements in Fig. 4.1. That produces two possible phase shifts on beams 1 and 2 which give quantum interference effects in the subsequent homodyne measurements. But the results would be the same if the homodyne measurements were completed first, since the homodyne and single-photon detection measurements correspond to commuting operators. This can be accomplished by extending the length of the single-photon interferometers as illustrated in Fig. 4.8, which allows the settings of σ_1 and σ_2 to be chosen at random after the homodyne measurements have been completed.

Figure 4.9 compares the approach described here with a more conventional test of Bell's inequality using a pair of single-photon detectors with limited detection efficiency. Fig. 4.9(a) illustrates a conventional Bell's inequality experiment based on a pair of particles, such as two photons with entangled polarizations. In a local realistic theory, each photon is assumed to carry a set of hidden-variables $\{\lambda_i\}$ that are used to locally determine the outcome of two measurement devices with randomly-chosen settings θ_1 and θ_2, such as the orientation of two polarization analyzers. The two possible outcomes $a = \pm 1$ and $b = \pm 1$ of each measurement are then determined by single-photon detectors D_{1a}, D_{1b}, D_{2a}, and D_{2b} as previously described. The measurement outcomes $a\left(\theta_1, \{\lambda_i\}\right)$ and $b\left(\theta_2, \{\lambda_i\}\right)$ are functions of θ_1, θ_2, and $\{\lambda_i\}$ in a hidden-variable theory. Bell's inequality can be derived in the usual way if the detectors have 100% detection efficiency. But for limited detection efficiencies, a photon entering a detector could have a probability of being detected that depends on the settings θ_1 and θ_2. That would bias the statistical results and allow a hidden-variable theory to violate Bell's inequality [96,97]. That possibility can be ruled out by using the fair sampling assumption or by using detectors with sufficiently high detection efficiencies.

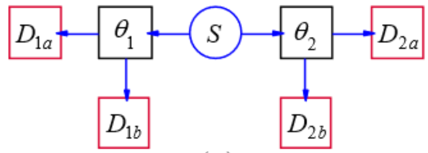

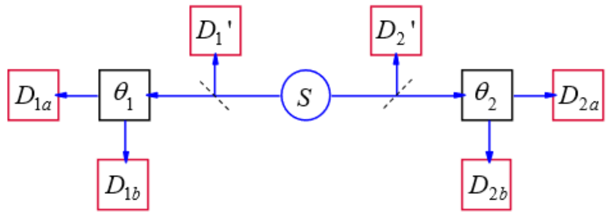

Figure 4.9 Comparison of a conventional test of Bell's inequality with the approach described in the text. (a) A conventional Bell inequality experiment in which a pair of entangled particles are created by a source S and propagate to two distant detectors with settings θ_1 and θ_2. The outcome of the measurements are recorded by detectors D_{1a}, D_{1b}, D_{2a}, and D_{2b} with limited detection efficiencies. Given that a photon enters one of the detectors, the detection probability could depend on θ_1 and θ_2 in a hidden-variable theory, which would bias the statistics and require the use of the fair sampling assumption. (b) The experiment of interest here, where the results are postselected based on the measurement outcomes in detectors D_1' and D_2'. The outcome of those measurements cannot depend on the choice of θ_1 and θ_2 if those measurements are completed before θ_1 and θ_2 are chosen at random. The fair sampling assumption would be required as usual if the detectors D_{1a}, D_{1b}, D_{2a}, and D_{2b} have sufficiently low efficiencies.

For comparison, the approach of interest here is illustrated in Fig. 4.9(b). The optical pulses leaving the source contain an indeterminate number of photons along with a set of hidden-variables $\{\lambda_i\}$ that are used to locally determine the outcome of any measurements in a local hidden-variable model. A beam splitter separates part of the signal in each path and sends it to homodyne detectors D_1' and D_2', whose outcome will form the basis for the post-selection process. The outcome of the post-selection process would be determined by the hidden-variables $\{\lambda_i\}$ in a local hidden-variable theory.

After the homodyne measurements D_1' and D_2' have been completed, the settings θ_1 and θ_2 in the two measurement devices are chosen at random. In our example, θ_1 and θ_2 correspond to the phase shifts σ_1 and σ_2 in the extended-length single-photon interferometers shown in Fig. 4.8. In a local hidden-variable theory, the measurement outcomes $a(\theta_1,\{\lambda_i\})$ and $b(\theta_2,\{\lambda_i\})$ are determined by a new set of hidden-variables $\{\lambda_i'\}$ that are consistent with the outcome from the first set of measurements in D_1' and D_2'. The probability distribution of these measurement outcomes can be viewed as conditional probabilities given the results obtained in D_1' and D_2'. In any event, the new hidden-variables $\{\lambda_i'\}$ must determine the outcome of the subsequent measurements as recorded by detectors D_{1a}, D_{1b}, D_{2a}, and D_{2b}, in complete analogy with the role of the hidden-variables $\{\lambda_i\}$ in the conventional Bell's inequality test of Fig. 4.9(a).

Bell's inequality can then be proven as usual, based on the fact that the $\{\lambda_i'\}$ must determine the outcome of the subsequent measurements. The usual proof relies only on the requirement that the probability distributions associated with the $\{\lambda_i'\}$ must be normalized to unity (i.e., the hidden-variable theory must always produce an outcome) with all probabilities in the range of 0 to 1 (no negative probabilities allowed).

The fair sampling assumption is not required for the post-selection process because the detection probabilities in D_1' and D_2' cannot depend on the subsequent choice of the settings σ_1 and σ_2. As a result, a hidden-variable model cannot take advantage of the limited detection efficiency of D_1' and D_2' to bias the statistics. That is not the case for the subsequent Bell-inequality measurement outcomes recorded by detectors D_{1a}, D_{1b}, D_{2a}, and D_{2b}, and the fair sampling assumption would still be required as usual if those detection efficiencies are sufficiently low.

The combined system consisting of the source S and homodyne detectors D_1' and D_2' can be viewed as an effective source that prepares an entangled state for a subsequent Bell inequality test. This is illustrated by the dashed-line box in Fig. 4.8. A compound source of this kind uses post-selection to herald when an entangled state is ready to be measured, after which the hidden-variables $\{\lambda_i'\}$ must determine the outcomes of the measurements. From a conceptual point of view, this can be viewed as either a state preparation process or a preselection of quantum states, rather than post-selection based on the results of the actual Bell-inequality test.

It can be seen from Eq. (4.7) that the post-selection process does not create the entanglement between the phases in the two beams, which already exists before any measurements are made. The post-selection provides a way to observe quantum interference between the probability amplitudes for states with different phases, which is required for a violation of Bell's inequality.

As a practical matter, the fair sampling assumption will be required in most experiments due to the limited detection efficiencies in D_{1a}, D_{1b}, D_{2a}, and D_{2b}. In that case, there is no need for the homodyne measurements to be space-like separated from the choice of σ_1 and σ_2, and the experimental apparatus of Fig. 4.1 would probably be easier to implement than the one in Fig. 4.8. The two experimental arrangements are equivalent according to quantum mechanics.

4.6 Discussion

The quantum interference responsible for the violation of Bell's inequality can be understood in an intuitive way if $N >> 1$. In that case, Eq. (4.7) describes a superposition of coherent states in each beam that is centered about a ring of radius $R = \sqrt{N}$ in phase space as illustrated in Fig. 4.10. The phases of the coherent states in the two beams are the same but totally uncertain, as illustrated by the red and blue circles.

A homodyne measurement on beam 1 will give a value of x_1 that corresponds to two possible values of the phase. For example, Fig. 4.11 illustrates the case where the measured value of x_1 is zero, which corresponds to a phase of $\pm\pi/2$. For simplicity, only the $\pi/2$ case is shown in the figure, where it is represented by a light blue circle. There are two ways of achieving a final phase of $\pi/2$. Both beams may have initially had a phase of $\pi/2-\theta$ followed by a phase shift of θ from the single-photon interferometers, which corresponds to the ψ_{++} amplitude. Or both beams may have initially had a phase of $\pi/2+\theta$ followed by a phase shift of $-\theta$ from the single-photon interferometers, which corresponds to the ψ_{--} amplitude. If the ψ_{+-} or ψ_{-+} amplitudes can be eliminated by the post-selection process, then the total amplitude for this process to occur is $e^{i(\sigma_1+\sigma_2)}\psi_{++}+\psi_{--,}$ Quantum interference between these two terms is responsible for the form of Eq. (4.20).

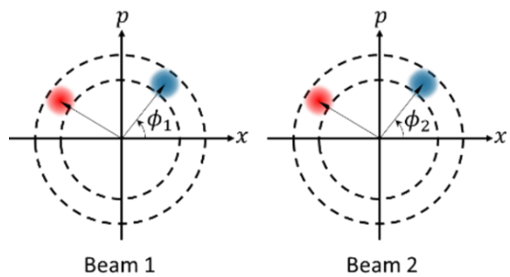

Figure 4.10 Interpretation of the phase-entangled state in Eq. (4.7) in phase space, where x and p represent the position and momentum in the Wigner distribution. There is an equal probability amplitude for all possible phases at a distance of $R=\sqrt{N}$ from the origin. The small circles represent the uncertainty in the quadratures of the coherent states. A phase measurement in beam 1 will collapse the states in the two beams to approximate coherent states with equal phases [14]. Two possible results are illustrated by the two sets of arrows. (Dimensionless units.)

The ψ_{+-} or $\psi_{-+.}$ amplitudes correspond to the case where one beam undergoes a phase shift of θ while the other beam undergoes a phase shift of $-\theta$. For $N >> 1$, those amplitudes do not overlap and they can be eliminated using post-selection as illustrated by the dashed open circles in Fig. 4.11. But for small values of N, the radius R will be reduced to the point that the uncertainty circles in Fig. 4.11 will overlap and the post-selection process is ineffective. This is responsible for the reduction in the value of S that can be seen in Fig. 4.6 for small values of N.

This interpretation is only approximately correct because of the uncertainty in the quadratures of a coherent state as well as the rapid variation in the factor of $\exp(-iN\phi)$ in the integral of Eq. (4.7). Nevertheless, it does provide some insight into the origin of these effects and it was the initial motivation for our interest in the system shown in Fig. 4.1.

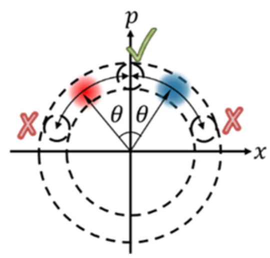

Figure 4.11 Nonlocal quantum interference produced by applying a phase shift of $\pm\theta$ to the two output beams from the initial beam splitter shown in Fig. 4.1. This can be done using two single-photon interferometers containing a Kerr medium in one path. In this example, the results are postselected on obtaining a homodyne measurement of $x = 0$ in both beams, which corresponds to a final phase of $\pm\pi/2$ (For simplicity, only the $\pi/2$ phase is shown.) One probability amplitude for this process to occur corresponds to an initial phase of $\pi/2+\theta$ in both beams, followed by a phase shift of $-\theta$ from the single-photon interferometers. A second probability amplitude corresponds to an initial phase of $\pi/2-\theta$ in both beams, followed by a phase shift of θ from the single-photon interferometers. Quantum interference between these two probability amplitudes can produce a violation of Bell's inequality. (Dimensionless units.)

4.7 Summary and conclusions

A photon number state is one of the most basic examples of a nonclassical state of light. A number state incident on a balanced beam splitter will produce two output beams that correspond to a superposition of identical coherent states in each beam. The phase of the coherent states is totally uncertain but the same in both beams. An entangled state of this kind can be viewed as a generalized form of a Schrödinger cat state with an equal probability amplitude for all phases.

Bell's inequality can be violated using this entangled state and two distant measurement devices. Each measurement device consists of a single-photon interferometer with a Kerr medium in one path, a set of single-photon detectors, and post-selection based on a homodyne measurement. The Kerr media produce a phase shift that depends on the path taken by the single photons through the interferometers. This gives two different probability amplitudes for obtaining the postselected value of the quadrature in the homodyne measurements. Nonlocal quantum interference between these probability amplitudes is responsible for the violation of Bell's inequality, which can occur for any number $N \geq 1$ of photons incident on the initial beam splitter.

Like other Schrödinger cats, these states are highly sensitive to photon loss. A violation of Bell's inequality requires that either the photon loss is inherently small or that its effects are minimized using linear optics techniques based on post-selection [16]. The decrease in the CHSH parameter S due to photon loss can be understood as being due to which-path phase information that is left in the environment.

The use of post-selection suggests that the fair sampling assumption may be required for a violation of Bell's inequality. We have shown that the fair sampling assumption is not required if the homodyne measurements are performed before the parameters σ_1 and σ_2 in the Bell-inequality measurements are chosen at random. Quantum mechanics predicts the same results regardless of the order of the measurements.

Somewhat similar violations of Bell's inequality have previously been proposed using entangled Schrödinger cat states [86,92]. The main difference is that most entangled Schrödinger cat states only contain a superposition of two possible phases, whereas the entangled state produced by a number state and a beam splitter contains a continuous range of possible phases. This approach provides a relatively straightforward way to produce entangled cat states, especially for small values of N.

In principle, this technique could be used to distribute entangled pairs of photons in the output of the single-photon interferometers, provided that the photon loss is sufficiently small. More importantly, a number state is one of the simplest forms of a nonclassical state and the fact that it can be used in this way to violate Bell's inequality is of fundamental interest.

Chapter 5 : Destructive controlled phase gate using linear optics

This chapter is taken from Ref. [14] that has been published in Scientific Reports.

A controlled-phase gate produces a phase shift ϕ when the control and target qubits both have a logical value of 1. This is a very useful operation since it is a universal gate for quantum computation when combined with single-qubit operations [98]. It can also be used to create Schrödinger cat states [99], to perform nonlocal quantum interferometry with violations of Bell's inequality [69,86], and to implement complete Bell state measurements in quantum teleportation [100,101], for example.

Knill, Laflamme, and Milburn (KLM) [13] showed that linear optics techniques could be used to implement a nonlinear sign gate. They also showed that two of their nonlinear sign gates could be combined to implement a controlled-phase gate. In this chapter, we propose an alternative implementation of a controlled-phase gate for a single-rail target qubit that only requires a single nonlinear sign gate. Since each operation of a nonlinear sign gate requires an ancilla photon, our approach requires one less ancilla photon than earlier approaches [13,102,103]. This gives a higher average probability of success when the required ancilla photons are generated using down-conversion and heralding techniques. The increased probability of success comes at the expense of destroying (erasing) the control qubit.

Logic gates in which the control qubit is destroyed have been used in a number of previous applications. For example, a destructive Controlled-NOT (CNOT) gate can be combined with a quantum encoder to implement a non-destructive CNOT gate [104-106]. The same devices can be used to implement fusion gates that allow the construction of a cluster state [107]. As another example, Bell's inequality can be violated in nonlocal interferometer experiments in which a controlled-phase shift is combined with homodyne measurements [69]. The control qubit is destroyed in a post-selection process in experiments of that kind, which allows the use of the controlled-phase gate described here.

There have been several demonstrations of controlled logic operations in the coincidence basis using dual-rail qubits or polarization encoding, including controlled-phase gates [105,108,109]. However, the coincidence basis cannot be used for the single-rail target qubits of interest in this chapter due to the superposition of the $|0\rangle$ and $|1\rangle$ Fock states in the input, which causes the total number of photons to be uncertain. The use of a single-rail target qubit is required for certain applications, such as in the interferometer of Ref. [86]. In addition, post-selection in the coincidence basis often destroys both the control and target qubits, whereas the event-ready approach described here only destroys the control qubit. Controlled phase gates for quantum computation applications have also been achieved using nonlinear interactions with trapped atoms [110-113], for example. In contrast, the controlled phase gate described here uses only linear optical elements.

In Section 5.1 we look at the nonlineat sign gate constructed using only linear optical elements and conditional measurements, as proposed by Knill, Laflamme and Milburn. Section 5.2 reviews their controlled phase gate that takes in dual-rail control and acts on a dual-rail target. In Section 5.3 we describe the proposed gate which takes a dual-rail control and acts on a single-rail target. Section 5.4 makes various comparisons between the two gates. In Section 5.3 we discuss implementing controlled phase shifts on coherent states with large amplitude and present a summary and our conclusions in Section 5.6.

5.1 Nonlinear sign gate

The nonlinear sign gate shown in Fig. 5.1 is the basic building block of the KLM approach to linear optics quantum computing [98]. The input state $|\psi_{in}\rangle$ is limited to at most two photons. The operation of the nonlinear sign gate is then defined by

$$|\psi_{in}\rangle = \alpha|0\rangle + \beta|1\rangle + \gamma|2\rangle \rightarrow \alpha|0\rangle + \beta|1\rangle - \gamma|2\rangle, \qquad (5.1)$$

where α, β, and γ are complex constants. The only effect of the nonlinear sign gate is to reverse the sign of the two-photon amplitude, which is similar to the effects of a nonlinear Kerr medium [94].

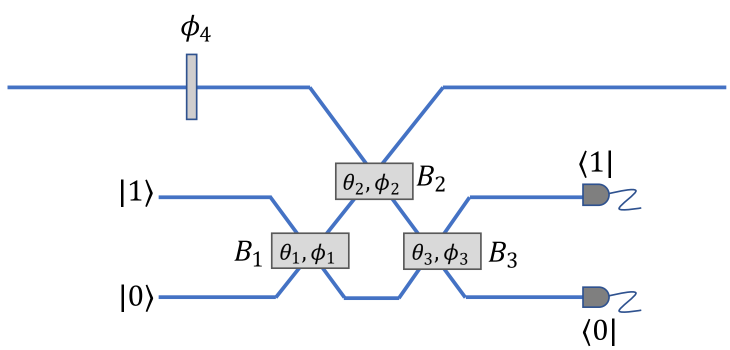

Figure 5.1 KLM nonlinear sign gate. An input state of the form $|\psi\rangle = \alpha|0\rangle + \beta|1\rangle + \gamma|2\rangle$ gives an output state $\alpha|0\rangle + \beta|1\rangle - \gamma|2\rangle$ for an appropriate choice of the transmission coefficients of the three beam splitters B_1, B_2, and B_3, along with a fixed phase shift ϕ_4. The results are heralded on the presence of a single photon in one of the two single-photon detectors

The KLM nonlinear sign gate utilizes three beam splitters, one ancilla photon, and post-selection based on the output of two single-photon detectors, as shown in Fig. 5.1. The gate applies a nonlinear phase shift of π as in Eq. (5.1) for an appropriate choice of beam splitters and linear phase shifters as shown in Fig. 5.1. Other choices of the parameters can also be used to implement a nonlinear phase shift of $\pi/2$, for example [13]. There have been several proposals to enhance the success rate of this gate at the expense of adding more resources [114,115] or vice-versa [116].

Costanzo et al. [94] proposed an alternative implementation of a nonlinear sign gate that is shown in Fig. 5.2. As illustrated in the left part of the figure, the device produces a coherent superposition of photon subtractions that occur either before or after a photon addition. The operation of the gate can be intuitively understood from the commutation relation $\left[\hat{a},\hat{a}^{\dagger}\right]=1$. This gate can be implemented using a down-conversion crystal with heralding to produce the photon addition, with photon subtraction occurring either at the first beam splitter B_1 or the second beam splitter B_2. Heralding on the output of beam splitter B_3 ensures that there is a fixed phase relationship between the two ways in which the photon subtraction can occur. The final state in this approach undergoes a noiseless amplification [94] in addition to the nonlinear sign shift. If necessary, this can be compensated using noiseless attenuation [17,117].

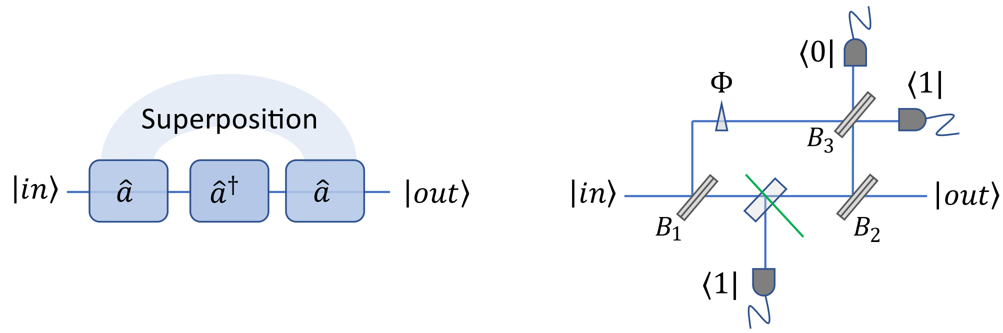

Figure 5.2 Alternative nonlinear sign gate suggested by Costanzo et al. A superposition of $\hat{a}\hat{a}^\dagger$ and $\hat{a}^\dagger\hat{a}$ operations is implemented using photon subtraction that occurs either at the first beam splitter B_1 or at the second beam splitter B_2. These operations cannot be distinguished when a single photon is detected in one of the outputs of the third beam splitter B_3. Photon addition is implemented in between B_1 and B_2 with the aid of a heralding signal from a down conversion process. A variety of nonlinear phase shifts can be achieved by adjusting the reflectivities of the three beam splitters along with an additional phase shift Φ.

Our destructive controlled-phase gate could be implemented using either the KLM nonlinear sign gate or the alternative implementation shown in Fig. 5.2. Our goal is to implement a controlled phase shift using only linear optical elements, whereas the approach shown in Fig.5.2 is based on the use of a nonlinear crystal. As a result, we will assume that the KLM approach is used for the nonlinear sign gate throughout the rest of this chapter.

5.2 KLM controlled-phase gate

The controlled-phase gate suggested by KLM is shown in Fig. 5.3. Dual-rail encoding is used for both qubits, and the two paths corresponding to a logical value of 1 are fed into a 50:50 beam splitter. Both outputs of the first beam splitter are passed through a nonlinear sign gate, after which they are recombined on a second beam splitter to form the output of the device.

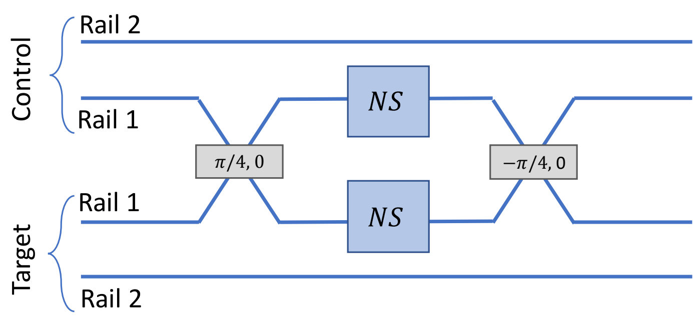

Figure 5.3 KLM Controlled-phase gate. Dual-rail encoding is combined with Hong-Ou-Mandel interference at the first beam splitter to apply a phase shift of π if both qubits have a logical value of 1. Two nonlinear sign gates labelled NS are required.

The operation of this device can be understood as being due to Hong-Ou-Mandel interference [118] at the first beam splitter. If both qubits have a logical value of 0, then no photons pass through the nonlinear sign gates and the device has no effect. If only one qubit has a logical value of 1, then a single photon passes through one of the nonlinear sign gates, which also has no effect. But if both qubits have a value of 1, then both of them will emerge in the same path after the first beam splitter as in the Hong-Ou-Mandel interferometer. In that case, one of the nonlinear sign gates will apply a phase shift of π as desired. The second beam splitter can be viewed as implementing the inverse of the Hong-Ou-Mandel interferometer with a single photon emerging in each path.

Other nonlinear phase shifts, such as $\phi = \pi/2$, can be produced by adding fixed phase shifts and varying the reflectivities of the beam splitters in the nonlinear sign gate from Fig. 5.1. E. Knill [102] has also described a somewhat a different implementation of a controlled-phase gate that also requires two ancilla photons as a resource.

5.3 Destructive controlled-phase gate

An alternative implementation of a controlled-phase gate that only requires a single nonlinear sign gate is shown in Fig. 5.4. In this case, we assume that a dual-rail encoding is used for the control qubit while a single-rail encoding is used for the target qubit. The two paths for the control qubit are incident on beam splitters B_1 and B_2, whose outputs are postselected on the absence of a photon to produce a photon addition at one of the two beam splitters. The path representing a logical value of 1 for the control qubit is assumed to be on the left-hand side of the figure, where it passes through beam splitter $B_{1.}$ A nonlinear sign gate is placed between the two beam splitters, after which beam splitter B_3 is used to subtract a photon.

The initial states $|\psi_T\rangle$ and $|\psi_C\rangle$ for the target and control qubits, respectively, will be denoted by

$$|\psi_T\rangle = \alpha|0_T\rangle + \beta|1_T\rangle, \; |\psi_C\rangle = \gamma|0_C\rangle + \delta|1_C\rangle, \tag{5.2}$$

where α, β, γ, and δ are complex constants. Here $|0_T\rangle$ and $|1_T\rangle$ represent the state of the target qubit containing zero or 1 photons, while $|0_C\rangle$ and $|1_C\rangle$ correspond to the dual-rail encoded states of the control qubit.

The basic idea behind the operation of the gate is illustrated in the left part of Fig. 5.4. If the control qubit has a logical value of 1, the photon addition occurs first and the state $|\psi_T'\rangle$ that passes through the nonlinear sign gate will contain two photons if the target qubit also has a logical value of 1. In that case, the nonlinear sign gate would produce a phase shift of π, after which the photon subtraction at beam splitter B_3 would restore the target qubit to its original number of photons. In all other cases, the state $|\psi_T'\rangle$, passing through the nonlinear sign gate would contain at most a single photon and no phase shift would be applied.

The transmission coefficients for the three beam splitters will be denoted by t_1, t_1, t_2, and t_3, while the corresponding reflection coefficients will be denoted by r_1, r_2, and r_3. If we apply the usual beam splitter transformation with a factor of i on reflection, the unnormalized state of the system at the output can be shown to be given by

$$|\psi'\rangle = \left(\alpha|0_T\rangle + \beta|1_T\rangle\right)|0_1\rangle|0_2\rangle|1_3\rangle, \tag{5.3}$$

where $|0_1\rangle$, $|0_2\rangle$ and $|1_3\rangle$ are the states at the three detectors that herald the target output. This state does not contain the states $|0_C\rangle$ and $|1_C\rangle$ of the control qubit because it is destroyed during the heralding process.

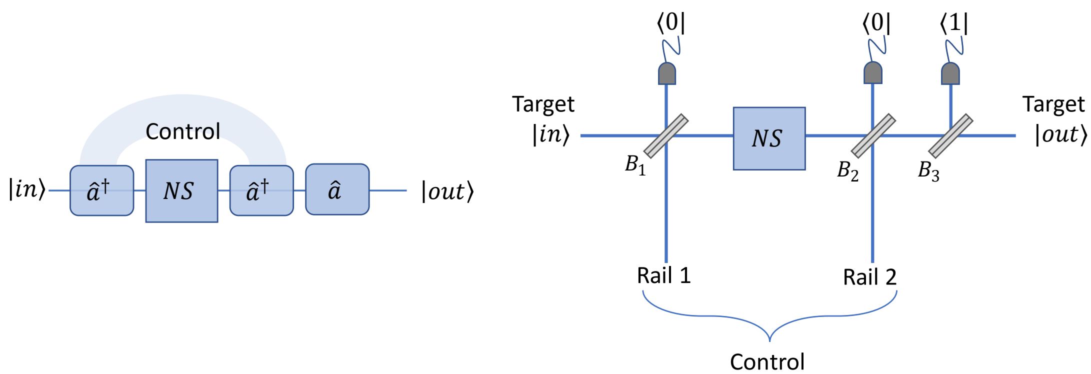

Figure 5.4 Destructive controlled-phase gate. Implementation of a destructive controlled-phase gate that only requires a single nonlinear sign gate labelled NS. If the control qubit has a logical value of 1, it produces a photon addition at beam splitter B_1. If the target qubit also has logical value of 1, two photons will then pass through the nonlinear sign gate and produce a phase shift of π. In all other cases, at most a single photon passes through the nonlinear sign gate and there is no effect on the state of the system. A photon subtraction at beam splitter B_3 restores the original number of photons to the target qubit. The events are heralded on the outputs shown in three single-photon detectors. The detector in one of the output ports of beam splitter B_3 is assumed to be a photon-number resolving detector.

This state can be put into the desired form by choosing the values of the transmission coefficients such that $2t_1t_2t_3 = 1$ and $r_2 = r_1t_2$. Equation (5.3) then reduces to

$$\left|\psi'\right\rangle = r_2r_3\left[\gamma\left(\alpha\left|0_T\right\rangle + \beta\left|1_T\right\rangle\right) + \delta\left(\alpha\left|0_T\right\rangle - \beta\left|1_T\right\rangle\right)\right], \tag{5.4}$$

where we have taken the projection onto the heralded state $\left|0_1\right\rangle\left|0_2\right\rangle\left|1_3\right\rangle$. The probability of success is given by $\left\langle\psi'\middle|\psi'\right\rangle$, which will depend on the value of the probability amplitudes in the initial state, as discussed in the next section.

Equation (5.3) gives a controlled phase shift of $\phi = \pi$ using the parameters described above. Other nonlinear phase shifts can be produced using different parameters in the nonlinear sign gate. It may be worth noting that the same gate can be implemented by interchanging the locations of the output target state and the third heralding detector if the transmission and reflectivity of the final beam splitter are also interchanged. The gate fidelity and the success probability will remain the same in that case because the two experimental arrangements are equivalent.

5.4 Performance comparison

The probability of success for the destructive controlled-phase gate proposed here will be compared to that of the original KLM controlled-phase gate in this section. The fidelity of both gates depends on the efficiency of the single-photon detectors used in the heralding process, and those efficiencies will also be compared.

One measure of the probability of success is to assume that the necessary ancilla photons are available with 100% probability and then calculate the intrinsic probability of success associated with the gate itself. But in many applications, the relevant probability of success would combine the intrinsic probability of success with the probability of generating the required ancilla photons using down-conversion and heralding techniques. Single photons can be generated using down-conversion with a very high fidelity, for example, which is essential in meeting the threshold for error correction.

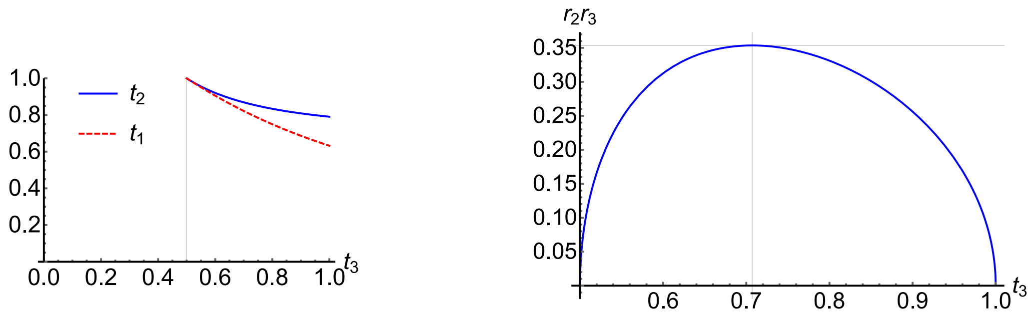

(a) (b)

Figure 5.5 Parameters used in the destructive controlled-phase gate. Plots of various parameters, as a function of the transmission coefficient t_3, satisfying the conditions $2t_1t_2t_3 = 1$ and $r_2 = r_1t_2$ required for the successful operation of the destructive controlled-phase gate. (a) Transmission coefficient t_1 (dashed red line) and t_2 (solid blue line). The plots suggest that t_3 cannot be less than 0.5 for a solution to exist. (b) Product r_2r_3 that appears in Eq. (5.5) for the probability of success. Maxima occurs at $t_3 = 1/\sqrt{2}$, which corresponds to using a 50-50 beam splitter in the photon subtraction.

We will first consider the probability of success for a controlled-phase gate with $\phi = \pi$. As was noted in the previous section, Eqs. (5.3) and (5.4) will give the desired result if we choose $2t_1t_2t_3 = 1$ and $r_2 = r_1t_2$, but those two equations do not completely determine the value of all three transmission coefficients. Fig. 5.5(a) shows the solutions for t_1 and t_2 as a function of t_3; the solutions only exist for $t_3 > 0.5$. It can be shown that the maximum probability of success occurs for $t_1 = \sqrt{2/3}$, $t_2 = \sqrt{3}/2$, and $t_3 = 1/\sqrt{2}$. This gives the maximum value of the coefficient r_2r_3 that appears in Eq. (5.4), as can be seen in Fig. 5.5(b).

From Eq. (5.4), the intrinsic probability P_D of success of the destructive controlled-phase gate is given by

$$P_D = P_{NSG} \langle \psi' | \psi' \rangle = P_{NSG} r_2^2 r_3^2 \left[1 + 2\left(|\alpha|^2 - |\beta|^2 \right) \mathrm{Re}\left(\gamma^* \delta \right) \right]. \tag{5.5}$$

where P_{NSG} is the probability of success for the nonlinear sign gate shown in Fig. 5.4. For the time being, we will assume that P_{NSG} is calculated based on the assumption that the ancilla photons are produced with 100% efficiency.

P_D depends on the values of the probability amplitudes α, β, γ, and δ that describe the initial control and target qubits. This is illustrated in Fig. 5.6, which is a plot of the intrinsic probability of success as a function of α and γ, where all of the probability amplitudes were assumed to be real with $\beta = \sqrt{1-\alpha^2}$ and $\delta = \sqrt{1-\gamma^2}$, for example. It can be seen that there is a significant variation in the probability of success depending on the form of the incident qubits.

If the target qubit has a logical value of 1 $(\alpha = 0)$ and $\gamma = \delta$, then it can be seen from Eq. (5.4) that the output state will have zero amplitude and $P_D = 0$, as can be seen in Fig. 5.6. This is an inherent feature of a destructive controlled-phase gate where the value of the control qubit is erased. This does not occur for other values of the controlled phase shift, such as $\pi/2$, and it is not an issue in nonlocal interferometer applications, for example [69,86].

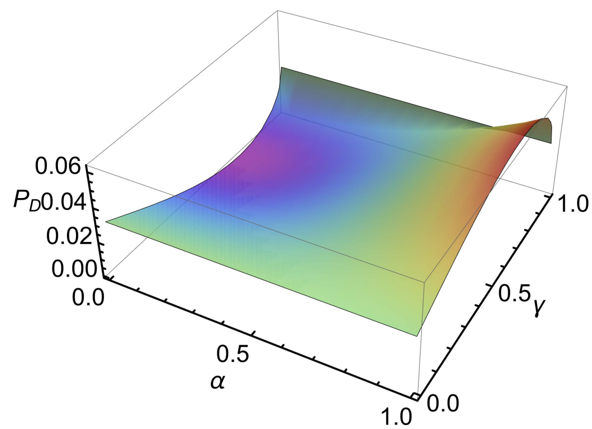

Figure 5.6 Intrinsic probability of success. Intrinsic probability of success P_D of the destructive controlled-phase gate as a function of the probability amplitudes α and γ in the incident control and target qubits. All four probability amplitudes in Eq. (5.3) were assumed to be real in this example. On the other hand, if we select β and δ to be imaginary, we get a probability independent of the real valued α and γ.

In order to simplify the comparison of the KLM controlled-phase gate and the gate proposed here, we averaged the intrinsic probability of success P_D over all possible values of the coefficients α, β, γ, and δ. This result is compared with the corresponding result P_{KLM} for the KLM controlled phase gate in Table 5.1. It can be seen that the intrinsic probability of success is comparable for the two gates for the case of $\phi = \pi$, which corresponds to a Controlled-Z operation.

Single photon ancilla can be generated using down-conversion and heralding on one of the pair of photons, which we will assume to succeed roughly 1% of the time [119]. Table 5.1 also includes the effective probabilities of success P_D' and P_{KLM}' for the two controlled phase gates if we include the probability of generating the required ancilla photons using down-conversion. It can be seen that $P_D' >> P_{KLM}'$ since the KLM gate requires two ancilla photons while the destructive controlled-phase gate only requires a single longer ancilla photon.

As described in the previous section, a destructive controlled-phase shift of $\phi = \pi/2$ can also be produced using a different set of parameters. The KLM gate can be modified to produce a phase shift of $\phi = \pi/2$ as well [13]. The probability of success for these two gates was calculated in the same way as before and the results are also compared in Table 5.1.

It can be seen that the destructive controlled-phase gate has a much higher average probability of success in this case as well if we include the probability of generating the required ancilla photons using down-conversion and heralding.

In principle, both types of gates can be operated with unit fidelity if the single-photon detectors are assumed to be perfect. The dark counts in an avalanche-diode single-photon detector are typically on the order of 100 counts/second or less. With a coincidence window of 1ns, this corresponds to an erroneous output in approximately 10^{-7} of the events, which has a negligible effect on the fidelities.

In contrast, heralding on those cases where the output of a single-photon detector indicated that no photons were present can have a significant impact on the gate fidelity if the efficiency η of the detectors is limited. Roughly speaking, this allows photons to escape unnoticed from the system, leaving an incorrect number of photons in the output state. The average fidelity F_D of the destructive controlled-phase gate of Fig. 5.4 and the average fidelity F_{KLM} for the KLM controlled-phase gate are plotted in Fig. 5.7 as a function of the detector efficiency η. Both of these results correspond to a controlled phase shift of $\phi = \pi$ and they assume that the ancilla photons have unit fidelity.

	$\phi = \pi$	$\phi = \pi / 2$
P_D	0.03125	0.0226
P_{KLM}	0.0625	0.0327
P_D'	3.125×10^{-4}	2.26×10^{-4}
P_{KLM}'	6.25×10^{-6}	3.27×10^{-6}

Table 5.1 Comparison of the average probability of success. Here P_D and P_{KLM} are the intrinsic success probabilities of the destructive controlled-phase gate and the KLM gate respectively, while P_D' and P_{KLM}' include the probability of generating the required ancilla photons using heralded down-conversion. The nonlinear phase shift is given by ϕ.

It can be seen that the fidelity of the destructive controlled-phase gate is somewhat less than that of the KLM gate. This can be understood from the fact that the destructive controlled-phase gate of Fig. 5.4 relies upon 3 photon detectors indicating that no photons were detected, while the KLM gate of Fig. 5.3 only depends on 2 null detection events. This includes the fact that each of the nonlinear sign gates of Fig. 5.1 relies on a single null detection event.

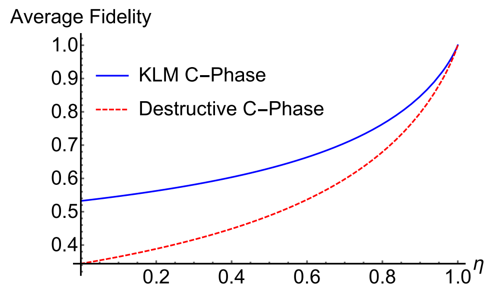

Figure 5.7 Comparison of the fidelities. Average fidelity F_{KLM} of the KLM controlled-phase gate (solid blue line) compared with the average fidelity F_D of a destructive controlled-phase gate (dashed red line). Both fidelities are plotted as a function of the single-photon detector efficiency η.

The KLM gate preserves the control qubit whereas it is destroyed in the controlled-phase gate of Fig. 5.4. As noted previously, a destructive controlled-phase gate can be used in a number of applications, such as nonlocal quantum interference experiments, the generation of entangled Schrödinger cat states [69], and in fusion operations for generating cluster states [107]. More generally, a quantum encoder gate [104,106] could be used in combination with a destructive controlled-phase gate to preserve the value of the control qubit, but that would require an additional ancilla photon. In that case, there would no longer be any advantage in the overall probability of success as compared to using the KLM gate.

5.5 Controlled phase shift for large photon numbers

Up to now, we have assumed that the target state that is input to the controlled-phase gate of Fig. 5.4 contains a maximum of one photon. There are potential applications where it would be desirable to produce a controlled phase shift on a state containing a larger number of photons, such as a coherent state.

This can be useful in producing Schrödinger cat states [99] or in quantum interference experiments, for example [69,86].

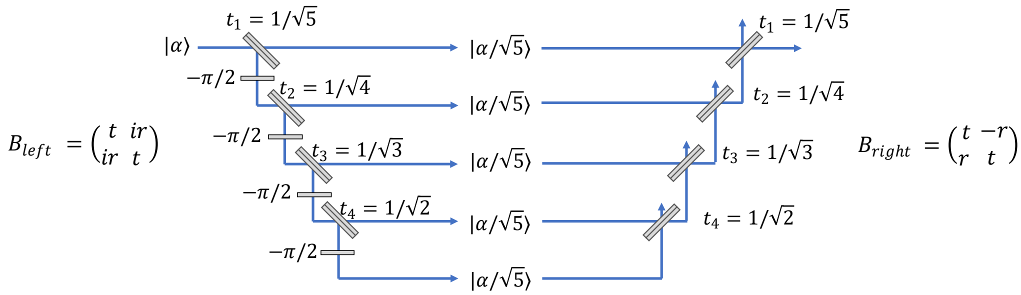

Figure 5.8 Controlled-phase gate for a coherent state. The incident field is divided into N separate paths, each of which contains a destructive controlled-phase gate. The case of $N = 5$ is shown here. A set of beam splitters then recombines the individual beams to form a single output state.

The controlled-phase gate can be modified as shown in Fig. 5.8 to allow a larger number n of photons in the input. Here a series of beam splitters is used to divide the incident field into N different paths. For $N >> n$, each of these paths will contain at most a single photon with high probability, which allows a destructive controlled-phase gate to be applied in each of the paths. The output of each of these controlled-phase gates can then be recombined using another series of beam splitters. This approach is similar to the technique used for noiseless amplifiers when the input state has more than one photon [93].

The main limitation in this approach is that all of the controlled-phase gates have to succeed simultaneously, and the probability of that occurring decreases exponentially with the value of N. In addition, a single control qubit would need to control the phase shift in all N paths. This can be accomplished by using a series of quantum encoders [106], which would further decrease the overall success rate. Nevertheless, an approach of this kind may be feasible for relatively weak coherent states.

5.6 Summary and conclusions

We have proposed a destructive controlled-phase gate that produces a phase shift of ϕ when the control and target qubits both have a logical value of 1. The most commonly used values of ϕ are π or $\pi / 2$, but other phase shifts can be produced as well. The controlled-phase gate proposed here only requires a single nonlinear sign gate as a resource, whereas earlier implementations required two nonlinear sign gates [13]. As a result, the average probability of success for this controlled-sign gate is much larger than in earlier implementations if we include the need to generate ancilla photons using down-conversion and heralding. No such advantage would exist if the ancilla photons are produced on demand using quantum dots, but that typically does not give fidelities as high as can be achieved using down-conversion due to charge fluctuations [120]. Nevertheless, the use of quantum dots to produce single photons is an active area of research with continual improvements [121-123].

The basic idea behind the proposed controlled-phase gate is the use of a dual-rail control qubit to add a photon either before or after the nonlinear sign gate. If the photon is added before the nonlinear sign gate and the target qubit has a logical value of 1, then two photons will pass through the nonlinear sign gate and a phase shift of π will be produced. No such phase shift will be produced if the photon addition is done after the nonlinear sign gate. A photon subtraction is performed at the output of the gate to restore the original number of photons in the target qubit.

The increased probability of success comes at the cost of destroying the control qubit. This is acceptable in a number of applications where the control qubit would have been destroyed in any event, such as in a post-selection process. Potential applications of this kind include the generation of Schrödinger cat states [99], nonlocal interference experiments that violate Bell's inequality [69], and the construction of cluster states using fusion gates [107]. The control qubit can always be preserved if necessary by using a quantum encoder circuit [106] before the controlled-phase gate, but that would require two ancilla photons and there would be no benefit as compared to the original KLM controlled-phase gate. The probability of success vanishes for certain input states for a controlled phase of π, but that is not the case for other values of the controlled phase that are required in many applications.

In summary, the controlled-phase gate described here provides an interesting example of the use of photon addition and subtraction [94], and it may be of practical use in certain applications such as the generation of Schrödinger cat states and violations of Bell's inequality.

Chapter 6 : Noiseless attenuation

This chapter is taken from Ref. [124] that has been published in Physical Review A.

Photon loss in the transmission of continuous-variable quantum states can produce a large amount of decoherence, which limits the usefulness of continuous-variable quantum states in quantum communication systems. These effects can be reduced by noiselessly attenuating the signal prior to transmission, followed by noiseless amplification after transmission [17]. In this chapter, we analyze the degree of coherence of several kinds of continuous-variable quantum states after they have been noiselessly attenuated. We show that ordinary attenuation by a beam splitter would introduce a large amount of decoherence, but that noiseless attenuation preserves the coherence of the quantum states and their ability to produce quantum interference effects.

Noiseless amplification techniques have been studied and experimentally verified, using linear or nonlinear optical elements combined with heralding techniques [125-128]. These probabilistic devices avoid the noise that is always introduced by deterministic, phase-preserving linear amplifiers [15,16]. Similarly, the inverse transformation of noiseless attenuation can be implemented using several kinds of nondeterministic devices [17,59]. The effect of noiseless attenuation can be described by the nonunitary operator $\nu^{\hat{n}}$, where the parameter ν can have values between 0 and 1. This transforms an input state of the form $\sum_n c_n |n\rangle$ into $\varepsilon \sum_n c_n \nu^n |n\rangle$, where ε is a suitable normalization constant. In addition to reducing the average photon number [117], we will show that such a device is truly “noiseless” in the sense that it preserves the coherence of several nonclassical states of interest.

We will analyze the effects of a noiseless attenuator implemented using a beam splitter and conditional measurements (heralding) [1], as illustrated in Fig. 6.1. Noiseless attenuation can also be achieved using an optical parametric amplifier and heralding techniques [59]. Ordinary attenuation by a beam splitter (without heralding) will leave which-path information in the environment, which produces decoherence and a reduction in quantum interference. Heralding on zero photons in the upper output path of Fig. 6.1 eliminates any which-path information in the environment. Several recent experiments have demonstrated the feasibility of heralding on the detection of zero photons [18,129-134].

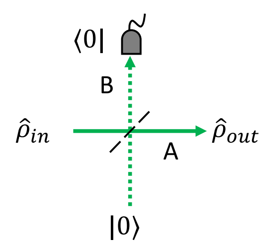

Figure 6.1 A noiseless attenuator implemented using a beam splitter combined with heralding on the presence of zero photons in one of the output ports. The conditional measurement is represented by a projection $\langle 0|$ on the reflected mode.

We will use the Wigner distributions [27] of the states as the primary tool for monitoring their evolution, since negative regions of the Wigner distribution are an indicator of nonclassicality and they can be used to test for any decoherence due to attenuation. In addition, the Wigner distribution is a useful tool since it can be reconstructed using homodyne measurements [135,136].

The rest of the chapter is as follows. In Section 6.1, the nonclassicality of Schrödinger cat states is shown to be preserved under the action of a noiseless attenuator. In Section 6.2, we consider the noiseless attenuation of single mode squeezed vacuum (SMSV) states. Section 6.3 expands the analysis to two-mode states, including the effect of noiseless attenuation on the quantum interference of two SMSV states using a Mach-Zehnder interferometer. Section 6.4 deals with the effects of limited detector efficiency. A Summary and Conclusions are provided in Section 6.5.

6.1 Schrödinger cat states

Schrödinger cat states are a superposition of macroscopically distinguishable states. In the context of quantum optics, they are usually assumed to be a superposition of two coherent states [137]. For a coherent state, the Wigner distribution [27] is a Gaussian distribution centered at the corresponding amplitude. A cat state shows additional oscillations in between the Gaussians of the individual coherent states, as can be seen in Fig. 6.2. These oscillations are due to quantum interference between the two components of the cat state. The interference also gives rise to negative regions of the Wigner distribution, which is an indicator of the nonclassical nature of the state [138].

It is well known that photon loss from a Schrödinger cat state will leave which-path information in the environment, which suppresses the interference pattern in the Wigner distribution [139,140]. If a noiseless attenuator is to be truly "noiseless," it must preserve the oscillations in the Wigner distribution. We will analyze the effects of the noiseless attenuator shown in Fig. 6.1, where the measurement of no photons in one of the output modes heralds the successful generation of the attenuated output in the other path.

We will assume that the input to the noiseless attenuator is an even cat state given by

$$\left|\psi_{cat}\right\rangle = \frac{\left|\alpha\right\rangle + \left|-\alpha\right\rangle}{\sqrt{2\left(1 + e^{-2|\alpha|^2}\right)}}, \tag{6.1}$$

where α is a real parameter and $\left|\alpha\right\rangle$ is a coherent state with that amplitude.

A coherent state is given in the number basis by

$$\left|\alpha\right\rangle = e^{-|\alpha|^2/2} \sum_{n=0}^{\infty} \frac{\alpha^n}{\sqrt{n!}} \left|n\right\rangle, \tag{6.2}$$

and if we consider relatively small amplitude cat states then, to a good approximation, we only need to keep a small number of photon number states $\left|n\right\rangle$. All of the subsequent numerical calculations were performed using an initial value of $\alpha = 2$ and keeping the first 20 photon number terms.

The wave function of the initial cat state in the coordinate representation [69] is thus a superposition of the wave functions $\psi_n(x)$ of the corresponding photon number states

$$\psi_{cat}(x) = \sum_n c_n \psi_n(x), \tag{6.3}$$

where the coefficients c_n can be obtained from Eqs. (6.1) and (6.2) as is described in more detail in the Appendix C. The Wigner distribution for a pure state $|\psi\rangle$ in units where $\hbar = 1$ is then given by the transformation [27]

$$W(x,p) = \frac{1}{2\pi} \int_{-\infty}^{+\infty} dy\; e^{ipy} \psi^*\left(x - \frac{y}{2}\right) \psi\left(x + \frac{y}{2}\right). \tag{6.4}$$

Figure 6.2 shows the Wigner distribution of the input cat state.

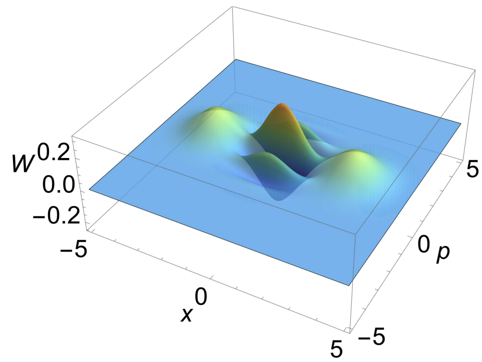

Figure 6.2 Wigner distribution of the input cat state with $\alpha = 2$. The oscillations near the origin are due to quantum interference between the two coherent states in Eq. (6.1). The fact that the Wigner distribution has negative regions indicates that the state is nonclassical. (Dimensionless units.)

The beam splitter transformation used to represent the input photon creation operators in terms of the output operators was chosen to be

$$B = \begin{pmatrix} t & ir \\ ir & t \end{pmatrix}, \tag{6.5}$$

where t and r are the transmissivity and the reflectivity of the beam splitter. Equation (6.5) is equivalent to several commonly used beam splitter transformations with the addition of different phases at its input and output modes.

6.1.1 Ordinary attenuation

The beam splitter shown in Fig. 6.1 can couple photons into the output path labeled A as well as the auxiliary mode labeled B, which can be thought of as the environment. In the photon number basis, the state of the system after the beam splitter can be written as

$$|\psi_{out}\rangle = \sum_{n_a}\sum_{n_b} c(n_a, n_b)|n_a\rangle|n_b\rangle. \tag{6.6}$$

Here the coefficients $c(n_a, n_b)$ can be found using Eqs. (6.1), (6.2), and (6.5), while $|n_a\rangle$ and $|n_b\rangle$ correspond to states with n_a and n_b photons in the two output modes. The details of the calculations are described in the Appendix C.

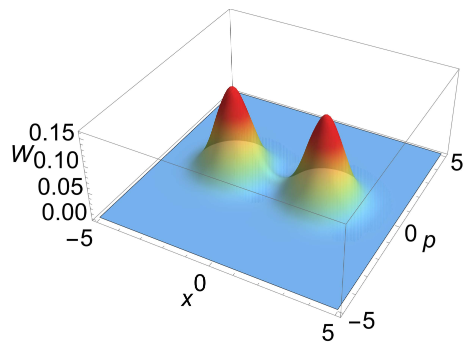

Figure 6.3 Wigner distribution of the output state after a Schrödinger cat state has passed through an ordinary beam splitter. Here, the reflectivity of the beam splitter was arbitrarily chosen to be $r = \sqrt{0.5}$ (a 50:50 beam splitter). The oscillations near the origin have been reduced due to decoherence arising from the which-path information left in the environment. (Dimensionless units.)

Since the number of photons in the environment is not measured in an ordinary attenuator, we need to take a partial trace over the environment. We will denote the projection onto the state with n_b of photons in mode b as $\left|\psi_{out\,|\,n_b}\right\rangle$, which is given by

$$\left|\psi_{out\,|\,n_b}\right\rangle = \sum_{n_a} c(n_a, n_b)\,|n_a\rangle. \tag{6.7}$$

The density matrix of the mixed state after tracing over mode b is given by

$$\hat{\rho}_{out} = \sum_{n_b} \left|\psi_{out\,|\,n_b}\right\rangle \left\langle \psi_{out\,|\,n_b}\right|. \tag{6.8}$$

The trace operation represents the decoherence due to loss of information into the environment. The Wigner distribution of the mixed state after the partial trace is then given by

$$W_{out} = \sum_{n_b} W_{out\ |\ n_b}, \tag{6.9}$$

where $W_{out\ |\ n_b}$ is the Wigner distribution of state $\left|\psi_{out\ |\ n_b}\right\rangle$. Note that $\left|\psi_{out\ |\ n_b}\right\rangle$ is an un-normalized state in our notation.

Figure 6.3 shows the Wigner distribution of the mixed state after tracing over the environment. The peaks corresponding to the original coherent states have been moved closer to the origin due to the overall attenuation. In addition, the oscillations near the origin have been reduced and are not as negative as before attenuation, which indicates a loss of decoherence and less nonclassical behavior.

6.1.2 Noiseless attenuation

In the previous section, we considered the case in which there was no heralding based on the number of photons that were coupled into the auxiliary mode (environment), which reduces the amount of quantum interference. Now we will analyze the output of a noiseless attenuator in which the output is only accepted when no photons are found in the auxiliary mode.

With post-selection of that kind, the Wigner distribution of the output mode is obtained by keeping only the $n_b = 0$ term in Eq. (6.9). After renormalization, this gives

$$W_{out}^{(heralded)} = W_{out\ |\ 0_b} \Big/ \left\langle \psi_{out\ |\ 0_b} \middle| \psi_{out\ |\ 0_b} \right\rangle, \tag{6.10}$$

where

$$\left|\psi_{out\ |\ 0_b}\right\rangle = \sum_{n} c_n t^n \left|n\right\rangle. \tag{6.11}$$

The results are plotted in Fig. 6.4, where it can be seen that the oscillations in the Wigner distribution have been restored. The negativity of the Wigner distribution is also similar to that of the original state in Fig. 6.2. At the same time, the peaks due to the two coherent states have been moved closer to the origin as a result of the attenuation.

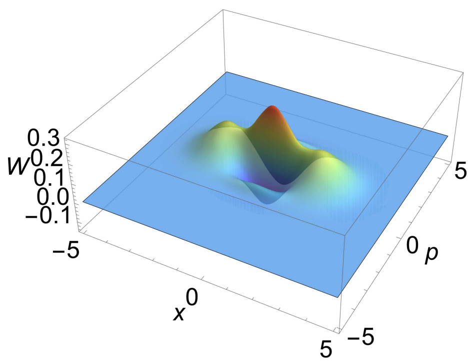

Figure 6.4 Wigner distribution of the state of the output mode after noiseless attenuation of a Schrödinger cat state. Here the output was postselected for events in which no photons were observed in the auxiliary mode. The oscillations near the origin are much larger than is the case for ordinary attenuation in Fig. 6.3, which shows that the coherence of the state has been maintained. (Dimensionless units.)

For comparison, the Wigner distribution of an exact Schrödinger cat state corresponding to a superposition of coherent states with a reduced amplitude of $\alpha = \sqrt{2}$ is plotted in Fig. 6.5. It can be seen that the Wigner distributions in Fig. 6.4 and 6.5 are the same, as can be shown analytically as well. The noiseless attenuation of a cat state is equivalent to simply reducing the amplitude of the coherent states in Eq. (6.1) while maintaining the coherence of their superposition. The amplitude of coherent states in the cat state at the output is given by $t\alpha$.

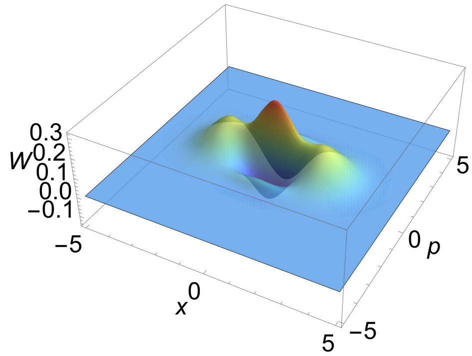

Figure 6.5 Wigner distribution of an exact Schrödinger cat state with a coherent-state amplitude of $\alpha = \sqrt{2}$. Comparing these results with those of Fig. 6.4 shows that noiseless attenuation of a cat state is equivalent to simply reducing the amplitude of the two coherent states in Eq. (6.1). (Dimensionless units.)

The success probability P_S is state dependent and given by

$$P_S = \left\langle \psi_{out \mid 0_b} \middle| \psi_{out \mid 0_b} \right\rangle = \sum_n \left| c_n \right|^2 t^{2n}. \qquad (6.12)$$

If the input state can be approximated by an expansion in the Fock basis with a maximum of N photons, then it is evident from Eq. (6.12) that $P_S \geq t^{2N}$;i.e., it is lower bounded [17]. This is a good approximation for weak cat states and squeezed vacuum states and for some N. For the example shown in Fig. 6.4, $P_S = 0.14$.

6.2 Single mode squeezed vacuum

We saw in the previous section that a noiseless attenuator preserves the coherence of a Schrödinger cat state. We will now consider another example in which a single mode squeezed vacuum (SMSV) state with squeezing along the x quadrature is passed through a noiseless attenuator. The initial SMSV state is given [141] by

$$|\psi_{SMSV}\rangle = \frac{1}{\sqrt{\cosh\xi}}\sum_{n=0}^{\infty}\sqrt{\binom{2n}{n}}\left(-\frac{\tanh\xi}{2}\right)^{n}|2n\rangle, \tag{6.13}$$

where ξ is a parameter related to the strength of the interaction in a $\chi^{(2)}$ medium. States of this kind can be produced using parametric down-conversion [142] and they are widely used in many applications.

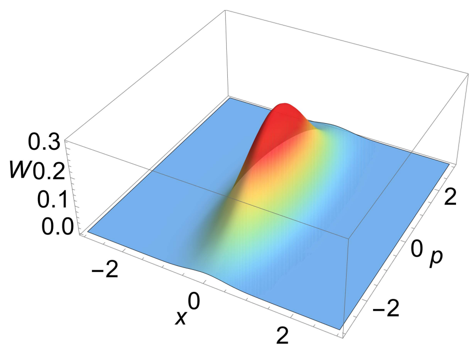

Figure 6.6 Wigner distribution of a single mode squeezed vacuum state with a squeezing parameter of $s = 3$ (arbitrary units). Fitting the distribution with Eq. (6.14) gives $\sigma = 0.707$. (Dimensionless units.)

The Wigner distribution of a single-mode squeezed vacuum state is described by a Gaussian of the form [27]

$$W(x,p) = A\exp\left[-\left(sx^{2}+\frac{p^{2}}{s}\right)\Big/2\sigma^{2}\right], \tag{6.14}$$

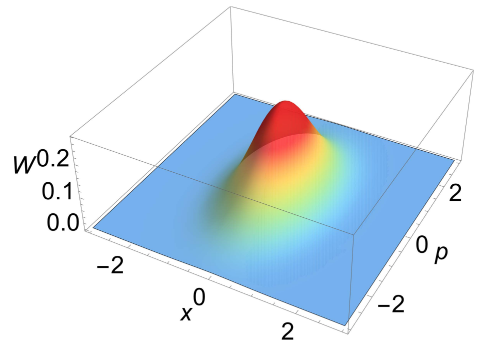

Figure 6.7 Wigner distribution of a single mode vacuum state after it has passed through an ordinary attenuator consisting of a beam splitter with an arbitrarily chosen reflectivity $r = \sqrt{0.5}$. Fitting the distribution with Eq. (6.14) gives $\sigma = 0.759$ and $s = 1.732$. (Dimensionless units.)

as illustrated in Fig. 6.6. The squeezing parameter s is related to ξ by $\xi = \ln\sqrt{s}$, while the width σ has the same value as in an ordinary vacuum state where $s = 1$ and $\sigma = 1/\sqrt{2}$. The uncertainty in one direction of phase space is reduced at the expense of an increased uncertainty in the orthogonal direction, as required by the uncertainty principle.

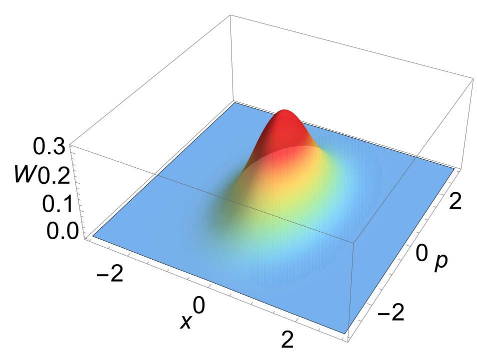

Figure 6.8 Wigner distribution of a single mode squeezed vacuum state after noiseless attenuation using a beam splitter and heralding, as illustrated in Fig. 6.1. Fitting the distribution with Eq. (6.14) gives $\sigma = 0.707$, which is same as that for the original single-mode squeezed state in Fig. 6.6, along with a value of $s = 1.667$. (Dimensionless units.)

Figure 6.7 shows the Wigner distribution of the output state after a single mode squeezed vacuum state has passed through an ordinary attenuator consisting of a 50:50 beam splitter. In comparison, Fig. 6.8 shows the Wigner distribution after the state has passed through a noiseless attenuator with post-selection on the auxiliary mode as discussed earlier. A reduction in the squeezing can be clearly seen in both cases. A fit to Eq. (6.14) gives $\sigma = 0.759$ and $s = 1.732$ for ordinary attenuation, while noiseless attenuation gives $\sigma = 0.707$ and $s = 1.667$. It can be seen that noiseless attenuation gives a state with lower uncertainty (noise) than is obtained using ordinary attenuation, although the difference is not as apparent as it is for a Schrödinger cat state. The new squeezing parameter in the state at the output is given by $\left[s\left(1+t^2\right)+\left(1-t^2\right)\right]\big/\left[s\left(1-t^2\right)+\left(1+t^2\right)\right]$. For the example shown in Fig. 6.7, $P_S = 0.90$.

6.3 Quantum interference

Figure 6.4 shows that noiseless attenuation maintains the quantum interference that is responsible for the oscillations near the origin of the Wigner distribution of a Schrödinger cat state. In this section, we will use a Mach-Zehnder interferometer to give a more explicit demonstration of the effects of a noiseless amplifier. In an ordinary attenuator, which-path information left in the environment will produce a large decrease in the visibility of the interference pattern. A noiseless attenuator eliminates the which-path information and would be expected to maintain the coherence of the quantum interference.

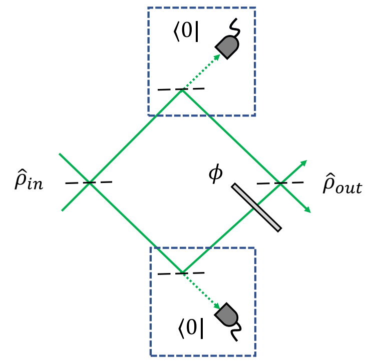

Figure 6.9 A modified Mach-Zehnder interferometer that could be used to measure the amount of quantum interference between two states after noiseless attenuation. The input state is a two-mode squeezed state, which is transformed into two independent single mode squeezed states after passing through the first beam splitter on the left. The noiseless attenuators are shown enclosed in blue dashed boxes. A phase shift ϕ is applied in one path, after which the two modes are recombined at a second beam splitter on the right. The effects of quantum interference can be observed in coincidence measurements between the two output ports.

The interferometer measurements of interest are illustrated in Fig. 6.9. A two-mode squeezed state is incident in the two input ports of the 50:50 beam splitter which is assumed to have the same form as in Eq. (6.5). It can be shown that this transformation generates two independent single-mode squeezed states in the two output modes [143]. These single-mode-squeezed states then pass through the noiseless attenuators placed in both paths, which consist of a beam splitter and heralding on zero photons in one of the output paths as in Fig. 6.1. Finally, the two beams are mixed on a second beam splitter to form a Mach-Zehnder interferometer. Coincidence measurements are performed on the two outputs.

The incident two-mode squeezed state can be written in the number state basis in the form [63]

$$\left|\psi_{TMSV}\right\rangle = \frac{1}{\cosh\xi}\sum_{n=0}^{\infty} -\tanh\xi\;^{n}\left|n\right\rangle\left|n\right\rangle. \tag{6.15}$$

Here ξ is once again related to the strength of the squeezing interaction, which we arbitrarily assumed to have the value $\xi = 0.5$. For relatively small squeezing, it is sufficient to retain only the first few terms in a number-state expansion. Equation (6.15) can be used to calculate the effects of the first beam splitters, and the coincidence rate was calculated numerically using the same techniques as before.

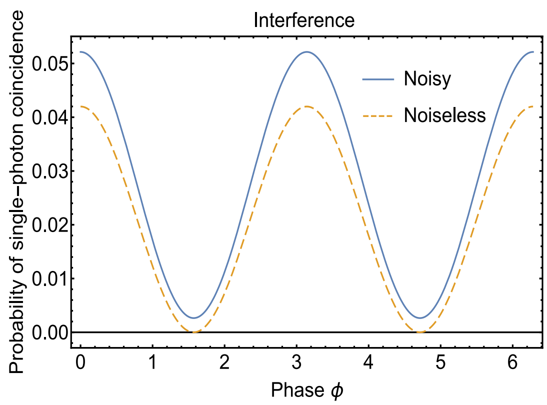

Figure 6.10 Probability of a single-photon coincidence in the two output paths of the Mach-Zehnder interferometer of Fig. 6.9. The solid (blue) line shows the results for the case of ordinary attenuation, where no heralding on the auxiliary mode was performed. This reduces the visibility of the interference pattern to $\sim 90\%$. The dashed (orange) line shows the results for noiseless attenuators, where the output was heralded on the presence of zero photons in the auxiliary mode; this gives a visibility of 100%. Both cases correspond values of $\xi = 0.5$ and $r = \sqrt{0.5}$, chosen arbitrarily. (Dimensionless units.)

With 100% reflective beam splitters (mirrors) in the two paths through the interferometer, Fig. 6.9 reduces to a standard Mach-Zehnder interferometer, and the calculated results show a visibility of 100% in the interference pattern. By reducing the reflectivity of the intermediate beam splitters, ordinary attenuation is introduced in both paths, adding noise. An arbitrarily chosen reflectivity of $r = \sqrt{0.5}$, for both beam splitters, gives a reduced visibility of ~90%. Noiseless attenuation is achieved by heralding on zero photons in the auxiliary modes, as shown in the dashed boxes of Fig. 6.9. This restores the interference visibility to 100%, as illustrated in Fig. 6.10. For the example shown there, $P_S = 0.83$. These results show that noiseless attenuation does maintain the coherence required for quantum interference effects.

6.4 Detector efficiency

Up to this point, the single-photon detectors used in the heralding process were assumed to have 100% detection efficiency. Limited detection efficiency can have a significant effect on the output of the heralded detection process shown in Fig. 6.1, which will no longer be completely "noiseless" [18,19]. In this section, we will model the effects of limited detection efficiency using a perfect detector preceded by a beam splitter to simulate the effects of loss or detection inefficiency.

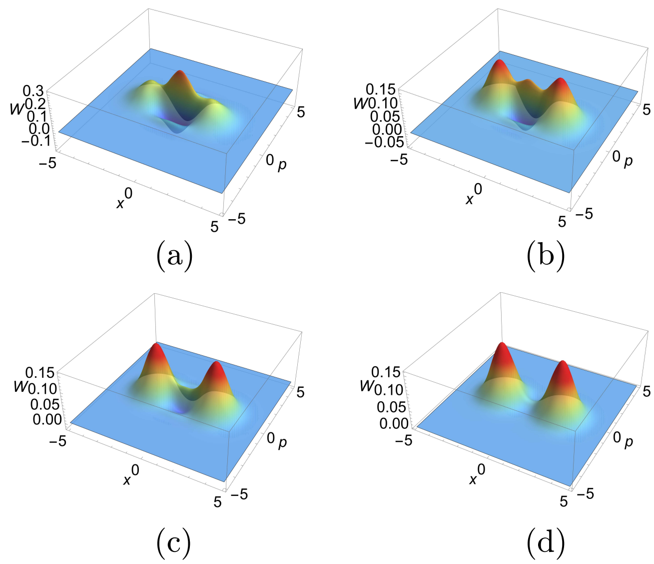

Figure 6.11 Effect of using inefficient detectors for heralding on no photons for noiseless attenuation of cat states. Wigner distribution of the outputs when the efficiency is: (a) 100%, (b) 75%, (c) 50%, and (d) 0%. (Dimensionless units.)

Figure 6.11 shows the effects of a noiseless detector on a Schrödinger cat state for several different values of the detector efficiency. It can be seen that the coherence of the cat state is completely maintained for a perfect detector, but that the performance of the device gradually degrades to that of an ordinary attenuator for a detection efficiency of 0. Intermediate values of the detection efficiency produce a reduction in the oscillations near the origin of the Wigner distribution, indicating a gradual decrease in the coherence of the output state. It can be seen from Fig. 6.11(c) that a detection efficiency as low as 50% can still give significantly better performance than an ordinary attenuator. For an initial cat state, the Wigner function of the output state can be solved analytically for arbitrary detector efficiency (see the Appendix C).

The dependence of the Mach-Zehnder interferometer of Fig. 6.9 on the detection efficiency is shown in Fig. 6.12, which is a plot of the visibility as a function of detector efficiency. There is a decrease in the visibility for lower efficiency photodetectors, which can be understood from the fact that a detector with limited efficiency does not completely rule out the possibility of which-path information being left in the environment, as in ordinary attenuation.

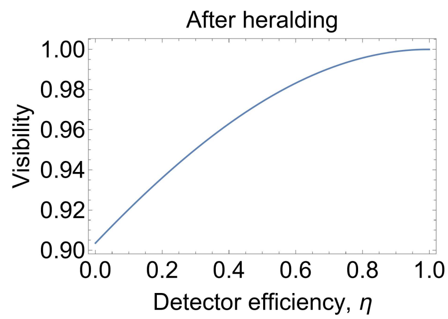

Figure 6.12 Visibility of the quantum interference from the Mach-Zehnder interferometer of Fig. 6.9 as a function of the detector efficiency used in the heralding process. No which-path information is left in the environment and the visibility is 100% for a perfect detector. The visibility decreases for limited detection efficiency since the possibility of which-path information is not completely eliminated in that case. (Dimensionless units).

The overall process is still noisy, and we are simply heralding on a suitable subset of the output states, which eliminates the terms that would have contributed to the noise. The ability to eliminate these outcomes, however, depends on the detector efficiency, which in turn has an effect on the amount of which-path information lost to the environment.

6.5 Summary and conclusions

Ordinary attenuation of an optical quantum state using a beam splitter can produce decoherence due to which-path information left in the environment.

Noiseless attenuation can be achieved using a beam splitter combined with heralding on those events in which no photons are present in the auxiliary mode (the environment), which eliminates the which-path information. It is interesting that this process can reduce the intensity of an optical signal without extracting any power from the system [17,59].

In this chapter, we showed that noiseless attenuators are truly “noiseless” in the sense that they do not reduce the coherence of the input state. We first considered the case of a Schrödinger cat state that has passed through a noiseless attenuator. The Wigner distribution of a cat state has characteristic oscillations near the origin that arise from the interference of its two constituent coherent states. The Wigner distribution also has negative regions, which demonstrates that the states are nonclassical. We showed that noiseless attenuation maintains both these properties. We also found similar results for the case of a single-mode squeezed vacuum state, where noiseless attenuation maintained the width of the Gaussian Wigner distribution.

Quantum interference effects were investigated more directly by considering a Mach-Zehnder interferometer with noiseless attenuators in each arm and a two mode-squeezed vacuum state for the input. The visibility in the interference pattern from coincidence measurements was found to be maintained by noiseless attenuation, while it was substantially reduced by ordinary attenuation. Once again, this is due to the fact that the heralding process eliminates any which-path information left in the environment.

The effects of limited detection efficiency were also investigated. As might be expected, heralding using a detector with limited detection efficiency limits the ability of the heralding process to eliminate noise by eliminating those states that would leave which-path information in the environment.

These results may be of practical use in quantum communications systems based on continuous variables, where photon loss will result in the decoherence of nonclassical states. These effects can be reduced by noiselessly attenuating the signal before transmission, followed by noiseless amplification after transmission [17]. Our results show that noiseless attenuation can maintain the coherence of nonclassical states, but that detector efficiency will be an important consideration.

Chapter 7 : Inhibiting phase drift in multi-atom clocks using the quantum Zeno effect

This chapter is taken from the preprint Ref. [144] submitted to Scientific Reports.

Atomic clocks have a number of important applications[145-149], and there has been considerable progress in developing new techniques to improve their performance[150-153]. The precision of atomic clocks depends in part on the absorption bandwidth of the relevant atomic transition[154]. Here we consider an ensemble of N atoms whose transition frequencies have been independently perturbed by a small amount due to coupling to the environment or other factors, such as the effective bandwidth due to finite lifetimes. We investigate the possibility of using the quantum Zeno effect to lock the relative phases of the atoms, which would decrease their effective bandwidth by a factor of $1/\sqrt{N}$. An example is analyzed in which the quantum Zeno effect can be used to lock the relative phase of a pair of atoms, after which the elapsed time can be determined. Practical applications may require $N >> 1$ in order to achieve a good signal-to-noise ratio.

In the quantum Zeno effect[21,37,155], frequent measurements can inhibit transitions into unwanted states and force the system to evolve in the desired subspace of Hilbert space. The Zeno effect has been experimentally demonstrated using $^{9}Be^{+}$ ground-state hyperfine levels[35], Bose-Einstein condensates[156], ion traps[157], nuclear magnetic resonance[158], cold atoms[159], cavity QED[160], and large atomic systems[155]. It has also been shown that the Zeno effect is a sufficient resource for the implementation of quantum logic gates[22,161], which could be used as the basis of a quantum computer[161] or quantum repeaters[162]. The Zeno effect can also be used to prepare various nonclassical or entangled states[68,163-166] and to protect entanglement once it has been generated[167,168]. The anti-Zeno effect, by which repeated measurements increase the rate of transitions, may be useful in quantum heat engines[169].

Earlier approaches have used entangled states to synchronize distant clocks[170,171]. Our approach is also based on the use of simple entangled states (dark states)[172], but here the goal is to improve the stability of a single clock rather than synchronize two or more distant clocks. A Zeno-like-effect has recently been shown to mitigate phase diffusion in self-sustaining quantum systems[173-175], which is somewhat related to our technique for inhibiting relative phase drift in atomic clocks. It has also been shown that an atomic clock can be implemented using the entropy reduction produced by weak coupling to the environment and continuous measurements[176].

This chapter begins with a discussion of the potential reduction in the bandwidth of an ensemble of atoms using the quantum Zeno effect and the increased precision of an atomic clock that could be achieved in that way in Section 7.1. In Section 7.2, a technique for using the quantum Zeno effect to lock the relative phase of a pair of two-level atoms is then described. Section 7.3 discusses the advantages of using three-level or four-level atoms. The ability to directly read out the phase of the atoms after some period of time and the need to extend these methods to larger numbers of atoms is considered in Section 7.4. Section 7.5 provides a summary and conclusions.

7.1 Benefit of atomic phase locking

Atomic clocks are typically operated by locking the frequency of an external microwave oscillator to the resonant frequency associated with an atomic transition between two nuclear hyperfine states[20]. Once locked in this way, the external oscillator provides the readout of the clock. The precision of such a clock depends on the bandwidth of the atoms and the measurement interval as described by the Allan deviation[154,177], which is given by

$$\sigma_y(\tau) \approx \frac{\Delta f}{f\sqrt{N}}\sqrt{\frac{T_c}{\tau}}. \tag{7.1}$$

where $\sigma_y(\tau)$ is the standard deviation of the fractional frequency offset $y(t)$ in the output, which is defined by

$$y(t) = \frac{f(t) - f_0}{f_0}, \tag{7.2}$$

T_c is the clock cycle time, τ the total averaging time, and N is the number of independent atoms.

Equation (7.1) is valid when the statistical noise is much larger than any systematic error. It is based on the assumption that the k^{th} atom in the ensemble has a frequency f_k chosen at random from a normal distribution about a central frequency f_0, with a full width at half maximum (FWHM) of Δf. This corresponds to a standard deviation of $\sigma \equiv \Delta f / 2\sqrt{2\ln 2}$. The $\sqrt{N}$ term in the denominator of Eq. (7.1) corresponds to the fact that the signal-to-noise ratio increases for larger numbers of atoms, since the absorption signal is larger in that case. Equation (7.1) clearly shows the advantage of reducing the atomic bandwidth Δf.

Locking an external oscillator to the atomic transitions is roughly equivalent to measuring the spectrum of the atomic transitions and performing a least-square fit to determine the central frequency f_0, as illustrated in Fig. 7.1(a). For a fixed number of atoms, the peak in the spectrum will be inversely proportional to the bandwidth Δf, as illustrated in Fig. 7.1(b), since the total rate of transitions is fixed. The goal of our approach is to use the quantum Zeno effect to lock the relative phases of all of the atoms, despite the differences between the various values of f_k.

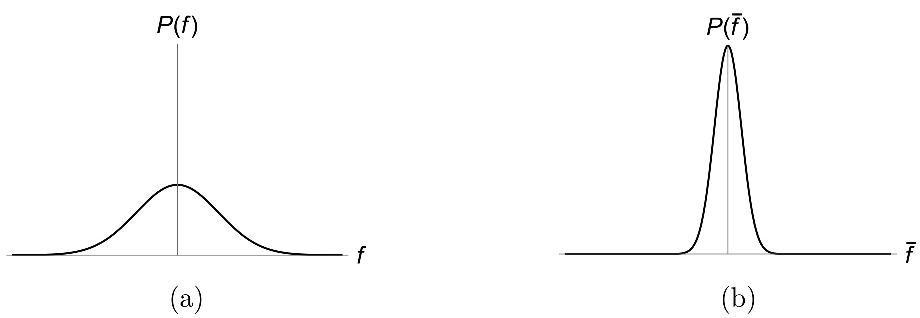

Figure 7.1 Reduced bandwidth after phase locking. (a) Initial probability distribution $P(f)$ of the frequencies f_k of N atoms in an atomic clock. (b) If the frequencies of all of the atoms are locked to their average frequency $\overline{f}$ using the quantum Zeno effect, the width of the probability distribution will be reduced by a factor of $1/\sqrt{N}$ and the height of the peak will be increased accordingly. In this example $N = 9$.

After phase locking, the central peak in Fig. 7.1(b) will correspond to the average $\overline{f}$ of all of the frequencies of the individual atoms, as given by

$$\overline{f} = \frac{1}{N}\sum_{k=1}^{N} f_k. \tag{7.3}$$

This results in a standard deviation $\bar{\sigma}$ for $\bar{f}$ that is reduced by a factor of $1/\sqrt{N}$, as is the FWHM $\Delta\bar{f}$, when measured over an ensemble of similarly-prepared systems. The Allan deviation of Eq. (7.1) is reduced by the corresponding amount. It should be noted that reducing the bandwidth is in addition to the factor of $1/\sqrt{N}$ that already appears in Eq. (7.1), which corresponds to the improved signal-to-noise ratio due to the increased transition rate from N atoms.

The output of an atomic clock could also be read out by directly measuring the average change in phase of the atoms after they have evolved over a time interval of Δt. The fact that the atoms have slightly different frequencies will cause a measurement of the average phase to wash out over a period of time. In order to see this, consider a situation in which all of the atoms start out at time $t = 0$ with the same phase. At a subsequent time t, the phases of all of the atoms will have evolved independently based on their frequencies f_k as chosen from a normal distribution given by

$$P(f) = \frac{1}{\sqrt{2\pi\sigma^2}} e^{-(f-f_0)^2/2\sigma^2}. \tag{7.4}$$

A measurement of the average cosine of the phases will then have the value

$$\cos\phi_{meas.} = \frac{1}{N}\sum_{k=1}^{N}\cos(2\pi f_k t). \tag{7.5}$$

The expectation value of this signal measured over a large number of similarly-prepared samples is given by

$$\langle\cos\phi_{meas.}\rangle = \int df\, P(f)\frac{1}{N}\sum_{k=1}^{N}\cos(2\pi f t), \tag{7.6}$$

which reduces to

$$\langle\cos\phi_{meas.}\rangle = \int_{-\infty}^{\infty} df\, P(f)\cos(2\pi f t) = e^{-\frac{1}{2}(2\pi t)^2\sigma^2}\cos(2\pi f_0 t). \tag{7.7}$$

The exponential factor in equation Eq. (7.7) means that a measurement of the average phase will wash out after a relatively short amount of time, as indicated in Fig. 7.2(a).

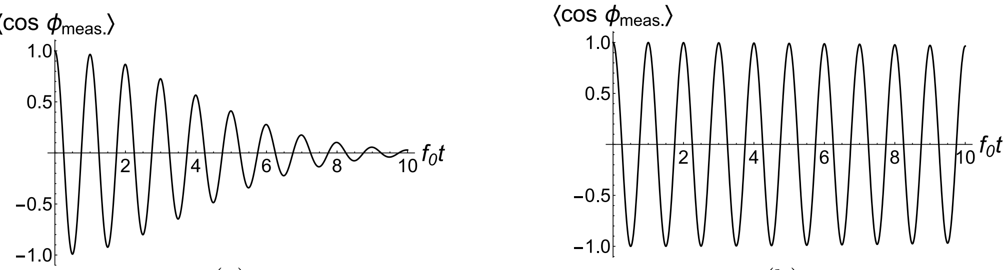

(a) (b)

Figure 7.2 Average phase of an ensemble of atoms. The expectation value of the average of the cosine of the phases of an ensemble of atoms is plotted as a function of the time t. (a) The average cosine of the phase for an ensemble of independent atoms. (b) The cosine of the phase averaged over an ensemble where the phases of the atoms have all been locked to their average phase $\overline{f}$ using the quantum Zeno effect. For simplicity, the results plotted correspond to $\Delta f / f_0 = 10\%$ and a central frequency of $f_0 = 100 Hz$. It can be seen that the average phase decoheres very rapidly for independent atoms, while locking the phase using the quantum Zeno effect can greatly extend the time interval over which the average phase is coherent and could be measured.

On the other hand, suppose that all of the atoms have been locked onto their average frequency $\overline{f}$ given by Eq. (7.3) as a result of the Zeno effect or some other mechanism. $\overline{f}$ is once again a random variable, but with a reduced standard deviation of $\sigma / \sqrt{N}$. Now the cosine of the average phase is simply

$$\cos \phi_{meas.} = \cos\left(2\pi \overline{f}\, t\right), \tag{7.8}$$

which has an expectation value of

$$\langle \cos\phi_{meas.} \rangle = e^{-\frac{1}{2}(2\pi t)^2 \sigma^2 / N} \cos(2\pi f_0 t). \tag{7.9}$$

In this case the average phase remains coherent over a much longer time interval, as illustrated in Fig. 7.2(b). These plots correspond to an arbitrary choice of $N = 100$ atoms with $\Delta f / f_0 = 10\%$.

Figure 7.2 provides another way to understand the potential benefits of locking the phases of the atoms in an atomic clock. The rest of our analysis will be based on determining the elapsed time by measuring the change in phase using the radiation emitted by the atoms, as will be described below.

7.2 Two-level atoms

In this section, we will show that the quantum Zeno effect can be used to lock the relative phase of a pair of two-level atoms. It will be assumed that the two-level atoms interact weakly with a single mode of an optical cavity and that their average frequency $\bar{f}$ is on resonance with the cavity mode, as illustrated in Fig. 7.3.

The atoms are initially prepared in a subradiant state $|\psi\rangle$ given by

$$|\psi\rangle = \frac{|EG\rangle - |GE\rangle}{\sqrt{2}} \otimes |0\rangle_{field}, \tag{7.10}$$

where the state $|EG\rangle$ corresponds to one atom in its excited state and the other atom in its ground state, with a similar notation for the other states of the atoms. The state $|0\rangle_{field}$ represents the vacuum state of the cavity.

The Hamiltonian for this system in the rotating wave approximation can be written [178] as

$$
\begin{aligned}
\hat{H} &= \hbar\omega\left(\hat{n} + 1/2\right) + \hbar\omega_A \left|E\right\rangle_A \left\langle E\right| + \hbar\omega_B \left|E\right\rangle_B \left\langle E\right| \\
&+\hbar\frac{\Omega_A}{2}\left[\hat{\sigma}_A^{(+)}\hat{a} + \hat{\sigma}_A^{(-)}\hat{a}^\dagger\right] + \hbar\frac{\Omega_B}{2}\left[\hat{\sigma}_B^{(+)}\hat{a} + \hat{\sigma}_B^{(+)}\hat{a}^\dagger\right],
\end{aligned} \tag{7.11}
$$

where ω is the angular frequency of the cavity mode while ω_A and ω_B are the transition frequencies of the two atoms A and B, which are unequal due to an interaction with the environment. $\Omega_{A(B)}$ are the interaction strengths between the atoms and the photons, and $\hat{\sigma}_{A(B)}^{(\pm)}$ are the atomic raising and lowering operators. In the subsequent analyses, we will assume that the interaction strengths of the two atoms are identical. A pair of atoms in a subradiant state of this kind cannot emit a photon into the cavity mode due to destructive interference between the two probability amplitudes[172,179].

We will now consider the evolution of the initial state of Eq. (7.10) over a time interval τ that is sufficiently short that the effects of the interaction with the cavity modes can be neglected $\left(\Omega_{A(B)} = 0\right)$. If the atoms both had the same transition frequency, then the phases of their excited states would evolve at the same rate and the form of the subradiant state would be maintained indefinitely (the minus sign would always hold).

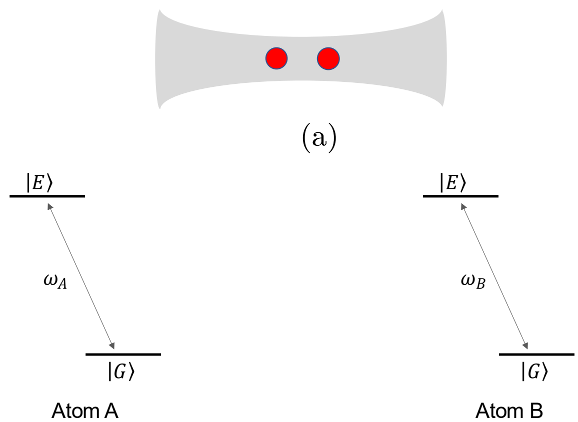

(b)

Figure 7.3 A pair of two-level atoms in a cavity. (a) A pair of two-level atoms interact weakly with a single mode of an optical cavity. The quantum Zeno effect can be implemented by periodically introducing n photons into the cavity and then measuring the number of photons present after a time interval of τ_m. Alternatively, the atoms could be passed through a cavity containing n photons. (b) Typical energy level diagrams for the two atoms.

Suppose instead that the frequencies of the two atoms are given by $\omega_A = \omega + \delta + \Delta$ and $\omega_B = \omega + \delta - \Delta$. Here δ is a common deviation from the resonant frequency of the cavity while 2Δ corresponds to a frequency difference between the two atoms due to environmental effects. To first order in τ, the final state of the system is given by

$$|\psi'\rangle = \left\{[1 - i(\omega+\delta)\tau]\left[\frac{|EG\rangle - |GE\rangle}{\sqrt{2}} - i\tau\Delta\frac{|EG\rangle + |GE\rangle}{\sqrt{2}}\right]\right\} \otimes |0\rangle_{field}\,. \tag{7.12}$$

The second term in this equation corresponds to a superradiant state where the rate of photon emission is enhanced by quantum interference effects instead of decreased. It can be seen that any difference in transition frequencies will cause the atoms to gradually develop a superradiant component. The overall phase shift of $-i(\omega+\delta)\tau$ has no physical effects and can be ignored.

The basic idea of our approach is to make frequent measurements to determine whether or not the system has evolved into the superradiant state. If it has not, then the system will collapse back into a pure subradiant state with the original relative phase of 180° as in Eq. (7.10). If these measurements are made frequently enough (or continuously), the transition into the superradiant state will be inhibited by the Zeno effect and the relative phase of the two atoms will remain unchanged, with both atoms evolving at the average angular frequency $\bar{\omega} = 2\pi\bar{f}$.

The measurements required for the quantum Zeno effect could be made in several ways. Here we will consider an approach in which the coupling of the atoms to the cavity mode is sufficiently weak that any interaction with the vacuum state (the vacuum Rabi effect) can be neglected. A large interaction with the field can then be produced by temporarily introducing a large number n of photons into the cavity, so that $|0\rangle_{field} \rightarrow |n\rangle_{field}$. Alternatively, the atoms could be passed through a small aperture in a cavity that already contains n photons[180,181]. Either way, the coupling to the cavity field can be turned on or off as desired.

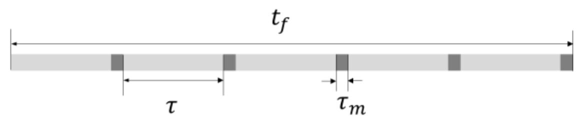

Figure 7.4 Relevant time scales in the measurement process. τ denotes the time interval between the measurements, during which the system will have evolved a small probability amplitude to be in the superradiant state. A strong interaction between the atoms and n photons in the cavity is applied during the measurement time τ_m, which is chosen to be half a Rabi flop for the superradiant state in Eq. (7.12). t_f is the final time at which the output of the clock is read out. We consider the limit of $\tau_m << \tau << t_f$, where the quantum Zeno effect would be expected to inhibit the growth of the superradiant state and lock the relative phases of the atoms.

The interaction with the field initially containing n photons is maintained for a measurement time τ_m as illustrated in Fig. 7.4. τ_m is chosen in such a way that the superradiant term in Eq. (7.12) will undergo half a Rabi flop, causing it to absorb or emit one photon [178]. The subradiant term is unaffected by the presence of the photons in the cavity. The initial number of photons n is chosen to be sufficiently large that τ_m is much shorter than the time required for a significant superradiant amplitude to evolve. This process is repeated until the final time t_f when the output of the clock is read out, as described below. As illustrated in Fig. 7.4, we assume a measurement sequence in which $\tau_m << \tau << t_f$.

In that limit, we would expect the quantum Zeno effect to inhibit the growth of the superradiant state. Integrating Schrödinger's equation over a time interval of τ_m using the initial state of Eq. (7.12) gives a final state of the form

$$\begin{aligned}
|\psi''\rangle &= \frac{|EG\rangle - |GE\rangle}{\sqrt{2}} \otimes |n\rangle_{field} \\
&-i\tau\Delta\cos\left(\Omega\tau_m\sqrt{n+\frac{1}{2}}\right)\frac{|EG\rangle + |GE\rangle}{\sqrt{2}} \otimes |n\rangle_{field} \\
&-\frac{\tau\Delta}{\sqrt{2n+1}}\sin\left(\Omega\tau_m\sqrt{n+\frac{1}{2}}\right)\left[\sqrt{n+1}\,|GG\rangle \otimes |n+1\rangle_{field} + \sqrt{n}\,|EE\rangle \otimes |n-1\rangle_{field}\right].
\end{aligned} \tag{7.13}$$

The second term with the cosine dependence will vanish for half a Rabi flop, while the third term with the sine dependence will reach a maximum. For simplicity, the overall phase factor from Eq. (7.12) has been omitted.

It can be seen that the net effect of this measurement process is to change the number of photons by ± 1 if the atoms were in the superradiant state. In principle, the number of atoms could be measured at the end of the time interval τ_m in order to determine whether or not the superradiant state was present. As a practical matter, no actual measurements are required in the quantum Zeno effect, since the entanglement with the state of the field is sufficient to inhibit the growth of the superradiant state.

The probability P_E that the system will be found to be in an error state corresponding to one of the last two terms in Eq. (7.13) is given by

$$P_E = \Delta^2 \tau^2. \tag{7.14}$$

The probability P_S of success that the system will remain in the subradiant state at the final time t_f is then given by

$$P_S = (1 - P_E)^{t_f/(\tau+\tau_m)} \approx \exp[-\Delta^2(\tau + \tau_m)t_f]. \tag{7.15}$$

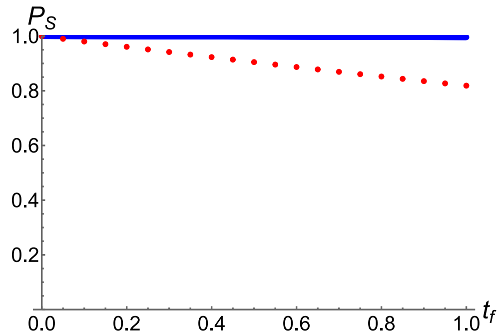

Figure 7.5 Plot of the probability P_S that the phase of a pair of two-level atoms will remain locked as a function of time. The solid line corresponds to relatively frequent measurements with $(\tau + \tau_m) = 0.001$, while the dotted line corresponds to less frequent measurements with $(\tau + \tau_m) = 0.05$. It can be seen that the quantum Zeno effect can lock the relative phase of a pair of two-level atoms in the limit of frequent measurements.

P_S is plotted as a function of time in Fig. 7.5 for two different values of τ. With frequent measurements corresponding to $(\tau + \tau_m) = 0.001$, it can be seen that the Zeno effect is very effective in keeping the pair of atoms in the subradiant state with their phases locked to their mean phase. Less frequent measurements corresponding to $(\tau + \tau_m) = 0.05$ are less successful in locking the phase. These results correspond to an arbitrarily chosen value of $\Delta = 2$.

7.3 Three-level and four-level atoms

In the previous section, we showed that the quantum Zeno effect could be used to lock the relative phase of a pair of two-level atoms. In the limit of frequent measurements, the final state is identical to the initial state aside from an overall phase factor that cannot be measured. As a result, there is no way to read the output of the clock by measuring a time-dependent phase factor. In order to solve this problem, we need a reference state of some kind so that a measurement of the relative phase can be used to estimate the elapsed time as indicated by the clock.

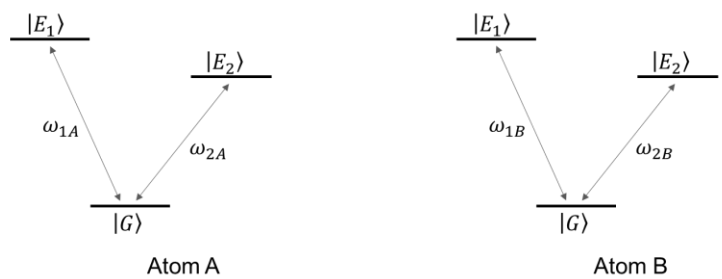

Figure 7.6 A pair of three-level atoms in a V-configuration. A pair of three-level atoms are in a state that corresponds to a superposition of two separate subradiant states, as described in Eq. (7.16). This allows the elapsed time to be measured by determining the relative phase of states $|E_1\rangle$ and $|E_2\rangle$.

With this in mind, we consider two three-level atoms in a V-configuration as shown in Fig. 7.6. The atoms are assumed to be in an initial state given by

$$|\psi\rangle = \left[\left(|E_1G\rangle - |GE_1\rangle\right) + \left(|E_2G\rangle - |GE_2\rangle\right)\right]/2. \qquad (7.16)$$

Here $|E_1\rangle$ and $|E_2\rangle$ are excited states of the atoms with energies $E_1 \neq E_2$. This state corresponds to a superposition of two subradiant states, and the basic idea is to lock the relative phase of each of the individual terms using the Zeno effect, after which the relative phase between the first and second terms can be used as a readout of the elapsed time.

The Hamiltonian for this system is given by

$$\begin{aligned}
\hat{H} &= \hbar\omega_1\left(\hat{n}_1 + 1/2\right) + \hbar\omega_2\left(\hat{n}_2 + 1/2\right) \\
&+\hbar\omega_{1A}\left|E_1\right\rangle_A\left\langle E_1\right| + \hbar\omega_{2A}\left|E_2\right\rangle_A\left\langle E_2\right| + \hbar\omega_{1B}\left|E_1\right\rangle_B\left\langle E_1\right| + \hbar\omega_{2B}\left|E_2\right\rangle_B\left\langle E_2\right| \\
&+\hbar\frac{\Omega}{2}\left[\hat{\sigma}_{1A}^{(+)}\hat{a}_1 + \hat{\sigma}_{1A}^{(-)}\hat{a}_1^\dagger\right] + \hbar\frac{\Omega}{2}\left[\hat{\sigma}_{2A}^{(+)}\hat{a}_2 + \hat{\sigma}_{2A}^{(-)}\hat{a}_2^\dagger\right] \\
&+\hbar\frac{\Omega}{2}\left[\hat{\sigma}_{1B}^{(+)}\hat{a}_1 + \hat{\sigma}_{1B}^{(-)}\hat{a}_1^\dagger\right] + \hbar\frac{\Omega}{2}\left[\hat{\sigma}_{2B}^{(+)}\hat{a}_2 + \hat{\sigma}_{2B}^{(-)}\hat{a}_2^\dagger\right],
\end{aligned} \tag{7.17}$$

where ω_1 and ω_2, refer to two cavity modes that are in resonance with the atomic transitions $\left|E_1\right\rangle \leftrightarrow \left|G\right\rangle$ and $\left|E_2\right\rangle \leftrightarrow \left|G\right\rangle$, respectively. If the energies of the two atoms are slightly different due to environmental effects, the subradiant states in Eq. (7.16) will gradually evolve into superradiant components as in the previous section. The Zeno effect can be used to inhibit the superradiant components as before, where n photons are now introduced into both modes of the cavity.

Unfortunately, it is possible to absorb a photon from the field in a transition such as $\left|E_1G\right\rangle\left|n\right\rangle_1\left|n\right\rangle_2 \leftrightarrow \left|E_1E_2\right\rangle\left|n\right\rangle_1\left|n-1\right\rangle_2$ or $\left|GE_1\right\rangle\left|n\right\rangle_1\left|n\right\rangle_2 \leftrightarrow \left|E_2E_1\right\rangle\left|n-1\right\rangle_1\left|n\right\rangle_2$ even in the subradiant states of Fig. 7.6. This difficulty occurs because both of the excited energy levels interact with a common lower level (the ground state). This problem can be avoided using a pair of four-level atoms as illustrated in Fig. 7.7, where the excited states $\left|E_1\right\rangle$ and $\left|E_2\right\rangle$ interact with two separate lower-energy states $\left|G_1\right\rangle$ and $\left|G_2\right\rangle$. These could correspond to two different hyperfine levels of the atomic ground state, for example. The cross-couplings between $\left|E_1\right\rangle$ and $\left|G_2\right\rangle$ are assumed to be negligibly small, as is the coupling between $\left|E_2\right\rangle$ and $\left|G_1\right\rangle$.

The four-level system is prepared in an initial state given by

$$\left|\psi\right\rangle = \frac{1}{2}\left[\left(\left|E_1G_1\right\rangle - \left|G_1E_1\right\rangle\right) + \left(\left|E_2G_2\right\rangle - \left|G_2E_2\right\rangle\right)\right]\left|0\right\rangle_1\left|0\right\rangle_2, \tag{7.18}$$

with a Hamiltonian given by

$$
\begin{aligned}
&\hat{H} = \hbar\omega_1\left(\hat{n}_1 + 1/2\right) + \hbar\omega_2\left(\hat{n}_2 + 1/2\right) \\
&+\hbar\omega_{E1A}\left|E_1\right\rangle_A\left\langle E_1\right| + \hbar\omega_{E2A}\left|E_2\right\rangle_A\left\langle E_2\right| + \hbar\omega_{G1A}\left|G_1\right\rangle_A\left\langle G_1\right| + \hbar\omega_{G2A}\left|G_2\right\rangle_A\left\langle G_2\right| \\
&+\hbar\omega_{E1B}\left|E_1\right\rangle_B\left\langle E_1\right| + \hbar\omega_{E2B}\left|E_2\right\rangle_B\left\langle E_2\right| + \hbar\omega_{G1B}\left|G_1\right\rangle_B\left\langle G_1\right| + \hbar\omega_{G2B}\left|G_2\right\rangle_B\left\langle G_2\right| \\
&+\hbar\frac{\Omega}{2}\left[\hat{\sigma}_{1A}^{(+)}\hat{a}_1 + \hat{\sigma}_{1A}^{(-)}\hat{a}_1^\dagger\right] + \hbar\frac{\Omega}{2}\left[\hat{\sigma}_{2A}^{(+)}\hat{a}_2 + \hat{\sigma}_{2A}^{(-)}\hat{a}_2^\dagger\right] \\
&+\hbar\frac{\Omega}{2}\left[\hat{\sigma}_{1B}^{(+)}\hat{a}_1 + \hat{\sigma}_{1B}^{(-)}\hat{a}_1^\dagger\right] + \hbar\frac{\Omega}{2}\left[\hat{\sigma}_{2B}^{(+)}\hat{a}_2 + \hat{\sigma}_{2B}^{(-)}\hat{a}_2^\dagger\right].
\end{aligned}
\tag{7.19}
$$

Quantum Zeno measurements can be implemented as before by introducing n photons in each of the two cavity modes that are resonant on the transitions in Fig. 7.7. The photons interact with the atoms for a short time interval $\tau_m << \tau$, after which the number of photons in each mode could be measured. (Once again, no actual measurements are required for the Zeno effect.)

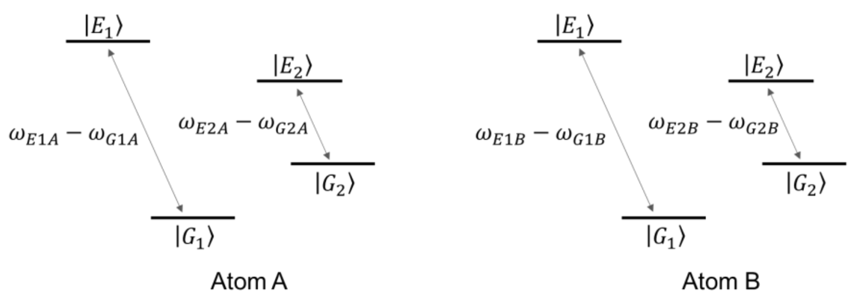

Figure 7.7 A four-level atomic system used to avoid transitions from the ground state. Atomic states $\left|E_1\right\rangle$ and $\left|G_1\right\rangle$ are coupled by allowed transitions, as are $\left|E_2\right\rangle$ and $\left|G_2\right\rangle$, with negligible coupling between the other states. The quantum Zeno effect is used to lock the relative phase of each pair of states, after which the relative phase between $\left|E_1\right\rangle$ and $\left|E_2\right\rangle$ can be used to read out the elapsed time from the clock.

The probability P_E that the four-level system will be found to be in an error state corresponding to one of the superradiant states after a time interval of τ can be shown to be

$$P_E = \left(\frac{\Delta_1^2 + \Delta_2^2}{2} \right) \tau^2. \tag{7.20}$$

Here $\Delta_k \equiv \left[(E_{kA} - G_{kA}) - (E_{kB} - G_{kB}) \right] / 2$, which corresponds to the difference in the transition energies of the two atoms. The probability P_S that the system will remain in the subradiant state at the final time t_f is then given by

$$P_S = (1 - P_E)^{t_f/(\tau+\tau_m)} \approx \exp\left[-\left(\frac{\Delta_1^2 + \Delta_2^2}{2} \right) (\tau + \tau_m) t_f \right]. \tag{7.21}$$

It can be seen that the Zeno effect can inhibit the growth of the superradiant states and maintain a fixed relative phase within each of the states $|E_k\rangle$ and $|G_k\rangle$ as before. The probability of success drops off at the same rates as shown in Fig. 7.5 if we choose Δ_1 and Δ_2 equal to the parameter Δ in Eq. (7.15). Once again, the probability of success can be made arbitrarily high by reducing the value of τ.

7.4 Clock readout

In our approach, the elapsed time can be read out by measuring the relative phase of the two terms in parentheses in Eq. (7.18) at the final time. For large values of t_f, multiple oscillations may have occurred, but the output can be used to give a small correction to an external oscillator, for example.

As shown in the previous section, the quantum Zeno effect can be used to eliminate the growth of the superradiant state. In that case, the initial state of Eq. (7.18) evolves into

$$\left|\psi\right\rangle = \frac{1}{2}\left[\left(\left|E_1G_1\right\rangle - \left|G_1E_1\right\rangle\right) + e^{i\omega_{clock}t_f}\left(\left|E_2G_2\right\rangle - \left|G_2E_2\right\rangle\right)\right] \tag{7.22}$$

at the final time t_f. Here $\omega_{clock} = \left(\bar{E}_1 + \bar{G}_1 - \bar{E}_2 - \bar{G}_2\right)/\hbar$, which reflects the phase precession due to the difference in the energy levels. $\bar{E}_k$ and $\bar{G}_k$ are the values of E_k and G_k averaged over the two atoms.

There are several ways to measure the relative phase of these two states. We will consider an approach in which Eq. (7.22) is first converted to a superposition of superradiant states, after which the phase of the electromagnetic field emitted by the atoms can be measured. The atoms can be put into a superradiant state by focusing a laser beam on atom B that is slightly off-resonance from the transition between states $\left|E_1\right\rangle$ and $\left|G_1\right\rangle$. The strength of the interaction can be adjusted to produce a minus sign on state $\left|E_1\right\rangle$ for atom B only. A similar procedure can be used to produce a minus sign for state $\left|E_2\right\rangle$ of atom B. This converts Eq. (7.22) into

$$\left|\psi'\right\rangle = \frac{1}{2}\left[\left(\left|E_1G_1\right\rangle + \left|G_1E_1\right\rangle\right) + e^{i\omega_{clock}t_f}\left(\left|E_2G_2\right\rangle + \left|G_2E_2\right\rangle\right)\right]. \tag{7.23}$$

Now the atoms are in a superposition of superradiant states where the rate of photon emission is enhanced by quantum interference effects instead of being suppressed.

The next step in the readout process is to mix the amplitudes of the two lower ground levels $\left|G_1\right\rangle$ and $\left|G_2\right\rangle$, which will allow quantum interference in the photon emission process. This can be done using a strong laser beam that is slightly off-resonance from the transition between states $\left|G_1\right\rangle$ and $\left|G_2\right\rangle$. (If there is no allowed matrix element between these two states, two laser beams and an intermediate state could be used instead.) The strength of the coupling is chosen to give a unitary transition of the form

$$|G_1\rangle \to \left(|G_1\rangle + |G_2\rangle\right)/\sqrt{2}, \quad |G_2\rangle \to \left(|G_2\rangle - |G_1\rangle\right)/\sqrt{2}. \tag{7.24}$$

Inserting this into Eq. (7.23) gives

$$\begin{aligned} |\psi\rangle = &\left\{\left[|E_1\rangle\left(|G_1\rangle + |G_2\rangle\right) + \left(|G_1\rangle + |G_2\rangle\right)|E_1\rangle\right]\right. \\ &\left. - e^{i\omega_{clock}t_f}\left[|E_2\rangle\left(|G_1\rangle - |G_2\rangle\right) + \left(|G_1\rangle - |G_2\rangle\right)|E_2\rangle\right]\right\}/2\sqrt{2}. \end{aligned} \tag{7.25}$$

We now post-select on the case where the atoms are not in the state $|G_2\rangle$, which could be accomplished by observing the photons emitted in a laser-induced transition to a higher-energy level, as is done in ion-trap quantum computing, for example [182-184]. This reduces Eq. (7.25) to

$$|\psi'\rangle = \left[\left(|E_1\rangle|G_1\rangle + |G_1\rangle|E_1\rangle\right) - e^{i\omega_{clock}t_f}\left(|E_2\rangle|G_1\rangle + |G_1\rangle|E_2\rangle\right)\right]/2. \tag{7.26}$$

The final step in the readout process is to apply a strong laser beam that is slightly off-resonance from the transition between $|E_2\rangle$ and $|G_1\rangle$, as illustrated in Fig. 7.8. Although the interaction between these two states and the cavity modes was assumed to be negligible, a sufficiently intense laser beam can produce the desired coupling. This allows a virtual transition in which the atoms can emit a photon with a frequency of $\omega_{clock} - \Delta'$ while making a transition from $|E_2\rangle$ to $|E_1\rangle$ [185-187], as shown in Fig. 7.8. Here Δ' is the detuning of the coupling laser from the ground state.

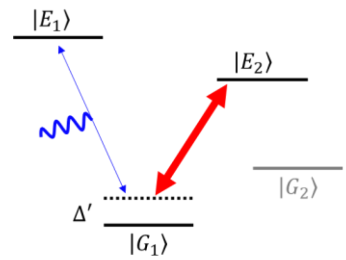

Figure 7.8 Measurement of the relative phase of two atomic states. The excited atomic states $\left|E_1\right\rangle$ and $\left|E_2\right\rangle$ in Eq. (7.26) can be coupled using a strong laser (red arrow) that is detuned from the transition between and $\left|G_1\right\rangle$. Photons (blue wavy line) can then be emitted in a virtual transition from state $\left|E_1\right\rangle$ to $\left|E_2\right\rangle$. The phase of the emitted field is shown in Fig. 7.9.

The expectation value of the electric field emitted by the atoms in this way is shown in Fig.7.9 as a function of time, as calculated using first-order perturbation theory. The initial phase of the field is equal to $\omega_{clock} t_f$, which could be directly measured using a homodyne detector, for example. A fit to this data could be used to determine the elapsed time t_f as indicated by the clock.

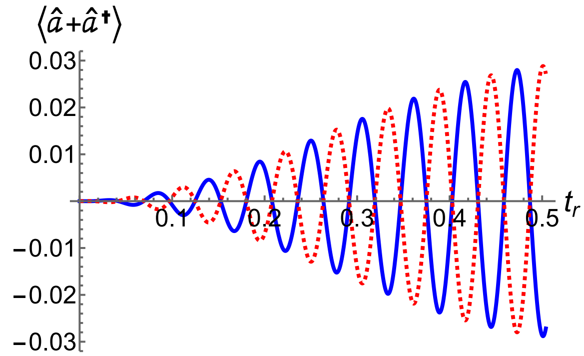

Figure 7.9 Mean electric field emitted during the readout of an atomic clock. The expectation value $\langle \hat{a} + \hat{a}^{\dagger} \rangle$ of the electric field emitted by the atoms in the state of Eq. (7.26) is plotted as a function of the time t_r. Here $t_r = 0$ corresponds to the time at which the coupling laser shown in Fig. 7.8 is turned on. The dashed (red) curve corresponds to a relative phase of $\omega_{clock} t_f = 0,$ while the solid (blue) curve corresponds to $\omega_{clock} t_f = \pi.$ These results correspond to an arbitrary choice of parameters with an interaction strength of $\Omega = 2,$ angular frequencies of $\omega_{G_1} = \omega_{G_2} = 0,$ $\omega_{E_1} = 1.2 \times 10^2,$ $\omega_{E_2} = 1.1 \times 10^2,$ a detuning of $\Delta' = 10,$ and a coupling laser amplitude of $A = 1.$ Dimensionless units have been used for convenience.

The accuracy of an atomic clock implemented in this way depends on the uncertainty in ω_{clock} due to interactions with the environment or other perturbations. The advantage of using the quantum Zeno effect is that locking the phases of the atomic states causes them to evolve at their average frequencies determined by $\bar{E}_k$ and $\bar{G}_k,$ which reduces the uncertainty in the clock frequency by a factor of $1/\sqrt{2}$. Practical applications may require that larger numbers of atoms be phase locked in this way in order to achieve an enhancement of $1/\sqrt{N}$.

7.5 Summary and conclusions

In this chapter, we have considered the possibility of using the quantum Zeno effect to lock the relative phases of an ensemble of N atoms that could be used to implement an atomic clock. This would reduce the effective bandwidth of the ensemble by a factor of $1/\sqrt{N}$ and improve the accuracy of an atomic clock by a corresponding amount.

We began by considering a pair of two-level atoms and showed that the Zeno effect can lock their phases in the limit of frequent measurements. This approach was based on the fact that an initial subradiant state with a small relative phase difference will slowly evolve into a superradiant state with a different relative phase. Frequent observations to determine whether or not the superradiant state has emitted any photons will inhibit the growth of the superradiant state, leaving the atoms in the original subradiant state with a well-defined relative phase. This has the effect of averaging any environmentally-induced phase shifts over the ensemble of atoms.

It was found that using a pair of two-level atoms does not allow a readout of the elapsed time, since there is only an unobservable overall phase in that case. Three-level atoms allow a readout of the elapsed time, but they are susceptible to an error source in which a photon can be absorbed by an atom in the ground state. Both of these difficulties can be resolved by using a pair of four-level atoms, where the elapsed time can be estimated by measuring the relative phase of two different excited states, as illustrated in Figs. 7.7 and 7.8.

These results show a potential enhancement by a factor of $\sqrt{2}$ in the precision of an atomic clock. Practical applications may require $N >> 2$ in order to obtain a good signal-to-noise ratio, and we have not been able to generalize this approach to larger values of N. In addition, the generation of the required initial state would be difficult for $N >> 2$, Fock states are required as a resource, and the measurement process is relatively complicated even for $N = 2$. As a result, further research would be required to find a more practical approach. Nevertheless, these results provide an interesting example of the potential use of the quantum Zeno effect.

Chapter 8 : Summary and conclusions

This thesis began with the examination of the generation of nonclassical states like photon-added states (and a range of other states) using an optical parametric amplifier (OPA) and conditional measurements in a single photon catalysis setup [50,52]. This method produces macroscopic superpositions of the displaced vacuum and single-photon Fock states. It could be used in continuous variable quantum information protocols due to the nonclassicality of these states and the tunability of the state preparation with the parametric gain.

Then we studied phase entanglement created by a Fock state [69]. Although the Fock state has an uncertain phase, it produces an entangled Schrödinger cat state after passing through a beam splitter. By demonstrating Bell's inequality violations using phase entanglement, we demonstrated that this entanglement can also be used for quantum communications, such as quantum key distribution. However, the primary concerns were the inefficiency of the detectors and the sensitivity to noise in the paths.

Current bottlenecks of most quantum communication approaches are low-efficiency detectors and high channel noise. Nevertheless, noiseless attenuation before transmission can facilitate arbitrarily high fidelity at the receivers when the signal is recovered from noiseless amplification, for quantum communication [17]. By considering the zero-photon subtraction setup, experimentally demonstrated by Ref.[18,19], we investigated the properties of the linear optical implementation of noiseless attenuation [124]. Earlier, this method had been shown to attenuate photon statistics without considering phase properties or coherence [19]. To verify that coherence is preserved by this method, we proposed a quantum interference measurement and studied the effects of using inefficient detectors with the Wigner quasiprobability.

The interference measurements mentioned above, and optical quantum computing require highly nonlinear interactions, but current materials don't allow them at the single-photon level. Instead, we use linear optics and conditional measurements that work non-deterministically. Most of these use dual rail encoding, but in some cases such as entanglement verification with Bell's inequality violations, we have to use a single rail. Specifically, we developed a destructive controlled phase gate for single rail targets and weak coherent states with a dual rail control qubit [14]. This method dramatically increases the success probability when the ancilla photons are prepared with a low probability, such as in a typical down-conversion and heralding setup [188]. The increased success rate, however, comes at the expense of destroying the control qubit, just as in measurement-based quantum computing schemes [106,107,189].

In recent years, applications of the quantum Zeno effect [21] have increased for use in quantum computing [161] and repeater networks [162]. In any communication network, reliable timekeeping is essential. We investigated how multi-atom clocks may be improved using the quantum Zeno effect [144]. Locking the relative phases of atoms can decrease their effective absorption bandwidth. Atoms whose transition frequencies are independently perturbed by the environment drift over time in relation to one another. A subradiant atomic state may develop superradiant components due to such drift. Our solution is to measure the superradiant components sufficiently frequently to prevent their growth entirely. In this way, it forces all atoms to evolve in sync at their average frequency, which is highly counterintuitive. Synchronizing the atoms their reduces bandwidth, illustrating the potential application of the quantum Zeno effect.

All the techniques proposed here are expected to be of potential use in quantum communications and are of fundamental interest as well.

Appendix A

The mean and variance of the photon number were briefly discussed in Chapter 3. The purpose of this appendix is to discuss some of their properties in more detail. For convenience, we rewrite the output state from Eq. (3.21) in the form

$$|\psi\rangle = C_0 \left|\alpha/g\right\rangle + C_1 \left|\alpha/g,1\right\rangle, \tag{A1}$$

where

$$C_0 \equiv \frac{1}{\sqrt{N}}\left(\frac{1}{g^2} - \left|\frac{\alpha}{g}\right|^2 G^2\right) \tag{A2}$$

and

$$C_1 \equiv -\frac{1}{\sqrt{N}}\frac{\alpha}{g}G^2. \tag{A3}$$

Using these definitions, the average photon number can be shown to be

$$\langle\hat{n}\rangle = \left|C_0\right|^2\left|\frac{\alpha}{g}\right|^2 + \left|C_1\right|^2\left(\left|\frac{\alpha}{g}\right|^2 + 1\right) - \frac{2}{N}\left|\frac{\alpha}{g}\right|^2\left(\frac{1}{g^2} - \left|\frac{\alpha}{g}\right|^2 G^2\right), \tag{A4}$$

which can be simplified further by using $\hat{n} = \hat{a}^\dagger\hat{a}$ to give

$$\langle\hat{n}\rangle = \left|C_0\right|^2\left\langle\frac{\alpha}{g}\middle|\hat{n}\middle|\frac{\alpha}{g}\right\rangle + \left|C_1\right|^2\left\langle\frac{\alpha}{g},1\middle|\hat{n}\middle|\frac{\alpha}{g},1\right\rangle + 2\,\mathrm{Re}\left(C_0^* C_1\left\langle\frac{\alpha}{g}\middle|\hat{n}\middle|\frac{\alpha}{g},1\right\rangle\right). \tag{A5}$$

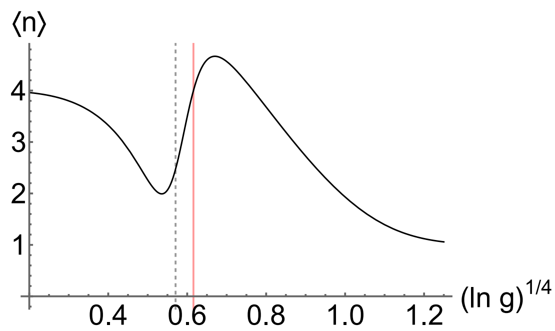

Figure A.1 Average photon number in the output signal mode as a function of the amplifier gain g, for an incident coherent state amplitude of $\alpha = 2$. The solid red vertical line corresponds to a gain of $g = g_0$ while the black dashed vertical line corresponds to a gain of $g = g_1$.

Figure A.1 shows the behavior of the average photon number as a function of the amplifier gain. We observe that the average photon number initially decreases as we increase the gain before increasing to a maximum value at a gain of approximately g_0. This behavior can also be seen in Fig. 3.5 where the peak value shifts closer to the origin between Fig. 3.3(a) and (b) whereas the peak shifts away from the origin between Figs. 3.3(b) and (d).

The second moment of the photon number in the final state can also be calculated using a similar procedure to give

$$\begin{aligned}\langle \hat{n}^2 \rangle &= |C_0|^2 \left(\left|\frac{\alpha}{g}\right|^2 + \left|\frac{\alpha}{g}\right|^4 \right) + |C_1|^2 \left(3\left|\frac{\alpha}{g}\right|^2 + \left(\left|\frac{\alpha}{g}\right|^2 + 1 \right)^2 \right) \\ &- \frac{2}{N}\left|\frac{\alpha}{g}\right|^2 \left(\frac{1}{g^2} - \left|\frac{\alpha}{g}\right|^2 G^2 \right)\left(2\left|\frac{\alpha}{g}\right|^2 + 1 \right),\end{aligned} \tag{A6}$$

from which the variance in the photon number can be calculated using

$$\mathrm{Var}(n) = \langle \hat{n}^2 \rangle - \langle \hat{n} \rangle^2. \tag{A7}$$

A plot of the variance is shown in Fig. A2 for an input coherent state amplitude of $\alpha = 2$. It can be seen that the variance increases rapidly to a maximum value at a gain of approximately g_0. This feature could be useful in experiments for determining if the output state is close to the displaced single photon state. Another interesting feature that can be seen in these plots is that the average photon number approaches unity in the limit of high gain while the variance vanishes, suggesting that a single photon state is produced in that limit.

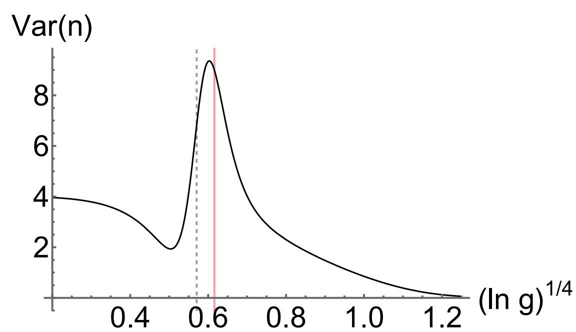

Figure A.2 Variance in the photon number of the output signal mode as a function of amplifier gain for the case in which the input coherent state has an amplitude of $\alpha = 2$. As in Fig. A.1, the solid red vertical line corresponds to a gain of $g = g_0$ while the black dashed vertical line corresponds to a gain of $g = g_1$.

Appendix B

The results in the Chapter 4 were derived using Eq. (4.4), which expresses a photon number state as a superposition of coherent states with all possible phases. In this appendix, we give an alternative derivation based on the properties of the Hermite polynomials. Although the results are equivalent to those in the text, they can be used to derive an analytic form for ψ_{++} or ψ_{--}.

This initial state of the system with N photons incident on the first beam splitter can be written in terms of the photon creation operators as

$$\left|\psi\right\rangle = \frac{\left(\hat{a}_1^{\dagger}\right)^N}{\sqrt{N!}}\left|0,0\right\rangle. \tag{B1}$$

Here the notation is the same as in the text. After passing through the beam splitter, Eq. (B1) can be used to write the transformed state as

$$\left|\psi\right\rangle = \frac{\left(\hat{a}_1^{\dagger} + i\hat{a}_2^{\dagger}\right)^N}{\sqrt{N!2^N}}\left|0,0\right\rangle. \tag{B2}$$

This can be rewritten using the binomial expansion as

$$\left|\psi\right\rangle = \sum_{n=0}^{N} i^n \sqrt{\frac{{}^N C_n}{2^N}}\left|N-n,n\right\rangle \tag{B3}$$

where ${}^N C_n$ are the binomial coefficients.

We can then simplify each of the terms in Eq. (4.14) by integrating over the phase ϕ. The results are that

$$\left|\psi_k\right\rangle = -p_k \frac{1}{4}\sum_{n=0}^{N} q_k^n \sqrt{\frac{{}^N C_n}{2^N}}\left|N-n,n\right\rangle, \tag{B4}$$

where $p_1 = e^{i(\sigma_1+\sigma_2+N\theta)}$, $p_2 = e^{i(\sigma_1-N\theta)}$, $p_3 = e^{i(\sigma_2+N\theta)}$, $p_4 = e^{-N\theta}$, $q_1 = q_4 = 1$ and $q_2 = q_3^* = e^{i2\theta}$. The index k corresponds to each of the four terms in Eq. (4.17).

The dimensionless position-basis representation of the final state is given by the inner product $\langle x_1, x_2 | \psi \rangle = \psi(x_1, x_2)$. We can use the position-basis representation of the number states,

$$\langle x | n \rangle = \sqrt{\frac{e^{-x^2}}{n! 2^n \sqrt{\pi}}} H_n(x), \tag{B5}$$

to obtain

$$\psi_k(x_1, x_2) = -p_k \frac{e^{-\left(x_1^2 + x_2^2\right)/2}}{4\sqrt{\pi N!}} \sum_{n=0}^{N} q_k^n \frac{{}^N C_n}{2^N} H_{(N-n)}(x_1) H_n(x_2). \tag{B6}$$

Here $H_n(x)$ is the n^{th} Hermite polynomial.

We can further simplify Eq. (B6) for $k = 1$ and $k = 4$ to the analytical form

$$\psi_k(x_1, x_2) = -p_k \frac{e^{-\left(x_1^2 + x_2^2\right)/2}}{4\sqrt{2^N \pi N!}} H_N\left(\frac{x_1 + x_2}{\sqrt{2}}\right). \tag{B7}$$

When the cross-terms terms corresponding to $k = 2$ and $k = 3$ are negligible, Eq. (B7) gives an interference pattern that is equivalent to Eq. (4.20) in the text, but without any complicated integrals over ϕ.

Appendix C

Some of the details of the calculations outlined in the Chapter 6 are presented in this Appendix.

We first consider the form of an even Schrödinger cat state. Combining Eqs. (6.2) and (6.3) gives

$$\left|\psi_{cat}\right\rangle = \frac{e^{-|\alpha|^2/2}}{\sqrt{2\left(1+e^{-2|\alpha|^2}\right)}}\sum_{n=0}^{\infty}\frac{\alpha^n+\left(-\alpha\right)^n}{\sqrt{n!}}\left|n\right\rangle. \qquad \text{(C1)}$$

Since the even terms are the only ones that contribute, we can introduce a new variable $k = n/2$, which gives

$$\left|\psi_{cat}\right\rangle = \frac{1}{\sqrt{\cosh|\alpha|^2}}\sum_{k=0}^{\infty}\frac{\alpha^{2k}}{\sqrt{(2k)!}}\left|2k\right\rangle. \qquad \text{(C2)}$$

This expression gives the values of the coefficients c_n that appear in Eq. (6.3) Rewriting the number states in terms of photon creation operators acting on vacuum gives

$$\left|\psi_{cat}\right\rangle = \frac{1}{\sqrt{\cosh|\alpha|^2}}\sum_{k=0}^{\infty}\frac{\alpha^{2k}}{(2k)!}\left(\hat{a}^{\dagger}\right)^{2k}\left|0\right\rangle. \qquad \text{(C3)}$$

The cat state of Eq. (C2) passes through a beam splitter as illustrated in Fig. 6.1. We use the beam splitter transformation of Eq. (6.5) to relate the photon creation operators in the input mode A to those in the output modes A and B, which gives

$$\hat{a}_{in}^{\dagger} \rightarrow t\hat{a}_{out}^{\dagger} + ir\hat{b}_{out}^{\dagger}. \qquad \text{(C4)}$$

We have chosen to represent the photon creation operators in modes A and B by $\hat{a}^\dagger$ and $\hat{b}^\dagger$, respectively. Inserting Eq. (C4) into Eq. (C3) gives the output state after the beam splitter:

$$\left|\psi_{cat}\right\rangle = \frac{1}{\sqrt{\cosh|\alpha|^2}} \sum_{k=0}^{\infty} \frac{\alpha^{2k}}{(2k)!} \left(t\hat{a}^\dagger + ir\hat{b}^\dagger\right)^{2k} |0\rangle|0\rangle. \tag{C5}$$

Using the binomial expansion and then applying the photon creation operators to the vacuum state, this can be rewritten as

$$\left|\psi_{cat}\right\rangle = \frac{1}{\sqrt{\cosh|\alpha|^2}} \sum_{k=0}^{\infty} \sum_{l=0}^{2k} \frac{\alpha^{2k}}{\sqrt{(2k-l)!\,l!}} (t)^{2k-l} (ir)^{l} |2k-l\rangle|l\rangle. \tag{C6}$$

Introducing two new variables defined by $n_b = l$ and $n_a = 2k - l$ gives

$$\left|\psi_{cat}\right\rangle = \frac{1}{\sqrt{\cosh|\alpha|^2}} \sum_{n_a=0}^{\infty} \sum_{n_b=0}^{\infty} f(n_a, n_b) \frac{(t\alpha)^{n_a} (ir\alpha)^{n_b}}{\sqrt{n_a!\,n_b!}} |n_a\rangle|n_b\rangle, \tag{C7}$$

where $f(n_a, n_b) = (n_a + n_b + 1) \bmod 2$. This gives the final state of Eq. (6.6) where the coefficients given are

$$c(n_a, n_b) = \left[(n_a + n_b + 1) \bmod 2\right] \frac{(t\alpha)^{n_a} (ir\alpha)^{n_b}}{\sqrt{n_a!\,n_b!\cosh|\alpha|^2}}. \tag{C8}$$

By setting $n_b = 0$ in Eq. (C8) and comparing with the coefficients in Eq.(C2) we see that heralding on zero photons in mode b would simply give another cat state with coherent states of amplitude $\alpha_{out} = t\alpha$ in mode a. This can also be noted by the transformation of the input state coefficients, c_n, to the output ones, $c_n t^n$.

Therefore, the Wigner function of the output, assuming real α, is

$$W_{out}^{(heralded)} = \left[e^{-\left(x+\sqrt{2}t\alpha\right)^2 - p^2} + e^{-\left(x-\sqrt{2}t\alpha\right)^2 - p^2} + 2e^{-\left(x^2+p^2\right)} \cos\left(2\sqrt{2}t\alpha p\right) \right] \Big/ 2\pi\left(1 + e^{-|t\alpha|^2}\right).$$

(C9)

Using the same procedure for an input state consisting of the single mode squeezed vacuum of Eq. (6.11) instead of an even Schrödinger cat state gives a set of coefficients of the form

$$c(n_a,n_b)=\left[\left(n_a+n_b+1\right)\bmod 2\right]\frac{(n_a+n_b)!\left(t\sqrt{\frac{-\tanh\xi}{2}}\right)^{n_a}\left(ir\sqrt{\frac{-\tanh\xi}{2}}\right)^{n_b}}{\left(\frac{n_a+n_b}{2}\right)!\sqrt{n_a!n_b!\cosh\xi}}$$
$$=\left[\left(n_a+n_b+1\right)\bmod 2\right]\left[\prod_{k=1}^{(n_a+n_b)/2}(2k-1)\right]\frac{\left(t\sqrt{-\tanh\xi}\right)^{n_a}\left(ir\sqrt{-\tanh\xi}\right)^{n_b}}{\sqrt{n_a!n_b!\cosh\xi}}.$$

(C10)

By setting $n_b=0$ in Eq. (C10) and comparing with the coefficients in Eq. (6.13) we see that heralding on zero photons in mode b would simply give another squeezed vacuum state with the squeezing parameters of the output given by $\tanh\xi_{out}=t^2\tanh\xi,$ or alternatively $s_{out}=\left[s\left(1+t^2\right)+\left(1-t^2\right)\right]/\left[s\left(1-t^2\right)+\left(1+t^2\right)\right]$. This can also be noted by the transformation of the input state coefficients, c_n, to the output ones, c_nt^n. For a given initial s, $s_{out}(t)$ is a monotonically decreasing function of the transmittivity t.

Therefore, the Wigner function of the attenuated output squeezed vacuum state is

$$W_{out}^{(heralded)}=\frac{1}{\pi}\exp\left[-\frac{s\left(1+t^2\right)+\left(1-t^2\right)}{s\left(1-t^2\right)+\left(1+t^2\right)}x^2-\frac{s\left(1-t^2\right)+\left(1+t^2\right)}{s\left(1+t^2\right)+\left(1-t^2\right)}p^2\right].$$

(C11)

Equations (C9) and (C11) give analytic results for the case of a Schrödinger cat or a single mode squeezed state incident on a beam splitter. Although a similar calculation could be done for the case of a two-mode squeezed vacuum incident on a Mach-Zehnder interferometer as in Fig. 6.9, the analysis is more tedious and numerical solutions were used instead.

If heralding on zero is done using a detector of efficiency η, instead of setting $n_b = 0$ we need to use the density operator formalism and use the projector,

$$\hat{\Pi}_0 = \sum_{n_b=0}^{\infty} (1-\eta)^{n_b} \left| n_b \right\rangle \left\langle n_b \right|. \tag{C12}$$

This gives the un-normalized output state

$$\tilde{\rho}_{out}^{(heralded)} = \mathrm{Tr}\left[\hat{\rho}_{in} \hat{\Pi}_0 \right] = \sum_{n_b=0}^{\infty} (1-\eta^{n_b}) \left| \psi_{out|n_b} \right\rangle \left\langle \psi_{out|n_b} \right|, \tag{C13}$$

If the input is an even cat state, then for even $n_b (\equiv 2k)$,

$$\begin{aligned} \left| \psi_{out|2k} \right\rangle &= \frac{(ir\alpha)^{2k}}{\sqrt{(2k)!}} \sqrt{\frac{\cosh\left(|t\alpha|^2\right)}{\cosh\left(|\alpha|^2\right)}} \left(\frac{1}{\sqrt{\cosh|t\alpha|^2}} \sum_{m=0}^{\infty} \frac{(t\alpha)^{2m}}{\sqrt{(2m)!}} |2m\rangle \right) \\ &= \frac{(ir\alpha)^{2k}}{\sqrt{(2k)!}} \sqrt{\frac{\cosh\left(|t\alpha|^2\right)}{\cosh\left(|\alpha|^2\right)}} |\mathrm{Even\ Cat}(t\alpha)\rangle, \end{aligned} \tag{C14}$$

and similarly for odd $n_b (\equiv 2k+1)$,

$$\left| \psi_{out|2k+1} \right\rangle = \frac{(ir\alpha)^{2k+1}}{\sqrt{(2k+1)!}} \sqrt{\frac{\sinh\left(|t\alpha|^2\right)}{\cosh\left(|\alpha|^2\right)}} |\mathrm{Odd\ Cat}(t\alpha)\rangle. \tag{C15}$$

Using Eqs. (C14) and (C15) in (C13) give the un-normalized state,

$$\begin{aligned} \tilde{\rho}_{out}^{(heralded)} &= \left[\sum_{k=0}^{\infty} \frac{(1-\eta)^{2k} \left(|ir\alpha|^2 \right)^{2k}}{(2k)!} \right] \left[\frac{\cosh\left(|t\alpha|^2\right)}{\cosh\left(|\alpha|^2\right)} \right] \hat{\rho}_+ \\ &+ \left[\sum_{k=0}^{\infty} \frac{(1-\eta)^{2k+1} \left(|ir\alpha|^2 \right)^{2k+1}}{(2k+1)!} \right] \left[\frac{\sinh\left(|t\alpha|^2\right)}{\cosh\left(|\alpha|^2\right)} \right] \hat{\rho}_-, \end{aligned} \tag{C16}$$

where $\hat{\rho}_+$ and $\hat{\rho}_-$ are the normalized density operators for even and odd cat states with amplitude $t\alpha$ respectively. This simplifies to the normalized output

$$\hat{\rho}_{out}^{(heralded)} = \frac{p_+\hat{\rho}_+ + p_-\hat{\rho}_-}{p_+ + p_-}, \tag{C17}$$

where

$$p_+ = \frac{\cosh\left(|t\alpha|^2\right)\cosh\left[(1-\eta)|ir\alpha|^2\right]}{\cosh\left(|\alpha|^2\right)}, \tag{C18}$$

and

$$p_- = \frac{\sinh\left(|t\alpha|^2\right)\sinh\left[(1-\eta)|ir\alpha|^2\right]}{\cosh\left(|\alpha|^2\right)}. \tag{C19}$$

The corresponding Wigner function is

$$W_{out}^{(heralded)} = \frac{p_+W_+ + p_-W_-}{p_+ + p_-}, \tag{C20}$$

where

$$W_\pm = \frac{e^{-\left(x+\sqrt{2}t\alpha\right)^2-p^2} + e^{-\left(x-\sqrt{2}t\alpha\right)^2-p^2} \pm 2e^{-\left(x^2+p^2\right)}\cos\left(2\sqrt{2}t\alpha p\right)}{2\pi\left(1 \pm e^{-|t\alpha|^2}\right)}. \tag{C21}$$

The success probability of the heralding is $p_+ + p_-$. It may be interesting to note that in this case, the noise remaining in the system is simply an odd cat state. In general, for other input states, the output heralded with an inefficient detector will have a more complicated noise term.

Bibliography

[1] M. A. Nielsen and I. L. Chuang, *Quantum Computation and Quantum Information: 10th Anniversary Edition* (Cambridge University Press, Cambridge, 2010).

[2] J.-G. Ren *et al.*, Nature **549**, 70 (2017).

[3] E. Musk, New Space **5**, 46 (2017).

[4] J. L. O'Brien, Science **318**, 1567 (2007).

[5] J. Liu, C. T. Hann, and L. Jiang, preprint, arXiv:2207.14336 (2022).

[6] A. Einstein, B. Podolsky, and N. Rosen, Physical Review **47**, 777 (1935).

[7] C. T. Lee, Physical Review A **44**, R2775 (1991).

[8] M. S. Kim, W. Son, V. Bužek, and P. L. Knight, Physical Review A **65**, 032323 (2002).

[9] J. S. Bell, Physics Physique Fizika **1**, 195 (1964).

[10] J. F. Clauser and A. Shimony, Reports on Progress in Physics **41**, 1881 (1978).

[11] H. Jeong, M. S. Kim, T. C. Ralph, and B. S. Ham, Physical Review A **70**, 061801 (2004).

[12] W. J. Munro, K. Nemoto, and T. P. Spiller, New Journal of Physics **7**, 137 (2005).

[13] E. Knill, R. Laflamme, and G. J. Milburn, Nature **409**, 46 (2001).

[14] S. U. Shringarpure and J. D. Franson, Scientific Reports **11**, 1 (2021).

[15] C. M. Caves, J. Combes, J. Zhang, and S. Pandey, Physical Review A (Atomic, Molecular, and Optical Physics) **86**, 063802 (2012).

[16] C. M. Caves, Physical Review D **26**, 1817 (1982).

[17] M. Mičuda, I. Straka, M. Miková, M. Dušek, N. J. Cerf, J. Fiurášek, and M. Ježek, Physical Review Letters **109**, 180503 (2012).

[18] C. M. Nunn, J. D. Franson, and T. B. Pittman, Physical Review A **104**, 033717 (2021).

[19] C. M. Nunn, J. D. Franson, and T. B. Pittman, Physical Review A **105**, 033702 (2022).

[20] L. Essen and J. V. L. Parry, Philosophical Transactions of the Royal Society of London. Series A, Mathematical and Physical Sciences **250**, 45 (1957).

[21] B. Misra and E. C. G. Sudarshan, Journal of Mathematical Physics **18**, 756 (1977).

[22] A. Beige, D. Braun, B. Tregenna, and P. L. Knight, Physical Review Letters **85**, 1762 (2000).

[23] G. Baym, *Lectures on Quantum Mechanics* (CRC Press, 2018).

[24] D. Manzano, AIP Advances **10**, 025106 (2020).

[25] E. Schrödinger, Naturwissenschaften **23**, 844 (1935).

[26] C. Gerry, P. Knight, and P. L. Knight, *Introductory Quantum Optics* (Cambridge university press, 2005).

[27] W. P. Schleich, *Quantum Optics in Phase Space* (John Wiley & Sons, 2011).

[28] F. Siyouri, M. El Baz, and Y. Hassouni, Quantum Information Processing **15**, 4237 (2016).

[29] I. I. Arkhipov, A. Barasiński, and J. Svozilík, Scientific Reports **8**, 1 (2018).

[30] M. Hillery, Physics Letters A **111**, 409 (1985).

[31] A. N. Kolmogorov and A. T. Bharucha-Reid, *Foundations of the Theory of Probability: Second English Edition* (Courier Dover Publications, 2018).

[32] N. G. Walker, Journal of Modern Optics **34**, 15 (1987).

[33] Y. Lai and H. A. Haus, Quantum Optics: Journal of the European Optical Society Part B **1**, 99 (1989).

[34] U. Leonhardt and H. Paul, Physical Review A **47**, R2460 (1993).

[35] W. M. Itano, D. J. Heinzen, J. J. Bollinger, and D. J. Wineland, Physical Review A **41**, 2295 (1990).

[36] B. Kaulakys and V. Gontis, Physical Review A **56**, 1131 (1997).

[37] P. Facchi and S. Pascazio, Journal of Physics A: Mathematical and Theoretical **41**, 493001 (2008).

[38] J. D. Jackson, *Classical Electrodynamics* (American Association of Physics Teachers, 1999).

[39] C. Weedbrook, S. Pirandola, R. García-Patrón, N. J. Cerf, T. C. Ralph, J. H. Shapiro, and S. Lloyd, Reviews of Modern Physics **84**, 621 (2012).

[40] G. Cariolaro and G. Pierobon, preprint, arXiv:1704.02008 (2017).

[41] A. Vourdas, Physical Review A **46**, 442 (1992).

[42] M. G. A. Paris, Physics Letters A **217**, 78 (1996).

[43] X. Ma and W. Rhodes, Physical Review A **41**, 4625 (1990).

[44] S. L. Braunstein, Physical Review A **71**, 055801 (2005).

[45] G. Cariolaro and G. Pierobon, Physical Review A **93**, 062115 (2016).

[46] A. DasGupta, American Journal of Physics **64**, 1422 (1996).

[47] A. Mufti, H. A. Schmitt, and M. Sargent Iii, American Journal of Physics **61**, 729 (1993).

[48] F. A. Raffa, M. Rasetti, and V. Penna, Physics Letters A **438**, 128106 (2022).

[49] M. Ban, Journal of the Optical Society of America B **10**, 1347 (1993).

[50] S. U. Shringarpure and J. D. Franson, Physical Review A **100**, 043802 (2019).

[51] A. I. Lvovsky and J. Mlynek, Physical Review Letters **88**, 250401 (2002).

[52] X.-x. Xu and H.-c. Yuan, Physics Letters A **380**, 2342 (2016).

[53] J. Sperling, W. Vogel, and G. S. Agarwal, Physical Review A **89**, 043829 (2014).

[54] M. Dakna, L. Knoll, and D. G. Welsch, Optics Communications **145**, 309 (1998).

[55] E. Bimbard, N. Jain, A. MacRae, and A. I. Lvovsky, Nature Photonics **4**, 243 (2010).

[56] D. T. Pegg, L. S. Phillips, and S. M. Barnett, Physical Review Letters **81**, 1604 (1998).

[57] M. Ban, Optics Communications **143**, 225 (1997).

[58] S. M. Barnett, D. T. Pegg, and J. Jeffers, Optics Communications **172**, 55 (1999).

[59] R. A. Brewster, I. C. Nodurft, T. B. Pittman, and J. D. Franson, Physical Review A **96**, 042307 (2017).

[60] S. Sivakumar, Physical Review A (Atomic, Molecular, and Optical Physics) **83**, 035802 (2011).

[61] A. Luis and J. Peřina, Physical Review A **53**, 1886 (1996).

[62] C. Brif and A. Mann, Quantum and Semiclassical Optics: Journal of the European Optical Society Part B **9**, 899 (1997).

[63] B. L. Schumaker and C. M. Caves, Physical Review A (General Physics) **31**, 3093 (1985).

[64] F. A. M. de Oliveira, M. S. Kim, P. L. Knight, and V. Buzek, Physical Review A (Atomic, Molecular, and Optical Physics) **41**, 2645 (1990).

[65] K. Husimi, Proceedings of the Physico-Mathematical Society of Japan. 3rd Series **22**, 264 (1940).

[66] Y. Kano, Journal of Mathematical Physics **6**, 1913 (1965).

[67] M. D. Eisaman, J. Fan, A. Migdall, and S. V. Polyakov, Review of Scientific Instruments **82**, 071101 (2011).

[68] I. C. Nodurft, R. A. Brewster, T. B. Pittman, and J. D. Franson, Physical Review A **100**, 013850 (2019).

[69] S. U. Shringarpure and J. D. Franson, Physical Review A **102**, 023719 (2020).

[70] J. F. Clauser, M. A. Horne, A. Shimony, and R. A. Holt, Physical Review Letters **23**, 880 (1969).

[71] M. Genovese, Physics Reports **413**, 319 (2005).

[72] S. J. Freedman and J. F. Clauser, Physical Review Letters **28**, 938 (1972).

[73] J. F. Clauser, Physical Review Letters **36**, 1223 (1976).

[74] E. S. Fry and R. C. Thompson, Physical Review Letters **37**, 465 (1976).

[75] A. Aspect, J. Dalibard, and G. Roger, Physical Review Letters **49**, 1804 (1982).

[76] W. Perrie, A. J. Duncan, H. J. Beyer, and H. Kleinpoppen, Physical Review Letters **54**, 1790 (1985).

[77] Z. Y. Ou and L. Mandel, Physical Review Letters **61**, 50 (1988).

[78] Y. H. Shih and C. O. Alley, Physical Review Letters **61**, 2921 (1988).

[79] J. D. Franson, Physical review letters **62**, 2205 (1989).

[80] Z. Jiang, M. D. Lang, and C. M. Caves, Physical Review A **88**, 044301 (2013).

[81] A. Ourjoumtsev, H. Jeong, R. Tualle-Brouri, and P. Grangier, Nature **448**, 784 (2007).

[82] A. Gilchrist, P. Deuar, and M. D. Reid, Physical Review Letters **80**, 3169 (1998).

[83] O. Thearle *et al.*, Physical Review Letters **120**, 040406 (2018).

[84] C. F. Wildfeuer, A. P. Lund, and J. P. Dowling, Physical Review A **76**, 052101 (2007).

[85] D. Cavalcanti, N. Brunner, P. Skrzypczyk, A. Salles, and V. Scarani, Physical Review A **84**, 022105 (2011).

[86] B. T. Kirby and J. D. Franson, Physical Review A **87**, 053822 (2013).

[87] J. Janszky, P. Domokos, and P. Adam, Physical Review A **48**, 2213 (1993).

[88] J. D. Franson, Physical Review A **49**, 3221 (1994).

[89] C. Cohen-Tannoudji, B. Diu, and F. Laloe, *Quantum Mechanics, Vol. I & II* (John Wiley, 1978).

[90] W. Berej and P. Rozmej, European Journal of Physics **20**, L25 (1999).

[91] J. Brendel, E. Mohler, and W. Martienssen, Europhysics Letters **20**, 575 (1992).

[92] B. T. Kirby and J. D. Franson, Physical Review A **89**, 033861 (2014).

[93] T. C. Ralph and A. P. Lund, in *Proceedings of the 9th International Conference on Quantum Communication Measurement and Computing* (American Institute of Physics, 2009), pp. 155.

[94] L. S. Costanzo, A. S. Coelho, N. Biagi, J. Fiurášek, M. Bellini, and A. Zavatta, Physical Review Letters **119**, 013601 (2017).

[95] J. Fiurášek, Optics Express **30**, 1466 (2022).

[96] P. M. Pearle, Physical Review D **2**, 1418 (1970).

[97] C. Branciard, Physical Review A **83**, 032123 (2011).

[98] G. J. Milburn, Physical Review Letters **62**, 2124 (1989).

[99] B. Yurke and D. Stoler, Physical Review Letters **57**, 13 (1986).

[100] D. Vitali, M. Fortunato, and P. Tombesi, Physical Review Letters **85**, 445 (2000).

[101] M. G. A. Paris, M. B. Plenio, S. Bose, D. Jonathan, and G. M. D'Ariano, Physics Letters A **273**, 153 (2000).

[102] E. Knill, Physical Review A **66**, 052306 (2002).

[103] E. Knill, Physical Review A **68**, 064303 (2003).

[104] J. D. Franson, M. M. Donegan, M. J. Fitch, B. C. Jacobs, and T. B. Pittman, Physical Review Letters **89**, 137901 (2002).

[105] T. B. Pittman, B. C. Jacobs, and J. D. Franson, Physical Review Letters **88**, 257902 (2002).

[106] T. B. Pittman, B. C. Jacobs, and J. D. Franson, Physical Review A **69**, 042306 (2004).

[107] D. E. Browne and T. Rudolph, Physical Review Letters **95**, 010501 (2005).

[108] K. Kieling, J. L. O'Brien, and J. Eisert, New Journal of Physics **12**, 013003 (2010).

[109] K. Lemr, A. Černoch, J. Soubusta, K. Kieling, J. Eisert, and M. Dušek, Physical Review Letters **106**, 013602 (2011).

[110] A. Reiserer, N. Kalb, G. Rempe, and S. Ritter, Nature **508**, 237 (2014).

[111] T. G. Tiecke, J. D. Thompson, N. P. de Leon, L. R. Liu, V. Vuletić, and M. D. Lukin, Nature **508**, 241 (2014).

[112] D. Tiarks, S. Schmidt-Eberle, T. Stolz, G. Rempe, and S. Dürr, Nature Physics **15**, 124 (2019).

[113] W.-Q. Liu, H.-R. Wei, and L.-C. Kwek, Physical Review Applied **14**, 054057 (2020).

[114] X. Zou, K. Pahlke, and W. Mathis, Physical Review A **65**, 064305 (2002).

[115] S. Scheel, J. K. Pachos, E. A. Hinds, and P. L. Knight, in *Quantum Coherence* (Springer, 2006), pp. 47.

[116] T. C. Ralph, N. K. Langford, T. B. Bell, and A. G. White, Physical Review A **65**, 062324 (2002).

[117] C. N. Gagatsos, J. Fiurášek, A. Zavatta, M. Bellini, and N. J. Cerf, Physical Review A **89**, 062311 (2014).

[118] C.-K. Hong, Z.-Y. Ou, and L. Mandel, Physical Review Letters **59**, 2044 (1987).

[119] E. Meyer-Scott, C. Silberhorn, and A. Migdall, Review of Scientific Instruments **91**, 041101 (2020).

[120] A. V. Kuhlmann, J. Houel, A. Ludwig, L. Greuter, D. Reuter, A. D. Wieck, M. Poggio, and R. J. Warburton, Nature Physics **9**, 570 (2013).

[121] A. V. Kuhlmann, J. H. Prechtel, J. Houel, A. Ludwig, D. Reuter, A. D. Wieck, and R. J. Warburton, Nature Communications **6**, 1 (2015).

[122] G. Kiršanskė *et al.*, Physical Review B **96**, 165306 (2017).

[123] N. Somaschi *et al.*, Nature Photonics **10**, 340 (2016).

[124] S. U. Shringarpure, C. M. Nunn, T. B. Pittman, and J. D. Franson, Physical Review A **105**, 013704 (2022).

[125] G.-Y. Xiang, T. C. Ralph, A. P. Lund, N. Walk, and G. J. Pryde, Nature Photonics **4**, 316 (2010).

[126] J. Fiurášek and N. J. Cerf, Physical Review A **86**, 060302 (2012).

[127] N. Walk, A. P. Lund, and T. C. Ralph, New Journal of Physics **15**, 073014 (2013).

[128] H. M. Chrzanowski, N. Walk, S. M. Assad, J. Janousek, S. Hosseini, T. C. Ralph, T. Symul, and P. K. Lam, Nature Photonics **8**, 333 (2014).

[129] A. Allevi, A. Andreoni, M. Bondani, M. G. Genoni, and S. Olivares, Physical Review A **82**, 013816 (2010).

[130] Y. Zhai *et al.*, Optics Letters **38**, 2171 (2013).

[131] Y. I. Bogdanov, K. G. Katamadze, G. V. Avosopiants, L. V. Belinsky, N. A. Bogdanova, A. A. Kalinkin, and S. P. Kulik, Physical Review A **96**, 063803 (2017).

[132] J. Hloušek, M. Ježek, and R. Filip, Scientific Reports **7**, 1 (2017).

[133] O. S. Magana-Loaiza *et al.*, npj Quantum Information **5**, 1 (2019).

[134] K. G. Katamadze, G. V. Avosopiants, N. A. Bogdanova, Y. I. Bogdanov, and S. P. Kulik, Physical Review A **101**, 013811 (2020).

[135] A. I. Lvovsky and M. G. Raymer, Reviews of Modern Physics **81**, 299 (2009).

[136] D. T. Smithey, M. Beck, M. G. Raymer, and A. Faridani, Physical Review Letters **70**, 1244 (1993).

[137] V. V. Dodonov, I. A. Malkin, and V. I. Man'Ko, Physica **72**, 597 (1974).

[138] A. Kenfack and K. Życzkowski, Journal of Optics B: Quantum and Semiclassical Optics **6**, 396 (2004).

[139] S. Glancy and H. M. de Vasconcelos, Journal of the Optical Society of America B **25**, 712 (2008).

[140] A. Serafini, S. De Siena, F. Illuminati, and M. G. A. Paris, Journal of Optics B: Quantum and Semiclassical Optics **6**, S591 (2004).

[141] J. N. Hollenhorst, Physical Review D **19**, 1669 (1979).

[142] L.-A. Wu, M. Xiao, and H. J. Kimble, Journal of the Optical Society of America B **4**, 1465 (1987).

[143] B. Böhmer and U. Leonhardt, Optics Communications **118**, 181 (1995).

[144] S. U. Shringarpure and J. D. Franson, preprint, arXiv:2208.06301 (2022).

[145] F. G. Major, *The Quantum Beat: Principles and Applications of Atomic Clocks* (Springer, 2007), Vol. 2.

[146] M. S. Grewal, A. P. Andrews, and C. G. Bartone, *Global Navigation Satellite Systems, Inertial Navigation, and Integration* (John Wiley & Sons, 2020).

[147] S. Blatt *et al.*, Physical Review Letters **100**, 140801 (2008).

[148] T. Rosenband *et al.*, Science **319**, 1808 (2008).

[149] M. J. Martin, M. Bishof, M. D. Swallows, X. Zhang, C. Benko, J. Von-Stecher, A. V. Gorshkov, A. M. Rey, and J. Ye, Science **341**, 632 (2013).

[150] S. Bize *et al.*, Comptes Rendus Physique **5**, 829 (2004).

[151] A. D. Ludlow, M. M. Boyd, J. Ye, E. Peik, and P. O. Schmidt, Reviews of Modern Physics **87**, 637 (2015).

[152] L. Pezze, A. Smerzi, M. K. Oberthaler, R. Schmied, and P. Treutlein, Reviews of Modern Physics **90**, 035005 (2018).

[153] E. Pedrozo-Peñafiel *et al.*, Nature **588**, 414 (2020).

[154] D. W. Allan, Proceedings of the IEEE **54**, 221 (1966).

[155] A. Signoles, A. Facon, D. Grosso, I. Dotsenko, S. Haroche, J.-M. Raimond, M. Brune, and S. Gleyzes, Nature Physics **10**, 715 (2014).

[156] H. V. Do, M. Gessner, F. S. Cataliotti, and A. Smerzi, Physical Review Research **1**, 033028 (2019).

[157] A. Beige, Physical Review A **69**, 012303 (2004).

[158] W. Zheng, D. Z. Xu, X. Peng, X. Zhou, J. Du, and C. P. Sun, Physical Review A **87**, 032112 (2013).

[159] M. C. Fischer, B. Gutiérrez-Medina, and M. G. Raizen, Physical Review Letters **87**, 040402 (2001).

[160] J. Bernu, S. Deléglise, C. Sayrin, S. Kuhr, I. Dotsenko, M. Brune, J.-M. Raimond, and S. Haroche, Physical Review Letters **101**, 180402 (2008).

[161] J. D. Franson, B. C. Jacobs, and T. B. Pittman, Physical Review A **70**, 062302 (2004).

[162] V. Bayrakci and F. Ozaydin, preprint, arXiv:2206.08785 (2022).

[163] X.-B. Wang, J. Q. You, and F. Nori, Physical Review A **77**, 062339 (2008).

[164] J.-M. Raimond, P. Facchi, B. Peaudecerf, S. Pascazio, C. Sayrin, I. Dotsenko, S. Gleyzes, M. Brune, and S. Haroche, Physical Review A **86**, 032120 (2012).

[165] Y. Lin *et al.*, Physical Review Letters **117**, 140502 (2016).

[166] L. Magazzù, J. D. Jaramillo, P. Talkner, and P. Hänggi, Physica Scripta **93**, 064001 (2018).

[167] M. A. Fasihi, Physica Scripta **94**, 085104 (2019).

[168] M. A. Fasihi, M. Khanzadeh, P. Hasanzadeh, and S. E. Asl, The European Physical Journal D **75**, 1 (2021).

[169] V. Mukherjee, A. G. Kofman, and G. Kurizki, Communications Physics **3**, 1 (2020).

[170] R. Jozsa, D. S. Abrams, J. P. Dowling, and C. P. Williams, Physical Review Letters **85**, 2010 (2000).

[171] E. O. Ilo-Okeke, L. Tessler, J. P. Dowling, and T. Byrnes, npj Quantum Information **4**, 1 (2018).

[172] R. H. Dicke, Physical Review **93**, 99 (1954).

[173] W. Li, N. Es'haqi-Sani, W.-Z. Zhang, and D. Vitali, Physical Review A **103**, 043715 (2021).

[174] T. E. Lee and H. R. Sadeghpour, Physical Review Letters **111**, 234101 (2013).

[175] J. Rohn, K. P. Schmidt, and C. Genes, preprint, arXiv:2111.02201 (2021).

[176] A. A. Gangat and G. J. Milburn, preprint, arXiv:2109.05390 (2021).

[177] D. G. Enzer, D. W. Murphy, and E. A. Burt, IEEE Transactions on Ultrasonics, Ferroelectrics, and Frequency Control **68**, 2590 (2021).

[178] B. W. Shore and P. L. Knight, Journal of Modern Optics **40**, 1195 (1993).

[179] D. Pavolini, A. Crubellier, P. Pillet, L. Cabaret, and S. Liberman, Physical Review Letters **54**, 1917 (1985).

[180] P. Domokos, M. Brune, J. M. Raimond, and S. Haroche, The European Physical Journal D-Atomic, Molecular, Optical and Plasma Physics **1**, 1 (1998).

[181] P. Bertet, S. Osnaghi, P. Milman, A. Auffeves, P. Maioli, M. Brune, J.-M. Raimond, and S. Haroche, Physical Review Letters **88**, 143601 (2002).

[182] D. Kielpinski, C. Monroe, and D. J. Wineland, Nature **417**, 709 (2002).

[183] T. P. Harty, D. T. C. Allcock, C. J. Ballance, L. Guidoni, H. A. Janacek, N. M. Linke, D. N. Stacey, and D. M. Lucas, Physical Review Letters **113**, 220501 (2014).

[184] B. Lekitsch, S. Weidt, A. G. Fowler, K. Mølmer, S. J. Devitt, C. Wunderlich, and W. K. Hensinger, Science Advances **3**, e1601540 (2017).

[185] I. Ashraf, J. Gea-Banacloche, and M. S. Zubairy, Physical Review A **42**, 6704 (1990).

[186] A. H. Toor and M. S. Zubairy, Physical Review A **45**, 4951 (1992).

[187] A. F. Linskens, I. Holleman, N. Dam, and J. Reuss, Physical Review A **54**, 4854 (1996).

[188] T. B. Pittman, B. C. Jacobs, and J. D. Franson, Optics Communications **246**, 545 (2005).

[189] P. Kok, W. J. Munro, K. Nemoto, T. C. Ralph, J. P. Dowling, and G. J. Milburn, Reviews of Modern Physics **79**, 135 (2007).